(12) INTERNATIONAL APPLICATION PUBLISHED UNDER THE PATENT COOPERATION TREATY (PCT)

(19) World Intellectual Property Organization
International Bureau

(43) International Publication Date
23 March 2023 (23.03.2023)

WIPO | PCT

(10) International Publication Number
WO 2023/044066 A1

(51) International Patent Classification:
G01K 1/02 (2006.01) *G01K 7/36* (2006.01)

(21) International Application Number:
PCT/US2022/043892

(22) International Filing Date:
16 September 2022 (16.09.2022)

(25) Filing Language: English

(26) Publication Language: English

(30) Priority Data:
63/245,088 16 September 2021 (16.09.2021) US

(71) Applicant: **GOVERNMENT OF THE UNITED STATES OF AMERICA, AS REPRESENTED BY THE SECRETARY OF COMMERCE** [US/US]; National Institute of Standards and Technology, 100 Bureau Drive, Gaithersburg, Maryland 20899 (US).

(72) Inventors: **DENNIS, Cindi Leigh**; National Institute of Standards and Technology, 100 Bureau Drive, Gaithersburg, Maryland 20899 (US). **RUS, Eric Daniel**; National Institute of Standards and Technology, 100 Bureau Drive, Gaithersburg, Maryland 20899 (US).

(74) Agent: **HAIN, Toby D.**; National Institute of Standards and Technology, 100 Bureau Drive, Gaithersburg, Maryland 20899 (US).

(81) Designated States *(unless otherwise indicated, for every kind of national protection available)*: AE, AG, AL, AM, AO, AT, AU, AZ, BA, BB, BG, BH, BN, BR, BW, BY, BZ, CA, CH, CL, CN, CO, CR, CU, CV, CZ, DE, DJ, DK, DM, DO, DZ, EC, EE, EG, ES, FI, GB, GD, GE, GH, GM, GT, HN, HR, HU, ID, IL, IN, IQ, IR, IS, IT, JM, JO, JP, KE, KG, KH, KN, KP, KR, KW, KZ, LA, LC, LK, LR, LS, LU, LY, MA, MD, ME, MG, MK, MN, MW, MX, MY, MZ, NA, NG, NI, NO, NZ, OM, PA, PE, PG, PH, PL, PT, QA, RO, RS, RU, RW, SA, SC, SD, SE, SG, SK, SL, ST, SV, SY, TH, TJ, TM, TN, TR, TT, TZ, UA, UG, US, UZ, VC, VN, WS, ZA, ZM, ZW.

(84) Designated States *(unless otherwise indicated, for every kind of regional protection available)*: ARIPO (BW, GH, GM, KE, LR, LS, MW, MZ, NA, RW, SD, SL, ST, SZ, TZ, UG, ZM, ZW), Eurasian (AM, AZ, BY, KG, KZ, RU, TJ, TM), European (AL, AT, BE, BG, CH, CY, CZ, DE, DK, EE, ES, FI, FR, GB, GR, HR, HU, IE, IS, IT, LT, LU, LV, MC, MK, MT, NL, NO, PL, PT, RO, RS, SE, SI, SK, SM, TR), OAPI (BF, BJ, CF, CG, CI, CM, GA, GN, GQ, GW, KM, ML, MR, NE, SN, TD, TG).

Published:
— *with international search report (Art. 21(3))*
— *before the expiration of the time limit for amending the claims and to be republished in the event of receipt of amendments (Rule 48.2(h))*

(54) Title: MAGNETICALLY-RESPONSIVE THERMAL SENSOR FOR DETERMINING THE TEMPERATURE OF A LOCAL MICROSCALE VOLUME AND CORRESPONDING PROCESS FOR DETERMINING THE TEMPERATURE OF A LOCAL MICROSCALE VOLUME WITH A MAGNETICALLY-RESPONSIVE THERMAL SENSOR

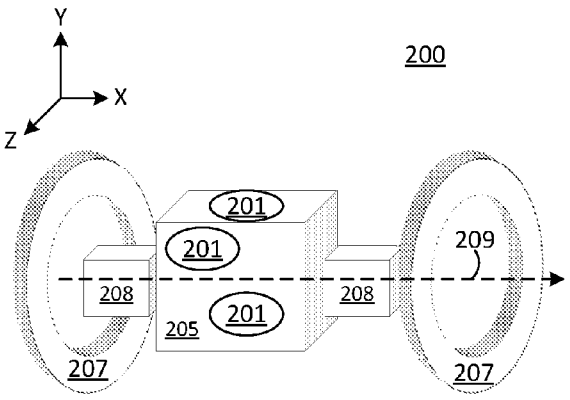

FIG. 5

(57) Abstract: A magnetically-responsive thermal sensor determines the temperature of a local microscale volume and includes: a magnetic nano-thermometer that comprises a main magnetic layer and a subordinate magnetic layer disposed on the main magnetic layer, such that: the main magnetic layer comprises a first magnetic material that: couples, via magnetic coupling, with the subordinate magnetic layer; or has a large change in magnetization as a function of temperature that produces a magnetic phase transition of the main magnetic layer; and the subordinate magnetic layer comprises a second magnetic material that: couples, via magnetic coupling, with the main magnetic layer; or has a large change in magnetization as a function of temperature that produces a magnetic phase transition of the subordinate magnetic layer, wherein the magnetic nano-thermometer produces a magnetic response from which the temperature of the local microscale environment is determined.

WO 2023/044066 A1

MAGNETICALLY-RESPONSIVE THERMAL SENSOR FOR DETERMINING THE TEMPERATURE OF A LOCAL MICROSCALE VOLUME AND CORRESPONDING PROCESS FOR DETERMINING THE TEMPERATURE OF A LOCAL MICROSCALE VOLUME WITH A MAGNETICALLY-RESPONSIVE THERMAL SENSOR

STATEMENT REGARDING FEDERALLY SPONSORED RESEARCH

[0001] This invention was made with United States Government support from the National Institute of Standards and Technology (NIST), an agency of the United States Department of Commerce. The Government has certain rights in this invention.

CROSS REFERENCE TO RELATED APPLICATIONS

[0002] This application claims the benefit of U.S. Provisional Patent Application Serial No. 63/245,088 (filed September 16, 2021), which is herein incorporated by reference in its entirety.

BRIEF DESCRIPTION

[0003] Disclosed is a magnetically-responsive thermal sensor for determining the temperature of a local microscale volume, the magnetically-responsive thermal sensor comprising: a magnetic nano-thermometer that comprises a main magnetic layer and a subordinate magnetic layer disposed on the main magnetic layer, such that: the main magnetic layer comprises a first magnetic material that: couples, via magnetic coupling, with the subordinate magnetic layer; or has a large change in magnetization as a function of temperature that produces a magnetic phase transition of the main magnetic layer; and the subordinate magnetic layer comprises a second magnetic material that: couples, via magnetic coupling, with the main magnetic layer; or has a large change in magnetization as a function of temperature that produces a magnetic phase transition of the subordinate magnetic layer, wherein the magnetic nano-thermometer produces a magnetic response from which the temperature of the local microscale environment is determined.

[0004] Disclosed is a process for determining the temperature of a local microscale volume with a magnetically-responsive thermal sensor, the process comprising: disposing the magnetically-responsive thermal sensor in the local

microscale environment, the magnetically-responsive thermal sensor comprising: a magnetic nano-thermometer that comprises a main magnetic layer and a subordinate magnetic layer disposed on the main magnetic layer, such that: the main magnetic layer comprises a first magnetic material that: couples, via magnetic coupling, with the subordinate magnetic layer; or has a large change in magnetization as a function of temperature that produces a magnetic phase transition of the main magnetic layer; and the subordinate magnetic layer comprises a second magnetic material that: couples, via magnetic coupling, with the main magnetic layer; or has a large change in magnetization as a function of temperature that produces a magnetic phase transition of the subordinate magnetic layer; a matrix in which the magnetic nano-thermometer are disposed; a coil disposed proximate to the magnetic nano-thermometer; and a sensor disposed proximate to the magnetic nano-thermometer; producing, by the coil, a magnetic field, wherein the magnetic field comprises an alternating magnetic field such that a field-free point or line is produced in a volume of the local microscale environment in which is disposed the magnetic nano-thermometer; subjecting the local microscale environment and the magnetic nano-thermometer to the magnetic field from the coil; producing, by the magnetic nano-thermometer, a magnetic response in response to the magnetic nano-thermometer receiving the magnetic field from the coil; receiving, by the sensor, the magnetic response from the magnetic nano-thermometer; producing, by the sensor, a sensor signal in response to receiving the magnetic response from the magnetic nano-thermometer; receiving, by the temperature analyzer, the sensor signal from the sensor; and determining, by the temperature analyzer, the temperature of the local microscale environment based on the magnetic response by obtaining frequency components in the sensor signal; comparing a set of harmonic frequency components to calibration data from which the temperature is obtained.

BRIEF DESCRIPTION OF THE DRAWINGS

[0005] The following description cannot be considered limiting in any way. Various objectives, features, and advantages of the disclosed subject matter can be more fully appreciated with reference to the following detailed description of the disclosed subject matter when considered in connection with the following drawings, in which like reference numerals identify like elements.

[0006] FIG. 1 shows a magnetically-responsive thermal sensor, according to some embodiments.

[0007] FIG. 2 shows a magnetically-responsive thermal sensor, according to some embodiments.

[0008] FIG. 3 shows a plurality of different shapes for a magnetic nano-thermometer, according to some embodiments.

[0009] FIG. 4 shows a magnetically-responsive thermal sensor, according to some embodiments.

[0010] FIG. 5 shows a perspective view of a magnetically-responsive thermal sensor that includes a pair of coils, according to some embodiments.

[0011] FIG. 6 shows: (A) an end view along a X-axis of the magnetically-responsive thermal sensor shown in FIG. 5 and (B) a cross-section along line A-A shown in panel A, according to some embodiments.

[0012] FIG. 7 shows a perspective view of a magnetically-responsive thermal sensor that includes two pair of coils, according to some embodiments.

[0013] FIG. 8 shows a perspective view of a magnetically-responsive thermal sensor that includes three pair of coils, according to some embodiments.

[0014] FIG. 9 shows a magnetically-responsive thermal sensor disposed in a local microscale environment on an architectural structure, e.g., a house, for determination of the temperature of the local microscale environment, according to some embodiments.

[0015] FIG. 10 shows a graph of a magnetization versus temperature for a magnetically-responsive thermal sensor, wherein the graph provides a temperature-dependent magnetic response of magnetic nano-thermometers, according to some embodiments.

[0016] FIG. 11 shows graphs that provide a magnetic response detected by sensors of magnetic nano-thermometers to an alternating magnetic field, according to some embodiments.

[0017] FIG. 12 shows transformation of data in FIG. 11 and a result of processing the magnetic response into frequency components, according to some embodiments.

[0018] FIG. 13 shows a ratio of frequency components for data shown in FIG. 11, according to some embodiments.

[0019] FIG. 14 shows graphs of normalized magnetization versus temperature for various composition of magnetic material for selective engineering of a temperature range of operation for magnetic nano-thermometers, according to some embodiments.

[0020] FIG. 15 shows a magnetic response of magnetic nano-thermometers to a near-zero alternating magnetic field, according to some embodiments.

[0021] FIG. 16 shows a magnetic response of magnetic nano-thermometers to a near-saturation alternating magnetic field, according to some embodiments.

[0022] FIG. 17: (a) Cyclic voltammetry of ruthenium film electrodes at room temperature and 10 mV/s in aqueous 0.003 mol/dm^3 K_2PtCl_4 + 0.1 mol/dm^3 $NiCl_2$ + 0.1 mol/dm^3 $NaCl_2$ with and without $B(OH)_3$, pH=2.5. Average currents measured during deposition of films with a 293 mC/cm^2 charge limit are shown as half circles. Plots including the second cycle are shown in FIG. 29. Chronoamperometric data corresponding to these points is included in FIG. 30. Coulombic efficiencies calculated using number densities from XRD and thicknesses determined from SEM images the constant potential deposition steps are shown in the inset. (b) Cyclic voltammogram of a 2 mm diameter platinum electrode in 0.1 mol/dm^3 $NaCl_2$ solutions with and without $B(OH)_3$.

[0023] FIG. 18: (a) X-ray diffraction (Cu K_α) of platinum nickel films potentiostatically electrodeposited on ruthenium sputtered silicon substrates in the absence and presence of 0.5 mol/dm^3 $B(OH)_3$, with a charge limit of 293 mC/cm^2. A diffraction pattern of the bare ruthenium film is included for reference. Measured in a 2θ configuration at a fixed incident angle of 1°. (b) Lattice parameters determined from the above data as a function of the composition as determined by EDX spectroscopy.

The Vegard line was drawn using literature platinum and nickel lattice parameters of 0.3524 nm and 0.39231 nm and, respectively.

[0024] FIG. 19: Rutherford backscattering spectra (2.0 MeV $^4He^{2+}$) of potentiostatically electrodeposited platinum nickel films on ruthenium sputtered silicon substrates, with deposition potential and charge limits noted at right. The presence or absence of 0.5 mol/dm^3 $B(OH)_3$ is indicated by the color of the traces (red and blue, respectively). A spectrum of a bare ruthenium film on a silicon substrate is also included for reference. Measured counts are shown as circles and fits of the total spectrum and of individual elements of the data are shown as solid lines.

[0025] FIG. 20: (a) X-ray photoelectron spectra of a platinum nickel film deposited at -0.60 V, with assignments of spectral features noted. Auger electrons are noted with ◊ markers. (b) Higher resolution spectra of the O 1s binding energy range for films deposited from solution without and with 0.5 mol/dm^3 $B(OH)_3$, indicated in blue and red, respectively at the potentials noted at left. Higher resolution spectra of selected energy ranges are included in FIG. 35. Spectra were measured with an Al K_α source. The films were deposited from aqueous 0.003 mol/dm^3 K_2PtCl_4 + 0.1 mol/dm^3 $NiCl_2$ + 0.5 mol/dm^3 NaCl at pH=2.5 solutions with and without $B(OH)_3$ with a time limit of 16 min.

[0026] FIG. 21: Composition (atomic basis) of electrodeposited platinum nickel films as a function of the deposition potential determined by EDX spectroscopy, RBS, and XPS. Points for the latter two were derived from data shown in FIG. 19 and 20, and FIG. 35. There are five RBS points corresponding to the RBS data, though not all are discernable due to overlap. Each EDX point corresponds to an individual sample. In (a) composition is expressed as the atomic fraction of Ni relative to the amount of Ni and Pt, and in (b) O content is expressed as a fraction of the amount of Ni, Pt, and O.

[0027] FIG. 22: (a) Median thicknesses of films deposited from solutions without and with 0.5 mol/dm^3 $B(OH)_3$ with a 293 mC/cm^2 charge limit measured by cross sectional imaging with SEM (points connected with lines) and RBS. (b) Thickness of a representative film measured by cross sectional SEM imaging across the face of the electrode (points), and step edge height around the perimeter

determined by optical profilometry (line). One of the SEM cross sectional images used in determining the thicknesses for this film is shown in the inset. Both measurements presented in (b) correspond to the same electrode, which was deposited at -0.5 V in a solution with 0.5 mol/dm^3 $B(OH)_3$. (c) Step edge profile around the electrode perimeter measured by optical profilometry after subtraction of the sloping baseline determined outside of the electrodeposited area. The scale bars for the in-plane axes are 6 mm, and that for the surface normal direction is 160 nm. For clarity, only heights immediately adjacent to the film edge are shown.

[0028] FIG. 23: Magnetization as a function of applied field at 300 K of electrodeposited platinum nickel films deposited at the potentials indicated at top without and with 0.5 mol/dm^3 $B(OH)_3$ with a charge limit of 293 mC/cm^2. comparison of the magnetization at the maximum applied field for these data with literature values is included in the supporting information.

[0029] FIG. 24: (a,b) Magnetization at an 8 kA/m (100 Oe) applied field as a function of temperature of platinum nickel films deposited at the indicated potentials and nickel contents in the absence and presence of 0.5 mol/dm^3 $B(OH)_3$ with a charge limit of 293 mC/cm^2. The above data were measured in a field cooled configuration. (c,d) Dimensionless magnetic thermosensitivity (S = T/M dM/dT) derived from the M vs T measurements shown in (a) and (b). The faint lines were calculated from the M vs T data in a point-by-point manner, and the lines were calculated from empirically selected functions and are included as a guide to the eye. Points were calculated only where the magnetization was between 8% and 90% of the maximum value in the M vs T plots. Thermosensitivity data for a platinum resistance thermometer and 10 kΩ (at 298.15 K) thermistor are included in (c) for comparison.

[0030] FIG. 25: Comparison of the $Pt_{1-x}Ni_x$ lattice parameters determined in the present work (circles) from the diffraction patterns in FIG. 18 with values reported in the literature for disordered $Pt_{1-x}Ni_x$. The dotted line connects lattice parameters reported for pure nickel and pure platinum. The methods by which these samples were produced are indicated in the legend: electrodeposition (EC), sputter deposition (SD), chemical vapor deposition (CVD), pulse laser deposition (PLD), high temperature methods (HT), thermal decomposition (TD), and an aerosol- based method (AE).

[0031] FIG. 26: A comparison of Curie temperatures of $Pt_{1-x}Ni_x$ films determined in the present work (circles) determined from the M vs T data in FIG. 8 with values reported in the literature. The films from the present work deposited with a 293 mC/cm^2 charge limit are connected by lines. Two unconnected points above and below the line had half and double this charge limit. The literature values are for samples produced by electrodeposition (EC), sputter deposition (SD), and high temperature methods (HT).

[0032] FIG. 27: Characterization of the bare $Ru/Ti/SiO_2/Si$ substrate by x-ray reflectivity. (left) Reflectivity vs momentum transfer Q_z, fit of the reflectivity data, and residuals. The inset shows the fitted x-ray scattering length density (SLD) – depth profile. (right) Best fit parameter values and 68% and 95% confidence intervals determined from the posterior distribution of Differential Evolution Adaptive Metropolis (DREAM) fit. Parameters named L0n_SLD indicate the SLD of the layer n, L0n_T indicates the thickness of the layer n in Angstroms, L0n_Intf indicates the layer n interfacial roughness as a fraction of the layer thickness. Instrumental parameters for background over/undersubtraction, intensity, and theta offset are given by “Backgr”, “Intens”, and “Th_Off”, respectively. The Si_Int parameter is the roughness of the SiO_2/Ti interface in Angstroms.

[0033] FIG. 28: (a) A diagram of the measurement geometry used for the Rutherford backscattering (RBS) measurements. (b) Correlation plots between parameters used in modelling the RBS data in the SIMNRA software package[1] for a $Pt_{1-x}Ni_x$ film deposited at -0.65 V vs SCE (saturated calomel electrode, KCl) with a charge limit of 586 mC/cm^2 (for which the RBS spectrum is included in figure 3). These parameters represent oxygen atomic fraction in the $Pt_{1-x}Ni_x$ layer (oxygen atoms per thousand atoms total), area specific number density of the $Pt_{1-x}Ni_x$ layer (“thickness” in $atoms/cm^2 \times 10^{15}$), and roughness of the $Pt_{1-x}Ni_x$ layer (in $atoms/cm^2 \times 10^{15}$). The platinum nickel ratio, which seemed fairly robust across different fits, was held constant, and the total amount of platinum and nickel was determined by the value of the oxygen parameter.

[0034] FIG. 29: Voltammograms of ruthenium film electrodes in 0.1 mol/dm^3 $NiCl_2$ + 3 $mmol/dm^3$ K_2PtCl_4 + 0.5 mol/dm^3 NaCl, pH=2.5 solutions (a) without $B(OH)_3$

and (b) with 0.5 mol/dm^3 $B(OH)_3$ showing the first and second cycle for comparison. Scan rate: 10 mV/s

[0035] FIG. 30: Plots of current vs time during the deposition of $Pt_{1-x}Ni_x$ films from aqueous 0.1 mol/dm^3 $NiCl_2$ + 3 mmol/dm^3 K_2PtCl_4 + 0.5 mol/dm^3 NaCl, pH=2.5 solutions (a) without $B(OH)_3$ and (b) with 0.5 mol/dm^3 $B(OH)_3$. The times for (a) and (b) have been normalized to the duration of the step, the duration of which was determined by the charge limit of 293 μC/cm^2. The step durations for both data sets are shown in (c). The color code for deposition potential is the same in all three of the above plots. The data correspond to the average current and Coulombic efficiency data shown in figure 1a of the main text.

[0036] FIG. 31: Voltammetry of a platinum disk electrode in 0.5 mol/dm^3 $B(OH)_3$ + 0.5 mol/dm^3 NaCl + 3 mmol/dm^3 HCl with three different lower potential limits. The redox couple at about -0.4 V vs SCE is attributed the reduction of protons furnished by H_3O and oxidation of the electrogenerated H_2. The more negative redox couple is attributed to reduction of protons furnished by $B(OH)_3$ and oxidation of hydrogen. The net current for the peak at more reducing potentials was negative, which suggests H_2 evolution and reduction were occurring simultaneously.

[0037] FIG. 32: (a) EDX spectra of a Pt_xNi_{1-x} film deposited at -0.50 V vs SCE in a solution with 0.5 mol/dm^3 $B(OH)_3$. This is the same film for which profilometry and a cross section are shown in figure 6b of the main text. The spectra collected over 80 μm by 160 μm areas across the face of the electrode, using a 10 kV accelerating voltage and 50× magnification. The spectra are offset in the vertical direction and cropped to a limited energy range for clarity. (b) Integration of the spectra in (a) over the highlighted energy ranges corresponding to oxygen, nickel, silicon, platinum, and ruthenium. The regions at either end of the range with more intense silicon, ruthenium, and oxygen peaks were outside of the area where platinum nickel was deposited. In the region where platinum and nickel were present, the gradients in intensity are indicative of a gradient in thickness, with the thickest region closer to the end of the electrode that was deepest in solution. (c) Ni L peak area as a fraction of the sum of the Ni L and Pt M peak areas. This indicates that the region of the film that was deepest in the solution was richer in platinum than the end that was

shallowest. Pieces of the film used for magnetic measurements were cleaved from near the center of the electrode.

[0038] FIG. 33: The points plotted at left were derived from EDX spectra of Pt_xNi_{1-x} films deposited in the presence and absence of 0.5 mol/dm^3 $B(OH)_3$, and are $1-I/I_0$, where I is the integrated area of the Si K peak or Ru L peak for a location where platinum and nickel were deposited, and I_0 is the integrated area for the same peak but in a location without electrodeposited platinum nickel. This is a relative indication of the thickness of the film – for a given platinum nickel content of the film, a smaller value on this plot indicates a thinner film.

[0039] FIG. 34: XPS data over energy ranges of interest for the Pt 4f and Ni 3p, and the Pt 4d, O 1s, and Ni 2p levels. For each, deposition potentials vs SCE are indicated at right. Data for films deposited from 0.5 mol/dm^3 boric acid-containing solutions are marked in red, and those deposited from boric acid free-solutions are marked in blue.

[0040] FIG. 35: Helium ion microscope image of a cleaved cross section of $Pt_{1-x}Ni_x$ (x=0.79) deposited at -0.65 V vs SCE with a charge limit of 586 mC/cm^2. RBS characterization of this film is included in figure 3 of the main text, and M vs T characterization is included in figure S11. From bottom to top, the visible layers are silicon, silicon oxide, ruthenium, $Pt_{1-x}Ni_x$, and vacuum.

[0041] FIG. 36: A comparison of magnetization at a 5.6 MA/m applied field vs mole fraction of Ni for Pt_xNi_{1-x} films electrodeposited from solutions without and with 0.5 mol/dm^3 $B(OH)_3$.

[0042] FIG. 37: M vs T measurements on three films deposited at the same potential, but with different charge limits (146 mC, 293 mC, and 586 mC), and hence with different thicknesses (30 nm, 60 nm, and 116 nm). RBS data measured on these three films are shown in figure 3 of the main text. Nickel contents determined by SEM and RBS, the later noted above, varied little with charge limit.

[0043] FIG. 38. XRD of presentative ferrite seed material indexed to the inverse spinel structure, ferrite/CoO nanoflowers with majority ferrite phase,

ferrite/CoO clusters with majority CoO phase, and CoO indexed to the cubic rock salt structure.

[0044] FIG. 39. TEM images and corresponding size distributions determined from TEM and DLS of ferrite particles (a,d), ferrite/CoO nanoflowers (b,e), ferrite/CoO clusters (c,f). The large (> 50 nm) object observed in the TEM image of the nanoflowers is most likely a drying artifact from sample preparation. Values for TEM and DLS size were rounded to whole number. Red circles with arrows indicating the length measured and show the approximate objects that remain intact when dispersed in hexane. In the high-resolution TEM images the d-spacings were determined by averaging over the line indicated by arrows. The crystal planes are labeled.

[0045] FIG. 40. Scanning transmission electron microscopy image with superposition of cobalt (red) and iron (green) elemental mapping of nanoflower sample showing irregular shaped particle (a) and more spherical particle (b).

[0046] FIG. 41. Raman spectroscopy measured at a wavelength of 785 nm and power of 3.8 mW of representative ferrite particles (black), ferrite/CoO nanoflowers (green), ferrite/CoO clusters (red), and CoO (blue). The background has been subtracted from the data.

[0047] FIG. 42. Liquid (hexanes) (ZFC) magnetization vs. temperature measured in a DC field of 10 mT (a), liquid ZFC measurements normalized by the maximum magnetization between 200 K and 310 K (b), liquid magnetization vs. field hysteresis loops measured at 100 K after cooling in a DC field of 1 T (c), and liquid magnetization vs. field hysteresis loops measured at 300 K (d). All samples were in hexane with the nanoflowers and clusters having an approximate concentration of 10 mg solids/mL, the ferrite sample had an approximate concentration of 20 mg solids/mL. Error bars are shown for a, c, and d but are smaller than the data point.

[0048] FIG. 43. AC susceptibility measurement of the nanoflowers at temperatures between 200 K and 300 K (a), and DC ZFC plotted alongside the ACS at 1 kHz as a function of temperature of the nanoflowers.

[0049] FIG. 44. Liquid (hexanes) room temperature MPS measured at a drive peak amplitude of about 14 mT (10 mT RMS) and a frequency of 1 kHz (a) and a drive peak amplitude of about 21 mT (15 mT RMS) and a frequency of 1 kHz (b). The samples were in hexane and normalized by the mass of solid material in kilograms, estimated based on the approximate concentration of the samples.

[0050] FIG. 45. Thermosensitivity curves calculated from the liquid DC ZFC measurements for the ferrite particles, nanoflowers, and clusters.

[0051] FIG. 46. Morphology, precursor quantities, precursors, and size characterization summary MNOs. The two DLS size values shown were obtained from measurement of samples with different concentrations. The label of (main peak) in a DLS measurements indicates there were additional larger objects that were a minority in the sample. Samples in bold are the focus of this work. The Ni doped cluster-like samples are labeled S1 through S4 to identify them in the measurement data presented in the SI.

[0052] FIG. 47. Line scans of STEM elemental maps with corresponding counts vs. position across the nano-objects showing Co (red, squares) and Fe (green, circles).

[0053] FIG. 48. STEM image with superposition of cobalt (red) and iron (green) elemental mapping of nanoflower sample showing irregular shaped particle.

[0054] FIG. 49. Fitting of Raman spectrum using Voigt/PsdVoigt functions of representative ferrite particles (a), CoO (b), ferrite/CoO nanoflowers (c), ferrite/CoO clusters (d) at 785 nm wavelength and 3.8 mW power. Ni-doped ferrite/CoO clusters (S1) at 785 nm and 0.65 mW power (c) and at 1.98 mW power (d) showing structural change with laser power not observed in the samples without Ni doping under these measurement conditions.

[0055] FIG. 50. Liquid (hexanes) Zero-field cooled (ZFC) and field cooled (FC) of representative ferrite particles with concentration of about 20 mg solids/mL (a), liquid (hexanes) ZFC and FC of nanoflowers (b), and ZFC and FC of clusters (c) with concentrations of about 10 mg solids/mL. Samples are in hexane and normalized by the total mass, solid material and solvent.

[0056] FIG. 51. Liquid (hexanes) ZFC and FC of Ni-doped cluster-like samples and corresponding exchange bias measurements at 100 K. Sample in (a,b) had concentration of approximately 10 mg solids/mL and samples in (c,d) had concentrations of approximately 10 mg solids/mL. All samples were normalized by the total mass, material, and solvent.

[0057] FIG. 52. Fast Fourier transform (FFT) of MPS intensity vs. time measured at a drive field peak amplitude of 21 mT and frequency of 1 kHz of ferrite particles (a), ferrite/CoO nanoflowers (b), Ni doped ferrite/CoO clusters (S1) (c), and ferrite/CoO clusters (d).

[0058] FIG. 53. Liquid (hexanes) room temperature magnetic particle spectroscopy (MPS) measured with an AC drive field peak amplitude of 14 mT (10 mT RMS) and a frequency of 7 kHz. The samples are in hexanes and normalized by the total mass of solid material in kilograms, estimated based on the approximate concentration of the samples.

[0059] FIG. 54. Powder zero-field cooled magnetization vs. temperature measured in a 10 mT DC field (a) and powder real part of the AC susceptibility measured in an AC field of 1.5 mT and 7 kHz, measurement started at 400 K and decreased. Both measurements were normalized by the total mass of the dried sample. Dashed vertical lines at 300 K and 340K are guides to the eye and not meant to indicate a maximum magnetization of any particular sample but illustrate shift between DC and 7 kHz AC measurements.

DETAILED DESCRIPTION

[0060] A detailed description of one or more embodiments is presented herein by way of exemplification and not limitation.

[0061] Conventional temperature sensors, e.g., a thermocouples, can be accurate and require wired connections that can be invasive and have a macroscopic footprint so that the thermocouple can be incompatible with high-density and dispersed measurements throughout a heterogeneous volume. Non-contact surface temperature mapping methods conventionally include infrared thermography and thermoreflectance with microscale spatial resolution and 10 mK thermal resolution.

However, these devices do not provide information from a specified volume within a sample. Nanodiamond with nitrogen-vacancy centers have 10 mK thermal resolution and involve optically transparent materials to measure a signal, and technology is absent for remote measurement of temperature throughout a volume with high accuracy and precision.

[0062] Conventional single-phase magnetic nanoparticles have a change in magnetization with temperature that is weak, especially near room temperature. Past magnetic thermometry work at room temperature on these materials have a single average temperature (with resolution > 250 mK over a 1 s measurement) for undiluted (high MNO concentration), macroscopic (> 1 cm^3) samples. Accordingly, there is an unmet but long-felt need for remote measurement of temperature throughout a volume with high accuracy and precision.

[0063] A number of emerging and established fields need remote measurement of the temperature throughout a volume. These include in heat exchangers, which are becoming ever more critical for cooling electronics; electronics for mapping failure points; fuel cells; thermal transport in nanofluids; in chemical reactions and reactors, especially micro-reactors; in biological processes and bio-reactors, especially for local control over heat-induced cell damage or thermally-activated local release of chemical agents for medicine; in materials processing, especially additive manufacturing of polymer melts whose properties are very dependent upon temperature, and across a wide range of combustion issues, where temperature control is critical. All of these involve remote and accurate measurement of temperature throughout a volume, over a range of rate, without perturbing the system.

[0064] There currently exists no method to measure temperature accurately and remotely throughout a 3D volume with microscale precision, and the magnetically-responsive thermal sensor described fills this void.

[0065] The magnetically-responsive thermal sensor described herein provide an advance from spatially unresolved temperature measurements to spatially resolved (3-Dimensional), high-sensitivity measurements of temperature and advantageously include dispersed nanoscale thermometers. In addition, the

magnetically-responsive thermal sensor has a physical property that changes rapidly with temperature for high sensitivity and is traceable to either the International Temperature Scale of 1990 (ITS-90) or has a direct link to the SI definition of the Kelvin.

[0066] For conventional magnetic nano-objects (MNOs), the change in magnetization with temperature is weak, especially near room temperature (RT). Past magnetic thermometry included single-phase nanoparticles, yielding only a single average temperature (with resolution > 250 mK over a 1 s measurement) for undiluted (high MNO concentration), macroscopic (> 1 cm3) samples. However, and beneficially, the magnetically-responsive thermal sensor includes a main magnetic layer and a subordinate magnetic layer with sharp temperature features in magnetization, and each layer can include a different magnetic material. Some magnetic materials can be selected sucha that one layer must has a strong temperature dependence (e.g., Curie temperature in the temperature range of interest, or the layers can have magnetic moments that are anti-parallel at the interface.

[0067] It has been discovered that a magnetically-responsive thermal sensor a process for determining the temperature of a local microscale volume described herein provide measurement of the temperature in the local microscale volume when the magnetic nano-thermometer is queried by an alternating magnetic field. A collection of these magnetic nano-thermometers distributed throughout a volume can measure the temperature distribution throughout that volume.

[0068] Magnetically-responsive thermal sensor 200 determines the temperature of a local microscale volume. In an embodiment, with reference to FIG. 1, FIG. 2, FIG. 3, FIG. 4, FIG. 5, FIG. 6, FIG. 7, FIG. 8, FIG. 10, FIG. 11, FIG. 12, FIG. 13, FIG. 14, FIG. 15, and FIG. 16, magnetically-responsive thermal sensor 200 includes: magnetic nano-thermometer 201 that includes main magnetic layer 202 and subordinate magnetic layer 203 disposed on main magnetic layer 202, such that: main magnetic layer 202 includes a first magnetic material that: couples, via magnetic coupling, with subordinate magnetic layer 203; or has a large change in magnetization as a function of temperature that produces a magnetic phase transition of main magnetic layer 202; and subordinate magnetic layer 203 includes a second magnetic material that: couples, via magnetic coupling, with main magnetic layer 202; or has a

large change in magnetization as a function of temperature that produces a magnetic phase transition of subordinate magnetic layer 203, wherein magnetic nano-thermometer 201 produces magnetic response 210 from which the temperature of local microscale environment 213 is determined.

[0069] In an embodiment, magnetically-responsive thermal sensor 200 includes matrix 205 in which magnetic nano-thermometer 201 are disposed.

[0070] In an embodiment, magnetically-responsive thermal sensor 200 include coil 207 disposed proximate to magnetic nano-thermometer 201 and that subjects magnetic nano-thermometer 201 to magnetic field 209.

[0071] In an embodiment, magnetic nano-thermometer 201 includes a plurality of coil 207 arranged as a pair that is opposingly disposed such that magnetic nano-thermometer 201 is interposed between each coil 207 of pair of coils.

[0072] In an embodiment, magnetic nano-thermometer 201 includes single pair of coils, two pairs of coils, or three pairs of coils, such that each coil in a pair is independently controlled, and each pair of coils is independently controlled to produce a separate and orthogonally oriented magnetic field 209.

[0073] In an embodiment, magnetic nano-thermometer 201 receives magnetic field 209 and produces magnetic response 210 in response to magnetic field 209.

[0074] In an embodiment, magnetically-responsive thermal sensor 200 includes sensor 208 disposed proximate to magnetic nano-thermometer 201 and that receives magnetic response 210 from magnetic nano-thermometer 201 and produces sensor signal 211 based on magnetic response 210 received from magnetic nano-thermometer 201.

[0075] In an embodiment, sensor 208 includes a pick-up coil, a superconducting quantum interference device, a hall sensor, a flux gate, a magnetoresistive sensor, or a combination comprising at least one of the foregoing type of sensor.

[0076] In an embodiment, magnetically-responsive thermal sensor 200 includes temperature analyzer 212 in electrical communication with sensor 208 and that receives sensor signal 211 from sensor 208 and determines temperature of local microscale environment 213 based on magnetic response 210 produced by magnetic nano-thermometer 201.

[0077] In an embodiment, magnetic nano-thermometer 201 includes medial magnetic layer 204 disposed on main magnetic layer 202 and interposed between main magnetic layer 202 and subordinate magnetic layer 203.

[0078] In an embodiment, medial magnetic layer 204 includes a non-magnetic material and facilitates antiferromagnetic coupling between main magnetic layer 202 and subordinate magnetic layer 203.

[0079] In an embodiment, magnetic nano-thermometer 201 includes substrate 206 on which is disposed main magnetic layer 202 and subordinate magnetic layer 203 and arranged in pillar structure 217 on substrate 206.

[0080] In an embodiment, magnetic nano-thermometer 201 includes core-shell structure 216 including core 214 and shell 215 disposed on and surrounding core 214, wherein main magnetic layer 202 is arranged in core 214 and subordinate magnetic layer 203 is arranged in shell 215.

[0081] In an embodiment, magnetic nano-thermometer 201 includes a plurality of main magnetic layer 202 and a plurality of subordinate magnetic layer 203 arranged so that layers of main magnetic layer 202 and layers of subordinate magnetic layer 203 sequentially alternate in magnetic nano-thermometer 201.

[0082] In an embodiment, main magnetic layer 202 includes iron. In an embodiment, subordinate magnetic layer 203 includes gadolinium.

[0083] In an embodiment, the magnetic coupling between main magnetic layer 202 and subordinate magnetic layer 203 is antiferromagnet coupling. In an embodiment, the magnetic coupling between main magnetic layer 202 and subordinate magnetic layer 203 is ferromagnetic coupling.

[0084] In an embodiment, matrix 205 includes a solid, a fluid, or a combination comprising at least one of the foregoing states of matter.

[0085] As used herein, a large change in magnetization refers to a thermosensitivy S of at least 1, [e.g., from 0.01 to 10^{15}, specifically from 1 to 10^{12}, and more specifically from 1 to 500. It should be appreciated that thermosensitivity S unitless, per S=(T/M)(dM/dT), wherein T is temperature; M is the magnetic moment or magnetization; and dM/dT is the first derivative of the magnetic moment or magnetization with respect to the temperature. It is contemplated that thermosensitivity S is defined over a temperature range, e.g., 100 K to 275 K. Moreover, the magnetic phase change is between different magnetic phases of the magnetic material, e.g., of main magnetic layer 202, subordinate magnetic layer 203. The different magnetic phases can involve different magnetic ordering states. It is contemplated that the different magnetic phases are a ferromagnetic, ferrimagnetic, or antiferromagnetic phase at a lower temperature and a paramagnetic phase at a higher temperature.

[0086] Elements of magnetically-responsive thermal sensor 200 can be various sizes and can be made of a material that is physically or chemically resilient in an environment in which magnetically-responsive thermal sensor 200 is disposed. In an embodiment, magnetic nano-thermometer 201 includes at least two layers of magnetic material. The magnetic material can be an elemental metal (Fe, Gd, Co, Ni), an alloy of the elemental metal, or an oxide, nitride, carbide, or boride of the elemental metal. These layers (202, 203) couple together to produce a magnetic nano-object with a large change in the magnetization as a function of temperature. These magnetic nano-objects can are disposed in matrix 205 (e.g., a solid or fluid) that is probed with magnetic field 209 to accurately measure the local temperature of local microscale environment 213 with minimal disturbance of the environment. The number of layers and format (e.g., globular format as shown in FIG. 2 (a cross-section of a spherical magnetic nano-thermometer 201) or pillar format as shown in FIG. 4 can be used although other regular and irregular shapes of magnetic nano-thermometer 201 are contemplated, each with at least a bilayer of layer 202 and layer 203 or more layers, such as arbitrary number n of layers (202, 203). The magnetic material in layers (202, 203) can include an elemental metal (Fe, Gd, Co, Ni), an alloy of the elemental metal

(Fe, Co, Ni, Gd alloyed with one or more of the following Al, Si, Ti, V, Cr, Mn, Fe, Co, Ni, Cu, Zn, Ga, Ge, As, Se, Y, Zr, Nb, Mo, Ru, Rh, Pd, Ag, Ir, Pt, Au, La, Ce, Pr, Nd, Sm, Eu, Gd, Tb, Dy, Ho, Er), or an oxide, nitride, carbide, or boride of the elemental metal or alloy. At least one of these layers has a magnetic transition in the desired temperature range, such as a ferromagnetic-paramagnetic (Curie temperature) or anti-ferromagnetic-paramagnetic (Neel temperature) or potentially both (for ferrimagnets). The other layer must couple anti-ferromagnetically across the interface with the first material. These two requirements, when the total size of the multi-layer magnetic nano-object is less than 100 nm, result in large changes in the magnetization as a function of temperature around the desired temperature range. This large change can be linear or monotonic. The large change in magnetization as a function of temperature means that a magnetic field applied remotely can measure the signal difference of the magnetic nano-object when at different temperatures and identify the different temperatures with high accuracy and precision.

[0087] In an embodiment, magnetically-responsive thermal sensor 200 includes a bilayer (or more layers) of magnetic nano-objects (MNOs) as dispersed magnetic nano-thermometer 201 to measure the temperature locally (microscale resolution) throughout a three-dimensional volume with time resolution. Magnetically-responsive thermal sensor 200 operates in an absense or presence of optical transparency or macroscopic sample size (such as with thermocouples). The choice of the magnetic materials and thicknesses provide a magnitude of the temperature sensitivity of the magnetic moment or a temperature range of the temperature sensitivity. By coupling one layer with a strong temperature dependence (e.g., Curie temperature in the temperature range of interest) and a second layer that magnetically aligns anti-parallel across the interface, the behavior becomes temperature dependent while maintaining a strong signal that is measured as magnetic response 210. The MNOs can be dispersed (not necessarily uniformly) inside another material (fluid or solid) and probed with AC magnetic fields with spatial resolution to read the measured magnetic moment. After calibration, this moment is translated into a local temperature, and the distribution of temperature throughout a volume can be determined.

[0088] In an embodiment, coil 207 is a metal (e.g., copper) or superconductor that produce alternating magnetic field 209 from which magnetic

nano-thermometer 201 produces magnetic response 210. There can be a single pair of coils, two pairs of coils, or three pairs of coils, where each coil in a pair can be controlled independently, and each pair can be controlled independently. The coil pairs can be arranged orthogonally to each other. The control for a given coil is the amount of current run through the coil. This control enables the movement of a field-free point or line for isolating the magnetic volume to be read. The frequency and amplitude of the alternating field can be variable. Litz wire can be used as the winding so that the resistance of the coil does not change with frequency, changing the amplitude at a given operating voltage.

[0089] Magnetically-responsive thermal sensor 200 measures the temperature in the local microscale volume when the magnetic nano-thermometer is queried by an alternating magnetic field. The magnetic nano-thermometer has a large change in the magnetization over a selected temperature range. This large change occurs by virtue of main magnetic layer 202 or subordinate magnetic layer 203 having a magnetic phase change, creating a temperature-dependent magnetization, or coupling, e.g., antiferromagnetically, between main magnetic layer 202 and subordinate magnetic layer 203. The temperature range can be shifted by changing the choice of magnetic materials in main magnetic layer 202 and subordinate magnetic layer 203 or by changing the thickness or composition of medial magnetic layer 204.

[0090] In an embodiment, a plurality of magnetic nano-thermometer 201 is disposed in matrix 205 or disposed on substrate 206, wherein the spatial or volumetric distribution of magnetic nano-thermometer 201 can be uniform or nonuniform. Neighboring magnetic nano-thermometers 201 can interact magnetically, which can be used to tune the collective magnetic anisotropy for improved signal to noise.

[0091] Magnetically-responsive thermal sensor 200 can be made in various ways. It should be appreciated that magnetically-responsive thermal sensor 200 includes a number of optical, electrical, or mechanical components, wherein such components can be interconnected and placed in communication (e.g., optical communication, electrical communication, mechanical communication, and the like) by physical, chemical, optical, or free-space interconnects. The components can be disposed on mounts that can be disposed on a bulkhead for alignment or physical

compartmentalization. As a result, magnetically-responsive thermal sensor 200 can be disposed in a terrestrial environment or space environment.

[0092] In an embodiment, a process for making magnetically-responsive thermal sensor 200 includes, e.g., colloidal chemical synthesis, electrochemical deposition with or without lithography, or physical deposition with lithography. Such methods are described in the following, which is incorporated by reference in its entirety: "Synthesis of very fine maghemite particles," Journal of Magnetism and Magnetic Materials, Volume 149, Issues 1–2, August 1995, pages 6-9.

[0093] In colloidal chemical synthesis, starting material, solvent, or ligand is can be varied or optimized in a synthetic steps that can include thermodecomposition, use of a polyol (organic compound with multiple hydroxyl groups) as starting material, or a chemical reaction. In electrochemical deposition oxidation and reduction deposit a material onto a substrate by using electrodes to control the current and potential in the electrolyte. In physical deposition (e.g., thermal evaporation, sputter deposition, molecular beam epitaxy, or atomic layer deposition), thermal evaporation heats, in a vacuum chamber, the material being deposited to a high enough temperature that it sublimates and then deposits on the much colder substrate. Sputter deposition uses other atoms, such as argon, to physically knock atoms of the material to be deposited off the target and into the vacuum chamber, where they deposit on the substrate. Molecular beam epitaxy involves beams of atoms from a heated target, under ultra-high vacuum, which then impact the substrate, forming an epitaxial layer. Atomic layer deposition (ALD), a variant of chemical vapor deposition, pulses the gaseous precursors one at a time in the reaction chamber to form the desired material via chemical surface reactions on a substrate.

[0094] With electrochemical deposition or physical deposition, the structure is patterned to form the nano-objects. This can be done by depositing into a pre-existing patterned structure such as an anodized alumina matrix or by pre- or post-patterning the substrate using lithography.

[0095] Lithography (e.g., photolithography, e-beam lithography, or imprint lithography) involve a pre-formed mask that has the pattern to be used and a resist on the surface of the substrate to contain the pattern. Photolithography involves the use

of visible light through the mask to expose a photo-active resist and change the exposed areas dissolution rate in a solvent; e-beam lithography uses a rastered electron beam, that follows a CAD mask, to expose the e-beam resist and change its dissolution rate in solvent, and imprint lithography brings the mask into contact with a film of thermoplastic polymer resist on a substrate, displacing the polymer three-dimensionally during the imprint due to the high pressure exerted. The resist can then be dipped in solvent to expose the pattern. Depending on the specific recipe, the desired material can be deposited into the pattern, or the extra material can be removed using a process like reactive ion etching. This process is repeated until the final structure is formed. Once the final structure is formed, it can be used as is, or the nano-thermometers must be released from the substrate by chemically etching away a sacrificial layer or the substrate itself, without damaging the structure of 100. Once released into solution, they can be stabilized by a surfactant to prevent irreversible agglomeration.

[0096] Coil 207 can be made by winding wire or tape of a conducting material such as copper or a superconductor into a uniform solenoid with a known number of turns and a defined current carrying capacity. Since the applied magnetic field is alternating at variable frequency, Litz wire can be used so that the resistance does not change with frequency that could affect the amplitude of the generated field.

[0097] Magnetically-responsive thermal sensor 200 has numerous advantageous and unexpected benefits and uses. In an embodiment, , a process for determining the temperature of a local microscale volume with magnetically-responsive thermal sensor 200 includes: disposing the magnetically-responsive thermal sensor 200 in the local microscale environment 213, the magnetically-responsive thermal sensor 200 including: a magnetic nano-thermometer 201 that comprises a main magnetic layer 202 and a subordinate magnetic layer 203 disposed on the main magnetic layer 202, such that: the main magnetic layer 202 comprises a first magnetic material that: couples, via magnetic coupling, with the subordinate magnetic layer 203; or has a large change in magnetization as a function of temperature that produces a magnetic phase transition of the main magnetic layer 202; and the subordinate magnetic layer 203 comprises a second magnetic material that: couples, via magnetic coupling, with the main magnetic layer 202; or has a large

change in magnetization as a function of temperature that produces a magnetic phase transition of the subordinate magnetic layer 203; a matrix 205 in which the magnetic nano-thermometer 201 are disposed; a coil 207 disposed proximate to the magnetic nano-thermometer 201; and a sensor 208 disposed proximate to the magnetic nano-thermometer 201; producing, by the coil 207, a magnetic field 209, wherein the magnetic field 209 comprises an alternating magnetic field such that a field-free point or line is produced in a volume of the local microscale environment 213 in which is disposed the magnetic nano-thermometer 201; subjecting the local microscale environment 213 and the magnetic nano-thermometer 201 to the magnetic field 209 from the coil 207; producing, by the magnetic nano-thermometer 201, a magnetic response 210 in response to the magnetic nano-thermometer 201 receiving the magnetic field 209 from the coil 207; receiving, by the sensor 208, the magnetic response 210 from the magnetic nano-thermometer 201; producing, by the sensor 208, a sensor signal 211 in response to receiving the magnetic response 210 from the magnetic nano-thermometer 201; receiving, by the temperature analyzer 212, the sensor signal 211 from the sensor 208; and determining, by the temperature analyzer 212, the temperature of the local microscale environment 213 based on the magnetic response 210 by obtaining frequency components in the sensor signal 211; comparing a set of harmonic frequency components to calibration data from which the temperature is obtained. Obtaining the frequency component can occur via Fourier transformation of sensor signal 211.

[0098] The articles and processes herein are illustrated further by the following Example, which is non-limiting.

EXAMPLES

EXAMPLE 1

[0099] Magnetic Characterization of Electrodeposited Pt1-xNix Alloy Films: Influence of Deposition Potential and the Presence of Boric Acid

[00100] Pt1-xNix (x = 0.25 to 0.92) thin films were examined for possible application as magnetic thermometers. The alloys were prepared by charge-limited potentiostatic electrodeposition from aqueous chloride-based solutions in the presence and absence of 0.5 mol/dm^3 $B(OH)_3$. Alloy composition was controlled by

the deposition potential with the Ni concentration increasing towards more reducing potentials. Films with x>0.45 were ferromagnetic with the magnetization at 300 K increasing with nickel content. Magnetization vs temperature (M vs T) at 8 kA/m (100 Oe) showed an increase in the Curie temperature from less than 200 K to above 400 K for the alloys investigated. For films deposited at potentials >-0.6 V vs the saturated calomel electrode (SCE), boric acid had negligible effect on the magnetization at the maximum applied field in M vs H measurements. In contrast, for depositions at more reducing potentials <-0.6 V vs SCE the presence of boric acid resulted in diminished magnetization. This effect was attributed to elevated incorporation of oxygen (up to ~4 atomic %), along with boron incorporation of about 400 µmol/mol.

[00101] Alloy electrodeposition offers a versatile approach to producing materials and structures with application-specific physical and chemical properties by varying processing parameters such as applied potential or current and solution composition. Optimization of the deposition conditions has been used to tune the magnetic characteristics such as magnetization, coercivity, and giant magnetoresistivity, that are important in data storage applications. The Curie temperature is another magnetic property that can be tailored via selection of electrodeposition conditions. For many applications, thermosensitive magnetic properties are often undesired. However, such properties can be of specific interest for temperature sensing, magnetocaloric cooling, heat assisted magnetic recording, and all optical switching of magnetization.

[00102] The platinum nickel system has been widely studied for its magnetic, catalytic, and structural properties. The compositions of $Pt_{1-x}Ni_x$ and other platinum alloys can be controlled via the potential at which they are electrodeposited, and the composition can be used to adjust the Curie temperature.

[00103] Previous work with electrodeposited platinum alloy films has been done in the presence and absence of boric acid, although its effect on the magnetic properties of the resulting films has not been investigated. Boric acid is commonly used in solutions for the electrodeposition of iron group metals (Fe, Co, Pt) and of alloys incorporating these metals to avoid precipitation of hydroxide species. The beneficial effect of boric acid has been attributed to diminution of the change in interfacial pH due to hydrogen evolution via some combination of its buffering action,

blocking of hydrogen evolution via competitive adsorption, or possibly a catalytic effect. Complexation of metal cations by boric acid or boric-acid derived species might also play a role. Minimization of interfacial pH changes during deposition is of particular concern for high aspect ratio nanostructured templates, such as anodic aluminum oxide.

[00104] In the present study, the effect of boric acid on the electrodeposition of $Pt_{1-x}Ni_x$ alloys, and the magnetic properties of the resulting alloys, are examined. Of particular interest is developing materials with magnetic thermosensitivity between 200 K and 400 K for use as magnetic thermometers.

[00105] Experimental

[00106] Electrochemistry

[00107] All depositions were carried out in a potentiostatic three-electrode configuration, using a platinum sheet counter electrode and an Ag/AgCl (0.5 mol/dm^3 NaCl) reference electrode using a BioLogic VSP potentiostat. Prior to each series of depositions, the Ag/AgCl reference was checked against a saturated calomel electrode (SCE, saturated KCl), and all potentials herein are reported with respect to this reference. The reference electrode was kept in a separate compartment connected to the main cell with a 3 mmol/dm^3 HCl + 0.5 mol/dm^3 NaCl-filled polytetrafluoroethylene tube. Solutions were deaerated with ultrahigh purity argon prior to depositions, and the gas flow was directed over the top of the cell during depositions. The cell held a 100 cm^3 volume of solution. The working and counter electrodes were held approximately vertical.

[00108] Solutions were prepared using potassium tetrachloroplatinate, nickel (II) chloride hexahydrate, and boric acid from Alfa (99.99%, 99.95%, 99.99% metals basis, respectively) with a sodium chloride from Taychemco (ACS Grade). The solution pH was adjusted to 2.5 by additions of 1 mol/dm^3 HCl.

[00109] Substrate preparation

[00110] Boron-doped, 0.01 Ω cm to 0.02 Ω cm, 525 μm thick, 100 oriented, prime grade silicon substrates with a 300 nm thick thermal oxide (University Wafer,

2946) served as a substrate for the platinum nickel films. Prior to electrodeposition a ruthenium seed layer and a titanium adhesion layer (43.2 nm and 6 nm, respectively) were deposited using a radio frequency sputtering system (AJA International Inc.) at 7.4 W/cm^2 and 4.9 W/cm^2 respectively with a substrate temperature of 350 °C while rotating the substrate at about 0.25 Hz. The silicon thermal oxide and the adhesion layer were needed to avoid silicide formation during deposition and delamination due to stresses evolved during electrodeposition. Wafers were cleaved to pieces about 16 mm on a side prior to depositing films. The electrode area exposed to solution was defined by 3M Electroplating Tape 470 with a punched 11.1 mm or 12.7 mm (7/16 inch or 1/2 inch) diameter circular hole. The wafer piece was affixed to a glass microscope slide to facilitate handling. Electrical contact to the seed layer was made via a strip of copper foil about 2 mm wide which contacted one edge of the wafer piece, and which was protected from the solution on one side by the tape and on the other by the microscope slide. All films were deposited with a charge limit of 293 mC/cm^2, which would result in a film 100 nm thick assuming 100% coulombic efficiency and the density of elemental nickel (8.908 g/cm^3, given a lattice parameter of 0.3524 nm).[55] The electrodeposited films were removed from solution within seconds of the end of the deposition to minimize galvanic displacement of nickel in the substrate by tetrachloroplatinate in the solution.

[00111] X-ray diffraction and reflectivity

[00112] X-ray diffraction measurements (XRD) were made using a Bruker D8 Advance diffractometer with a Dectris Eiger2R 500K detector in a 2θ scan configuration with a fixed incident angle of 1°, with Cu K_α radiation. Montel optics removed the K_β contribution, but the beam had $K_{\alpha1}$ and $K_{\alpha2}$ contributions. A 0.1 mm incident slit limited the footprint of the beam on the sample to 6 mm in the line formed by the intersection of the surface and the plane of incidence. The glancing angle configuration was chosen to decrease the depth to which the beam penetrated the sample. The $Pt_{1-x}Ni_x$ lattice parameters represent the average of the values determined from the positions of the (111) and (200) peaks, assuming a fcc structure. Only the (200) peak position was used in cases in which the (111) peak position was ambiguous due to overlap with diffraction peaks from the Ru substrate.

[00113] X-ray reflectivity (XRR) measurements were made using a Rigaku SmartLab diffractometer with a D/teX Ultra silicon strip detector and a Cu rotating anode source. A parallel incident beam-configuration and 0.052 mm incident slit width were used. A Ge (220) two bounce monochromator on the incident side was used to remove the $K_{\alpha 2}$ contribution. The reflectivity data and fit using Refl1D[56] for the Ru substrate film may be found in the supporting information FIG. 27.

[00114] Rutherford backscattering spectroscopy

[00115] Rutherford backscattering spectroscopy (RBS) was carried out using 2.0 MeV $^4He^{2+}$ ions, with a scattering angle of 163° and a sample-detector distance of 5 cm. The incident beam was perpendicular to the sample surface and had a footprint about 2 mm across. A silicon surface barrier detector with an energy resolution of 18 keV was used to detect the scattered ions. A diagram of the measurement geometry is included in the supporting information FIG. Analysis of the RBS data was carried out using the SIMNRA software package.[57] Data measured on a piece of the bare ruthenium-sputtered substrate were fit first using initial parameter values taken from fits of XRR data. The layer structure determined for the bare substrate was then held fixed in subsequent fitting of parameters for electrodeposited films. The electrodeposited $Pt_{1-x}Ni_x$ and ruthenium layer roughness were fit with a gamma distribution; the underlying layers were assumed to have negligible roughness.

[00116] X-ray photoelectron spectroscopy

[00117] X-ray photoelectron spectroscopy (XPS) measurements were made using a Kratos Analytical AXIS Ultra DLD spectrometer with a monochromatic Al K_α source (1486.69 eV) and pass energies of 20 eV and 80 eV for narrow range and survey spectra, respectively. XPS spectra were analyzed using CasaXPS (2.3.24PR1.0). The Pt 4d, Ni 2p, C 1s, and O 1s and Kratos C relative sensitivity factors were used for assessing the composition. A U 2 Tougaard function was used to determine the background subtraction for the first three of these transitions, but a linear background was used for the O 1s. The O 1s binding energy is slightly higher than the Pt 4p line, and the sloping baseline associated with the Pt 4p appeared to interfere with the application of the U 2 Tougaard background. Shirley background subtraction yielded nickel contents that were slightly lower than those obtained with

the Tougaard approach. The Pt 4d and Ni 2p lines were used as these were in relatively isolated ranges of the spectrum, unlike the overlapped Ni 3p and Pt 4f peaks.

[00118] The films were sputter cleaned with Ar^+ (4 kV accelerating voltage) for 20 min prior to starting XPS measurements. A series of spectra collected at different sputtering times showed there was little change in oxygen content for sputtering times beyond 20 min. In one case this was verified by sputtering through the entire film.

[00119] Scanning electron microscopy and energy dispersive x-ray spectroscopy

[00120] Film cross sections were imaged using a FEI Quanta 200 scanning electron microscope (SEM), and a Bruker XFlash 5030 spectrometer was used to measure energy dispersive x-ray (EDX) spectra with a working distance of 10 mm. Analysis of the EDX spectra was done using the ESPRIT version 1.9 software, which corrected for detector effects, applied a Bremsstrahlung background subtraction, and ZAF correction (i.e. correction of atomic number, x-ray absorbance, and x-ray fluorescence effects). Spectra were collected across the samples to assess composition uniformity. Analysis of Ni and Pt content used the L and M lines, respectively. A 10 keV beam energy was used to limit the extent to which the interaction volume extended beyond the film into the substrate. Dimensions in images were measured using ImageJ.58

[00121] Secondary ion mass spectrometry

[00122] Secondary ion mass spectrometry (SIMS) was carried out using a Cameca ims-1280 large-geometry (LG)-SIMS (Cameca Instruments, Inc., 5470 Nobel Dr, Fitchburg, WI, USA) with O_3^- primary ions impacting the sample at 23 keV. A Köhler beam spot (uniform beam density) 50 μm in diameter was used to depth profile the films, with optical gating to accept ions only from the central 19 μm × 19 μm area of the crater. For each measurement the magnetic field was cycled between $^{11}B^+$, $^{30}Si^+$, and $^{62}Ni^+$, counting for 4.96 s, 0.96 s, and 2.00 s, respectively. Wait times of 4.00 s, 2.00 s, and 2.96 s were used to allow the magnetic field to settle before counting. The $^{30}Si^+$ signal was used to determine when the film had been sputtered through. Boron-11 and ^{62}Ni ion signals were scaled by their terrestrial isotopic abundances. A relative

sensitivity factor (RSF) was then used to convert the B^+/Ni^+ signal ratio to a B/Ni atomic ratio. The B/Ni RSF was estimated to be 0.25, based upon a value of 0.211 for NIST SRM® 610 (trace elements in glass) and a reported value of 0.587 for Ni-implanted Si.[59,60] The B/Si RSF was found to be 0.568±0.006 using a sample of Si doped with 1.22×10^{19} ^{11}B atoms/cm^3 (244 µmol/mol), which was traceable to NIST SRM® 2137 (B implanted in Si). This compares well with a value of 0.794 determined for a B implanted Si wafer,[59] and a value of 0.422 for NIST SRM® 610 glass.[60] The B/Ni ratio was then scaled by Ni/(Ni+Pt+O) atomic fractions determined by XPS to yield the B content.

[00123] Profilometry

[00124] Profilometry was carried out using a Zygo Newview 7300 optical profilometer with a 5× Michaelson objective and using 570 nm light. To collect height profiles over a large lateral range, the “stitch” function of the Metropro control software was used to collect overlapping images on a grid over the sample.

[00125] Magnetic measurements

[00126] Magnetic measurements were made using a Superconducting Quantum Interference Device Vibrating Sample Magnetometer (SQUID-VSM, Quantum Design). The electrodeposited films were cleaved to pieces approximately 4 mm by 4 mm, which were then affixed to 5 mm quartz rods with GE 7031 varnish. The samples were cooled to 100 K in zero applied field prior to applying an 8 kA/m (100 Oe) direct current (DC) field. The DC magnetic moment (m) was measured as a function of temperature (T) while increasing the temperature to 400 K in steps of 5 K, and then while decreasing the temperature back to 100 K. These are referred to as zero field cooled (ZFC) and field cooled (FC) measurements, respectively. The moment was also measured as a function of applied magnetic field (H) at 300 K and between ±5.6 MA/m (70 kOe). All magnetic measurements were made at a frequency of 14 Hz and an amplitude of 5 mm for 2 s in an in-plane configuration.

[00127] The raw M vs H and M vs T data had contributions from both the electrodeposited film and the substrate. To remove the diamagnetic contribution, measurements of M vs T and M vs H were made on a bare piece of substrate under the same conditions as were used for measurements on the electrodeposited films.

Volumes used for normalizations were obtained from specimen dimensions measured using calipers (or photographically) and film thicknesses obtained from SEM images. Film magnetizations (M) in units of Am^2/mol were calculated from the measured moment for a sample (m_0, which includes both film and substrate contributions), its area (A_0), the moment of a piece of bare of substrate and its area (m_b and A_b), the electrodeposited film thickness (t), the fcc lattice parameter (a), and Avogadro's number (N_A):

$$\mathrm{M} = \left[\left(\frac{\mathrm{m_0}}{\mathrm{A_0}} - \frac{\mathrm{m_b}}{\mathrm{A_b}}\right)\frac{1}{t}\right]\left[\frac{4}{N_A a^3}\right]^{-1}$$

[00128] Note that the first term is the volume-normalized magnetization and the second term is the inverse of the number density. The factor of four is the number of atoms per unit cell.

[00129] Temperature measurements

[00130] The temperature measurements were taken using internal Cernox thermometers as provided by Quantum Design and installed in the SQUID-VSM system. Temperature accuracy was confirmed with NIST SRM® 766 MnF_2. Error bars were much smaller than the marker.

[00131] The Curie temperature of a sample was taken to be the temperature at which the magnitude of $|dM/dT|$ passed through a maximum for zero field cooled M vs T data. Note that for some samples, a Curie temperature could not be determined, either because the value was outside of the temperature window considered or because the signal to noise ratio was too low.

[00132] The thermosensitivity was calculated in terms of the specific sensitivity S, defined as:

$$S = \left(\frac{\mathrm{T}}{\mathrm{y}}\right)\left(\frac{d\mathrm{y}}{d\mathrm{T}}\right) = \left(\frac{\mathrm{T}}{\mathrm{M}}\right)\left(\frac{d\mathrm{M}}{d\mathrm{T}}\right)$$

where y is a measured parameter, which for the present work is taken to be the magnetization M at a constant 8 kA/m applied field. Note that the specific sensitivity is material specific and unitless, and other measured parameters, such as pressure, capacitance, or resistance may be substituted into the general expression.

[00133] Voltammetry and chronoamperometry

[00134] Voltammograms of ruthenium film electrodes in solutions with and without 0.5 mol/dm^3 $B(OH)_3$ are shown in FIG. 17. For clarity, only the first cycle is shown. The points in FIG. 17 represent the average currents during constant potential depositions. The initial negative going sweep in the voltammograms showed a reduction wave at about -0.32 V. In subsequent negative-going sweeps (FIG. 29) reduction commenced more gradually, but at potentials at least 0.3 V more positive. The more negative potential and sharper increase in current in the first cycle suggest this could be associated with a nucleation process. The nucleation threshold is also supported by the presence of a peak in the current following the initial decay of double layer charging current during the potential steps during which the films were deposited (FIG. 30). Underpotential H_{upd} on the freshly deposited Pt component may contribute to the earlier onset of negative currents on the subsequent voltametric cycles. Similar voltametric behavior was obtained with both gold and ruthenium seed layers.

[00135] As the potential was set to more reducing values, the reduction current increased more rapidly for electrodes in the boric acid-containing solution. The currents for the solutions with and without boric acid diverged at about -0.55 V and -0.65 V for the voltammograms and potential steps, respectively. The coulombic efficiencies of the two series (FIG. 17, inset) diverged in approximately the same potential range to where the currents diverged. Coulombic efficiencies were considerably lower at more reducing potentials in the presence of boric acid.

[00136] To aid in understanding the voltammetry of the fully comprised electrolyte, voltammograms were also measured in the precursor-free supporting electrolyte (i.e., 0.5 mol/dm^3 NaCl + 3 mmol/dm^3 HCl) with and without boric acid using a platinum electrode. A platinum electrode was selected, rather than a ruthenium electrode or an electrodeposited $Pt_{1-x}Ni_x$ film, as the catalytic activity of platinum for hydrogen evolution was more like that of $Pt_{1-x}Ni_x$ than ruthenium. The voltammetry for $Pt_{1-x}Ni_x$ itself was complicated by oxidative dealloying of nickel at more positive potentials. The voltammograms measured at Pt diverged at about -0.55 V on the negative-going sweep; the electrode in the solution without boric acid showed a current plateau in the -0.55 V to -0.8 V range, while the magnitude of the current increased over this entire potential range for the electrode in solution with 0.5 mol/dm^3

$B(OH)_3$. In the former case the current was limited by the mass transport of H_3O^+ down to the -0.8 V lower potential limit, beyond which the current began to increase with the onset of water reduction (not shown). In contrast, in the presence of boric acid a clear rise in the current was evident below -0.55 V associated with protons furnished by dissociation of the pH buffering $B(OH)_3$ and polymeric boron species, with a pK_a value of 8.98 for the former and 7.29 to 6.77 for the later. Note that in this case, rather than the H_2O or OH^- produced by reduction of H_3O^+ or H_2O, $B(OH)_4^-$ and polyborate species would be produced instead.[64,65] For the voltammograms in solutions with the platinum and nickel precursors, the larger currents and lower coulombic efficiencies are related to reduction of boric acid-derived protons or perhaps $B(OH)_3$ stimulated water reduction as suggested by Horkans.[45]

[00137] In the positive-going sweeps of the voltammograms in the precursor-free solutions, there were prominent oxidation peaks at about -0.62 V and -0.39 V, respectively, for the boric acid containing and boric acid free solutions. These are both attributed to hydrogen oxidation. The marked difference in the peak potential reflects differences in interfacial pH. Nucleation of H_2 bubbles also likely affects the voltametric profile in the case of the boric acid containing solution. Depending on the lower potential limit of the voltammogram, one or two oxidation peaks may be observed (FIG. 31).

[00138] For the precursor-containing solutions, the more negative peak in the positive going sweep for the boric acid containing solution may be associated with hydrogen oxidation. For both boric acid-containing and boric acid free solutions, the more positive peak can be attributed to the oxidative dealloying of nickel from the $Pt_{1-x}Ni_x$ film. The smaller nickel stripping peak area for the voltammogram in the boric acid containing solution reflects the lower coulombic efficiency of $Pt_{1-x}Ni_x$ deposition.

[00139] The potential limits for the boric acid free case were selected to avoid nickel hydroxide precipitation. For potentials more negative than about -0.75 V (and at more positive potentials for depositions with larger charge limits) $Ni(OH)_2$ precipitation was evident with a glassy appearance by eye, while a mudcrack-like morphology was observed by SEM ostensibly due to contraction associated with loss of water in the high vacuum environment.

[00140] Film Structure and Composition

[00141] X-ray diffraction patterns for films deposited from solutions without and with 0.5 mol/dm^3 $B(OH)_3$ are shown in FIG. 18, along with a diffraction pattern for the bare ruthenium film. Two additional peaks, fcc (111) and (200) reflections, are observed for the electrodeposited film. The sharp peaks at about 37 nm^{-1} are attributed to the silicon substrate. The ruthenium substrate shows four peaks which are attributed to the (100), (002), (101), and (102) reflections, respectively. At -0.45 V to -0.55 V, the diffraction patterns for the boric acid free and boric acid containing series differ only slightly, but the differences become progressively larger at more reducing potentials. The peaks for the films deposited from the boric acid containing solution become less intense relative to those deposited from boric acid free solution, suggesting these films were thinner. For a given potential, the lattice parameters of films deposited from boric acid-containing solutions were slightly larger. In both cases, most of the lattice parameters are above a line drawn using Vegard's law and the reported lattice parameters for platinum and nickel.

[00142] The platinum nickel phase diagram shows three ordered phases (Ni_3Pt, NiPt, and $NiPt_3$, which have $L1_2$, $L1_0$, and $L1_2$ structures, respectively) with relatively broad composition widths. [9,67,68] Ordered Ni_3Pt and NiPt would be expected to show an ordering peak at about 23 nm^{-1} to 24 nm^{-1}, corresponding to the (110) and (100) peaks of the $L1_2$ and $L1_0$ structures respectively, but no features were observed in this range of the diffraction pattern, indicating the films were disordered fcc (A1) alloys.

[00143] Film compositions were determined by RBS, XPS, and EDX spectroscopy (FIGs. 19-21, 34). A monotonic increase in nickel content as the deposition potential was set to more negative values, was evident, similar to previous reports. For a given deposition potential, differences in composition between films deposited from boric acid-free and boric acid-containing solutions were relatively small. There was good agreement between platinum/nickel ratios determined by the three methods for the most part, though the XPS determined values of Ni/(Ni+Pt) were systematically lower than those determined from EDX spectroscopy.

[00144] To investigate whether the composition of the material deposited changed over the course of the depositions, two additional films with charge limits of 146.5 mC/cm^2 and 586 mC/cm^2 were deposited at -0.65 V from the boric acid containing solution (half and double the charge limits used for the other films in the present work). RBS characterization of these three films (FIG. 3) indicated a decrease in the fraction of nickel in the film (Ni/(Ni+Pt)) with increasing charge passed. The 146.5 mC/cm^2, 293 mC/cm^2, and 586 mC/cm^2 films were 76.9%, 78.4%, and 79.3% nickel, respectively. EDX measurements on the same three samples showed variations on a similar scale, but the nickel content decreased with charge passed rather than increased (81.5% to 78.3% nickel). While the two techniques showed different trends, the variation for each is likely within the error of the measurement, and indicate the nickel fraction varied weakly, if at all, with the amount of charge passed. Eiler et al. had observed the film platinum content to decrease with deposition time,[29] though the depositions considered in that comparison were shorter than those considered here, which could mask the effect in the present case.

[00145] EDX spectroscopic mapping indicated the platinum content tended to decrease going from the region of the film that was deepest in solution during the deposition to the region that was shallowest, reflecting the impact of free convection. The amount of variation within a given film was generally smaller than the difference in composition between two samples deposited at potentials 50 mV apart (FIG. 33).

[00146] EDX spectroscopy, RBS, and XPS all indicated the presence of oxygen in the films. With EDX, the interaction volume extended into the silicon thermal oxide layer underlying the films, and the response thus had contributions from both the film and the SiO_2 layer of the substrate. The oxygen signal for EDX spectra of films electrodeposited on oxygen free high conductivity copper foil substrates was above the background level, indicating the presence of some oxygen in the films. In RBS, oxygen in the electrodeposited $Pt_{1-x}Ni_x$ layer was in some cases apparent as broad peak at about 0.7 MeV overlying the feature associated with silicon, and slightly higher in energy than the peak associated with oxygen in SiO_2. In other cases, oxygen in the electrodeposited $Pt_{1-x}Ni_x$ layer was apparent only as a diminution of the platinum and nickel signals in RBS. In fitting the RBS data, a correlation between the parameters representing the $Pt_{1-x}Ni_x$ layer thickness and its oxygen content was noted,

and this possibly skewed the fitted oxygen contents to higher-than-expected values (FIG. 28).

[00147] XPS is reliable for the determination of oxygen. It showed a considerable amount of oxygen prior to sputter cleaning of the films due to the surface oxide formed due to exposure to the atmosphere. Oxygen was still present in the spectra following extended Ar sputtering with the films deposited from boric acid containing solution always having higher oxygen levels. The oxygen content of the films deposited from boric acid free solution was relatively invariant with deposition potential, while for boric acid solution the film oxygen content increased as the deposition potential was stepped to values more negative than -0.55 V. The disparity between the two series of films is readily apparent in FIG. 20B. While the XPS spectra presented here show only a monotonic increase in oxygen content with decreasing deposition potential, preliminary EDX characterization of $Pt_{1-x}Ni_x$ films on low oxygen copper foil substrates suggest there might be a maximum in the oxygen content at more reducing potentials. Further work is needed for confirmation. The O (1s) spectra comprised three peaks, suggesting the oxygen resided in at least three chemical environments. Of the three, the peak at the lowest bonding energy (about 530 eV) showed the greatest difference between boric acid free and boric acid containing solution. This peak may correspond to oxygen in an oxide while the remaining components may involve interactions with H such as in hydroxides. These species are most likely distributed as grain boundary segregants although the possibility occupation of interstitial sites within the fcc lattice cannot be excluded.

[00148] Another possibility is that some of the oxygen is associated with borate. The 1s binding energy of boron in the oxidized form would be expected near 193 eV,[69] however no signal above background was evident in high resolution scans in the 180 eV to 200 eV range. More sensitive analysis with secondary ion mass spectrometry revealed boron was present in films deposited from boric acid containing solutions. The detected quantity was more than three orders of magnitude larger than that observed for a film deposited from boric acid free solution, indicating the boron incorporated in from boric acid containing solution was not adventitious. A film deposited in the absence of boric acid at +0.65 V, the boron content was 53±16 nmol/mol, while that for a film deposited at the same potential in the presence of boric

acid was 383±12 μmol/mol. The deposition potential affected the amount of boron incorporated little; films deposited at +0.60 V and +0.55 V from boric acid containing solution had 411±11 μmol/mol and 281±15 μmol/mol, respectively. Note that the uncertainties noted for these boron contents reflects the precision of the measurements, and not the absolute accuracy of the concentration values. The relative amounts in these films are well known, but the absolute concentration might be as much as a factor of 3 different from the actual value due to the dissimilarity between the standards and the samples.

[00149] Film Quantification

[00150] While the charge passed per unit area during deposition was a specified quantity, the coulombic efficiency and deposit thickness, and thickness uniformity needed to be measured. Several approaches were taken towards quantifying the amount of material in the electrodeposited films. Measurements performed to determine the electrodeposited film thicknesses included x-ray reflectivity, optical and profilometry, energy dispersive x-ray spectroscopy, cross sectional SEM and helium ion microscope (HeIM) imaging, and RBS. Film thicknesses determined by RBS and SEM plotted against deposition potential are shown in FIG. 22a. Because a charge limit was placed on the depositions, a lower coulombic efficiency results in a thinner deposit. Thus, the films deposited at more reducing in the presence of boric acid were thinner than those deposited in its absence (cf. FIG. 17a inset).

[00151] It was possible to measure the thickness of the sputtered ruthenium with XRR, but the overlying electrodeposited films were too rough for this approach. The ruthenium thickness and surface roughness fit to values of 43.2 nm and 0.95 nm, respectively. The fitted ruthenium scattering length density indicated a mass density about 95% of the reported value of 12.438 g/cm^3, and x-ray diffraction of the film indicated a density nearly equal to the literature value. (The slight discrepancy could be due to alignment error in either the XRD or XRR measurements.) Four-point probe sheet resistivity measurements at room temperature gave values of about 10 μΩ cm, which is somewhat higher than that reported for bulk ruthenium, though the thinness of the film and limited grain size could increase the value due to surface and grain boundary scattering. The XRR, XRD, and resistivity measurements indicate relatively

low oxygen content in the ruthenium film. The (002) peak was the most intense in the ruthenium diffraction pattern (and the most intense by far when the measurement was carried out in a symmetric θ/2θ configuration), indicating strong texture along the *c* direction.

[00152] Film thicknesses were quantified by SEM imaging of cleaved midline cross sections of the films. Significantly, the analysis also yielded a ruthenium layer thickness which agreed well with the value determined by XRR. The microscope magnification calibration was also checked against a lithographically-defined trenched patterned substrate (Quick Cleave D, Semitech/ATDF, Austin, TX). The chief source of uncertainty in these measurements was likely in determining the locations of layer boundaries within an image. Several locations were imaged along the cross-section of each film to minimize sampling error. A set of cross-sectional thicknesses measured along the edge of a film is shown in FIG. 22b, along with a representative image included in the inset. The $Pt_{1-x}Ni_x$, Ru, and SiO_2 layers can be distinguished in this by their distinct morphologies in this image, as well as in an HeIM image included in FIG. 35.

[00153] Optical profilometry was used to measure the edge height of some of the films, but substrate warp at least in part due to substantial growth stress[54] was generally much larger than the film thickness. Assessment of edge height was further complicated by several features, including gas bubbles that tended to grow at the periphery of the electrode during deposition and screened further metal deposition, and irregularities in the cut edge of the tape mask used to define the electrode area. These features made the edge profile more complicated than a simple step function (FIG. 22c). The edge height around the perimeter of an electrode is compared with thicknesses determined by SEM cross sectional imaging in FIG. 22b. There is rough agreement in the general trends determined by the two methods, but the SEM results are considered more reliable due to the factors complicating analysis of the profilometry data.

[00154] EDX spectroscopy can also be used to measure thin film thicknesses. A complete quantitative analysis was not performed but the EDX results qualitatively confirm the thickness trends determined by imaging the film cross sections, i.e. films deposited at more reducing potentials are thinner in the presence

of boric acid. This was evident in the intensity of x-rays from the underlying Ru/Ti/SiO_2/Si substrate, which were attenuated by the overlying $Pt_{1-x}Ni_x$ film which decreases the fraction of the beam reaching the buried layers with sufficient energy and attenuates the resulting x-rays. Spatially resolved EDX spectra, and a plot of the substrate attenuation vs deposition potential are included in the supporting information (FIG. 32, 33).

[00155] As noted earlier, the deposits were generally thicker at the end of the electrode that was deeper in solution during deposition. This is evident in the SEM cross section values, profilometry step edge heights in FIG. 22b and c, and substrate x-ray attenuation in EDX spectroscopy in FIG. 33. Depletion of the precursors at the electrode surface during deposition is expected to decrease the solution density in the diffusion layer. The density difference between the diffusion layer and bulk solution produced upward convection leading to an increase in the depletion layer thickness going from the bottom to the top of the electrode.[70,71] This convection is also reflected in the small gradient in the platinum/nickel ratio from the bottom to top of the specimen midline. (FIG. 32c)

[00156] The film thickness was also determined from analysis of the Rutherford backscattering spectrometry. The $^4He^{2+}$ ion beam was about 2 mm across, so these measurements give a more area-averaged result than the aforementioned methods. Analysis of RBS data yields an area specific number density for different nuclei in different layers, which can be converted to a thickness if the volumetric number density is known. Volume specific number densities were determined from XRD, assuming an fcc structure. The vacancy content of the films is unknown, but was assumed to be negligible for this analysis.

[00157] In modelling and fitting the RBS data, it was found that there was a positive linear correlation between the fitted oxygen content of the films and the area specific number density. Initial results yielded oxygen contents and thicknesses that were greater than those expected from XPS and SEM, respectively. It was found, however, that there were other local minima, albeit with somewhat higher χ^2 values, that were more consistent with the results of the other characterization methods. These more consistent fits were selected in preference to those which produced the lowest χ^2 values. The fitted platinum/nickel ratios were generally consistent across

the different fits of a given data set and close to the values determined by XPS and EDX.

[00158] Magnetic Characterization

[00159] The magnetic responses of two series of $Pt_{1-x}Ni_x$ films, one deposited from boric acid-free and one from boric acid-containing solutions at different applied potentials, were measured as a function of applied field at a constant temperature of 300 K, and as a function of temperature at a constant applied field of 8 kA/m (100 Oe) are shown in FIG. 23 and 24, respectively. Both the M vs H and M vs T responses of films deposited in the -0.75 V to -0.50 V range indicated they were ferromagnetic.

[00160] The magnetization in M vs H measurements for films deposited from boric acid-free solution increased almost monotonically as the deposition potential was set to more reducing potentials, concomitant with increasing nickel content (FIG. 23). For films deposited from boric acid-containing solution, however, the magnetization showed a more muted deposition potential dependence. It should be noted that the M vs H response of the films often had a non-zero slope at the maximum applied field. This may have been due to a paramagnetic contribution, possibly indicating the presence of platinum rich regions within the samples or oxidation. Accordingly, for these samples, it was not possible to assess the saturation magnetization. Instead, magnetization at 5.6 MA/m (70 kOe) was taken as a metric for comparison. In some cases, this value was the same as the maximum magnetization. The films were magnetically soft, with coercivities less than the flux trappage of the superconducting magnet (approximately 2.8 kA/m or 35 Oe), with the exception those deposited at -0.70 V and -0.75 V from a boric acid-free solution, with coercivities of about 7.5 kA/m (95 Oe) and 10.9 kA/m (140 Oe), respectively.

[00161] The field cooled M vs T response of films deposited from boric acid-free and boric acid-containing solutions both showed an increase in the Curie temperature for progressively more reducing deposition potentials, along with increasing nickel content (FIG. 24a and 24b). For simplicity of presentation and interpretation, only the field cooled measurement is shown. Similar to the M vs H measurements, the magnitude for the M vs T response increased almost monotonically for progressively more negative deposition potentials, but again showed

a weaker deposition potential dependence for the films deposited from boric acid-containing solution. Note that while the M vs T responses of films deposited at -0.70 V and -0.75 V from boric acid-free solutions were also characterized, the Curie temperature for these films were above 400 K.

[00162] All films with a Curie temperature within the measurement range had a narrow temperature range of high magnetic thermosensitivity *S* (FIG. 24c and 24d) around T_C and a broad shoulder extending towards lower temperatures. Calculation of *S* had the effect of accentuating noise in the data, particularly where dM/dT or M was small. Thus, the data have been truncated to a range where the magnetization was between 8% and 90% of the maximum magnetization attained in each M vs T measurement for the calculation of S.

[00163] The magnetic behavior of a series of electrodeposited $Pt_{1-x}Ni_x$ films was evaluated. A monotonic relationship between the deposition potential and film composition and lattice parameter was found. Comparison with materials produced by electrodeposition and other means, including sputter deposition, thermomechanical processing, chemical vapor deposition, pulsed laser deposition, thermal decomposition and an aerosol-based method leads to reasonable agreement as shown in FIG. 25. The origins of the positive and negative deviations from Vegard's law remain to be understood, but the dispersion may be indicative of the measurement challenge as was previous noted during the characterization of sputter deposited films. Error in both the composition measurements and lattice parameter measurements could contribute.

[00164] An important aspect to be considered is the incorporation of light elements, i.e. O, B, and H, into the films. In the present work O levels from 1 to 4 atomic % were measured and found to result from the presence of boric acid. Further still, as the Ni-rich $Pt_{1-x}Ni_x$ films are deposited at potentials negative of the H_3O^+/H_2 reversible potential, H is likely to be incorporated in the film although no measurements of its concentration and its dependence on processing conditions are available at present. It is unclear how much and for how long the hydrogen would remain in the film after it is no longer poised at reducing potentials.

[00165] Film Oxygen and Boron Content

[00166] The presence of boric acid is known to hinder precipitation of nickel hydroxide species at more negative potentials, however the present work demonstrates that this occurs at expense of lower current efficiency and unexpectedly higher oxygen content in the deposit. Reduction of boric acid-derived protons would be expected to prevent the interfacial pH from increasing as much at a given potential as it would if H_3O^+ and H_2O were the only available reducible protons. The expectation would thus be for greater nickel hydroxide precipitation for the boric acid free case, and thus that less oxygen would be incorporated in the presence of boric acid. This has been shown to be the case for deposition of Ni alone.[74] Note that for films deposited from boric acid free solution at more reducing potentials on a low oxygen copper foil substrate where the presence of nickel hydroxide species in the deposit was apparent from the cracked deposit morphology, the EDX indicated a much higher oxygen content than films deposited in the presence of $B(OH)_3$. This suggests the nature of the oxygen incorporation is different.

[00167] While incorporation of oxygen associated with boron is another possible explanation, particularly since adsorption of boron containing species from boric acid and borate containing solution has been reported, no boron 1s signal was observed above background in the XPS data. If the excess O (1s) signal in the spectra for films deposited from boric acid containing solution were attributed to borate species, given the Kratos relative sensitivity factors for B (1s) and O (1s), 0.159 and 0.78, respectively, the boron signal accompanying the oxygen signal would be a factor of 14 lower. Given the noise level in the region of the spectrum where boron was expected, it would not have been readily detectable.

[00168] The SIMS result is only semiquantitative due to the dissimilarity of the matrix effects of boron doped silicon standard relative to $Pt_{1-x}Ni_x$. Nevertheless, analysis based on the $^{11}B^+/^{62}Ni^+$ ratio indicated boron was present in considerably smaller quantities than amounts of oxygen measured by XPS. The amount of boron in the film deposited from boric acid containing solution at -0.65 V had about 4% oxygen and about 0.038% boron (383±12 μmol/mol), a factor of about 100. Excess oxygen in the films deposited from $B(OH)_3$ containing solution was thus at most partially associated with boron. If the oxygen in the films was not associated with boron, it would seem likely that it is bound to nickel in the films. The peak positions in

the XPS spectrum of the Pt 4f and Ni 3p core level spectra showed little variation between films deposited with and without boric acid, and also little variation with the deposition potential, and hence with nickel content, which is consistent with previously reported XPS characterization of bulk alloys produced at high temperature. (FIG. 34) The invariance of the peak positions would not indicate greater oxidation, though it is possible subtle changes elsewhere in the spectra could be associated with oxidized nickel species.

[00169] Film Magnetic Behavior

[00170] While the nickel-rich films deposited from the boric acid containing solution at more reducing potentials were thinner than those deposited from the boric acid free solution at the same potential, the normalization of the magnetic moment to determine the magnetization takes this into account. This means that the films deposited from boric acid containing solution had a smaller magnetic responses per unit of material present. While the reason for this is not entirely clear, it could be due to the higher oxygen content of the films deposited from boric acid containing-solution. Oxygen incorporation has previously been noted for electrodeposited $Pt_{1-x}Fe_x$[39,40,75] and its presence was found to decrease the magnetization of the material,[40,75] and it was concluded the magnetization was lower because the iron was oxidized.

[00171] It is also possible local structure could play a role in the lower magnetization of films deposited from boric acid containing solution. Formation of $L1_2$ ordered $Pt_{1-x}Ni_x$ has been reported to decrease the magnetization at a given composition. Though XRD indicated the films were fcc alloys (i.e. not ordered phases), the possibility of some clustering within the bulk cannot be discounted. Previous studies have indicated that local structure plays a role in the magnetic behavior of $Pt_{1-x}Ni_x$, with the moment of each nickel atom depending upon its chemical environment and most strongly on its nearest neighbors. This is a general feature of the magnetic behavior of transition metal alloys.

[00172] Strain could also play a role in the differing magnetic behaviors between the boric acid free and boric acid containing series. The lattice parameters were generally slightly smaller for films deposited from boric acid free solutions, suggesting strain could play a role, although the differences in electronic structure this

produces are too subtle to discern in the valence band energy range of XPS measurements presented here.

[00173] The magnetizations of the films at the maximum applied field of 5.6 MA/m for a given composition were considerably lower than previously reported saturation values reported for $Pt_{1-x}Ni_x$ produced at high temperature, but were closer to values reported for electrodeposited and evaporated samples (FIG. 36). One point to note is that some reported measurements were conducted at low temperature, and the increased thermal energy available for disordering spins in measurements reported here (at 300 K) will decrease the magnetization. Also, as noted earlier, the magnetic response did not saturate at the maximum applied field, which by definition means the response was smaller than saturation. While not conclusive, it seems possible that the higher oxygen content of the films deposited from boric acid containing solution could be a contributing factor in diminishing their magnetizations relative to the literature values. Though speculative, hydrogen, present either as a hydride or bound to oxygen, could also play a role. Electrochemical hydrogenation of nickel has been reported to decrease its magnetization. Hydrogen is ostensibly present in the bulk during deposition, though further experimental work is needed to verify whether an appreciable amount remains after removal from the deposition environment.

[00174] Curie temperatures measured for a given composition in the present work were systematically lower than those recently reported by Eiler et al. for electrodeposited $Pt_{1-x}Ni_x$ films (FIG. 36). This may in part be due to a difference in the measurement conditions (80 kA/m or 1000 Oe) which was nearly at saturation, rather than the 8 kA/m field used in the present work), the way the data were processed (the two tangent method, as opposed to the inflection point used here), or due to the nature of the samples themselves (the reported values were for mesoporous $Pt_{1-x}Ni_x$ films). Reported T_C values for $Pt_{1-x}Ni_x$ prepared by sputter deposition and high temperature methods were comparable to the values for electrodeposited films in the present work (FIG. 26). Lower T_C values have been reported for annealed relative to quenched $Pt_{1-x}Ni_x$, which is due to formation of the $L1_2$ ordered structure in the annealed case. The T_C values for films deposited from $B(OH)_3$ containing solution were lower than for films deposited from $B(OH)_3$ free solution, and tended to be closer to literature values for

annealed samples in the same composition range, but the XRD data indicate this was not due to long range order. Differences in local structure in the two series could be contributing factor to the differences in T_C, but differences in light atom content and strain may are also possible contributing factors.

[00175] AN investigation of the effect of film thickness on magnetic response was made. The Curie temperatures of three films deposited at -0.65 V with thicknesses of 30 nm, 60 nm, and 116 nm were 314 K, 356 K, and 381 K, respectively (FIG. 37).

[00176] Magnetic Thermosensitivity

[00177] As expected given how T_C was defined herein, $Pt_{1-x}Ni_x$ films showed the largest thermosensitivity *S* near T_C. For comparison, the well-known industrial thermometer made from platinum wire or films is the PRT (platinum resistance thermometer), sometimes designated as 'PT100', has a thermosensitivity of approximately 1. This is ideal for an interpolation thermometer operating over a wide range of temperatures. Other more sensitive devices, such as metal oxide based thermistors, with $S > 1$ may also be used for thermometry, but usually over a more restricted range of temperatures. Data corresponding to these two such devices are included in FIG. 24 for comparison.

[00178] $Pt_{1-x}Ni_x$ could potentially be used as the basis for interpolating thermometers of high thermosensitivity, but over temperature windows of about 25 K centered on T_C. While it may have less general utility than the PRT, it could potentially be used for applications within a narrow temperature range, such as found in many biomedical research applications. Importantly, the tunability of the thermosensitivity with deposition potential means the material can be tailored for the temperature range of interest.

EXAMPLE 2

[00179] Thermosensitivity Through Exchange Coupling in Ferrimagnetic/Antiferromagnetic Nano-Objects for Spatially Resolved Thermometry

[00180] Measurement of temperature is critical to every scientific discipline. As technology advances, thermometry with spatial resolution becomes crucial to fully develop application, in the areas of biomedicine, integrated photonic devices, fuel cells, combustion engines, microelectronics, and additive manufacturing, to name a few. Remote thermometry within an optically opaque 3D volume with microscale resolution is generally not possible. Thermal magnetic particle imaging (T-MPI)[a], which is based on the non-linear magnetic response of magnetic nano-objects (MNOs), is currently at the forefront of possible solutions. However, T-MPI requires MNOs that exhibit strong temperature dependent magnetization (thermosensitivity) near room temperature (200 K to 400 K). Commercially produced colloidal nanoparticles typically show minimal change in magnetization with temperature in this temperature range. Here, we focus on development of MNOs with good thermosensitivity around room temperature.

[00181] Core-shell and bi-magnetic nano-objects of F(i)M and AFM materials have been previously studied due to their potential to exhibit exchange bias (EB). EB is an interfacial coupling effect between the F(i)M and AFM, which can lead to changes in the coercivity of the MNOs. These effects have been studied in Co/CoO formed by controlled oxidation; $Fe_{3-d}O_4$/CoO and $CoFe_2O_3$/CoO produced by seed-mediated growth; and FeO/Fe_3O_4, MnO/Mn_3O_4, CoO/Fe_3O_4, CoO/$CoFe_2O_4$, CoO/$Co_{1-x}Zn_xFe_2O_4$, and $Co_yFe_{1-y}O$/$Co_xFe_{3-x}O_4$ synthesized by a variety of colloidal methodologies. Despite some fundamental studies on these materials, no new technologies have emerged for utilizing this type of exchanging coupling in MNOs. Recent computational work has suggested that in core-shell nanoparticles of ferromagnetic iron and gadolinium with antiferromagnetic interfacial exchange coupling, a sharp change in the magnetization with temperature can occur.[i1] This temperature feature shows tunability, with the core radius and core/shell thickness ratio as independent parameters.

[00182] We synthesized ferrite/CoO MNOs by a seed-mediated colloidal growth approach. The FiM/AFM MNOs were physically characterized by X-ray diffraction (XRD), dynamic light scattering (DLS), Raman spectroscopy, and (scanning) transmission electron microscopy (STEM/TEM). The magnetic and thermal properties of the MNOs were characterized by DC and AC magnetometry

measurements as a function of temperature plus room temperature magnetic particle spectroscopy (MPS). The results show proof of concept of induced thermosensitivity through interface effects.

[00183] Structural Characterization

[00184] The MNOs produced in this work were synthesized by a seed-mediated colloidal growth approach. Ferrite particles were first synthesized and used as seeds to grow the antiferromagnetic CoO in a second synthesis step. Details are given in the material synthesis and characterization methods section. Crystal structures and qualitative phase quantities were evaluated by powder XRD, shown in Figure 1. The ferrite MNOs were indexed to the inverse spinel structure and the CoO MNOs were indexed to the cubic rock salt structure. All ferrite/CoO nano-object samples show both the inverse spinel and cubic rock salt structures, but the relative peak intensity differs according to the synthesis conditions. One sample (with 48 mg ferrite seeds) has a majority inverse spinel ferrite phase and is labeled as nanoflowers. The other (with 32 mg ferrite seeds) has a majority of CoO cubic rock salt phase and is labeled as clusters. Table S1 summarizes synthesis details including the morphology and corresponding quantity of ferrite seeds, DLS size and TEM size when available.

[00185] The size, morphology, and interface between the crystal structures was investigated by transmission electron microscopy (TEM). Figure 2 (a) is a TEM image of the ferrite particles with corresponding size distributions from TEM and DLS. The mean size determined from TEM is approximately 10 nm with a standard deviation of 2 nm. The mean hydrodynamic size is approximately 12 nm (main peak). The nanoflower sample with majority ferrite phase is composed of irregular shaped particle-like objects with an approximate mean cross section of 13 nm and standard deviation of 3 nm, Figure 2 (b). The mean hydrodynamic size from DLS was found to be approximately 22 nm. The discrepancy between the TEM size and DLS size is most likely due to a combination of the organic surfactants on the surface, and the non-spherical nature of the nanoflowers leading to additional errors in size estimation by DLS. The cluster sample with majority of CoO phase shows tightly packed polycrystalline objects, Figure 2 (c). In this case the mean hydrodynamic size was

found to be approximately 74 nm, suggesting that these objects remain intact when dispersed in hexanes.

[00186] The next step is to examine the interface between the ferrite and CoO, using high resolution (HR)-TEM. Figure 2 (d) shows HR-TEM of a single ferrite particle. The d-spacing of this particle was determined by averaging across the line indicated by arrows and was found to be approximately 0.254 nm corresponding to the (311) plane of the inverse spinel structure, a similar value of 0.252 nm was determined from XRD. In Figure 2 (e) the nanoflower sample is shown, which has clear crystalline interfaces between the ferrite center with (311) plane, and the cubic rock salt CoO phase identified by the (111) plane. In this case it appears as if the CoO forms an interface with the ferrite and grows from the faceted sides of the particle. The cluster sample shows a similar ferrite center with CoO growing from the surface of the particle creating a crystalline interface between the two phases, Figure 2 (f).

[00187] To further elucidate what is occurring at the interface after the growth of CoO on the ferrite particles, high-angle annular dark-field (HAADF) scanning transmission electron microscopy (STEM) imaging, energy dispersive X-ray spectroscopy (EDX) elemental maps, and Raman spectroscopy were performed. Figure 3 shows STEM images and corresponding elemental maps of representative morphologies in the ferrite/CoO nanoflower sample. In Figure 4 (a), cobalt-rich protuberances are shown growing from the iron-rich ferrite center. This image closely matches the particle shown in the HR-TEM, Figure 2 (e), with these cobalt regions being identified as the cubic rock salt structure of CoO and the iron-rich region having the inverse spinel structure. Figure 3 (b) shows a more spherical particle which has a cobalt-rich surface with similar iron-rich core. At the interface there appears to be diffusion between the cobalt and iron rich regions. Line scans of these particles, Figure S1, reveal a relatively uniform signal of cobalt coming from the iron rich cores with the largest protuberance in the irregular particle and the surface of the more spherical particle being nearly all cobalt. An additional STEM map of another particle from the nanoflower sample is shown in Figure S2, with similar features. The STEM results suggest cobalt may diffuse into the ferrite particles followed by growth of the CoO phase. Alternatively, the cobalt signal coming from the iron rich regions may simply reside on the surface of the particles.

[00188] Raman spectroscopy, Figure 4, was used to identify structural features not detectable by XRD. Figure 4 shows Raman spectrum of representative ferrite particles, nanoflowers, clusters, and CoO. The ferrite particles have two primary modes at 663 cm^{-1} and 698 cm^{-1}. These can be identified as the A_{1g} modes of magnetite and maghemite, the values are in relatively good agreement with what has been reported in iron oxide thin films[1j], and a previous work including both computational and experimental data.[2j] The highest intensity mode in the CoO spectrum is at 529 cm^{-1}. Previous reports on single crystal samples[3j,4j] have identified a one-phonon longitudinal optical (LO) mode in the range of 540 cm^{-1} to 560 cm^{-1}, but in a nanocrystalline sample with cubic rock salt structure[5j] a value of 530 cm^{-1} has been reported for this mode, in agreement with our findings.

[00189] In the nanoflower sample two primary peaks can be identified at 667 cm^{-1} and 534 cm^{-1}; in the clusters, these peaks are found at 666 cm^{-1} and 537 cm^{-1}. The peaks at 666 cm^{-1} and 667 cm^{-1} are the highest intensity mode of the ferrite and the peaks at 534 cm^{-1} and 537 cm^{-1} are that of the CoO. Comparing these spectrums to the spectrum of ferrite particles, the most striking feature is the clear disappearance of the maghemite shoulder on the A_{1g} peak. Additionally, the mode at 369 cm^{-1} is no longer present which also belongs to the maghemite phase. Maghemite is typically believed to exist on the surface of ferrite particles in a magnetite-maghemite core-shell configuration[1,2], and the disappearance of these peaks after the growth of CoO strongly support Co diffusion into the surface of the ferrite particles leading to the formation of a Co ferrite phase. Therefore, the shifts in these peaks may be related to diffusion at the interface leading to the formation of a lightly doped Co ferrite phase.

[00190] At lower wavenumbers two additional modes are observed in the nanoflowers; 302 cm^{-1} and 461 cm^{-1}, and in the clusters; 300 cm^{-1} and 460 cm^{-1}. These modes are similar to those reported in Co ferrites.[6j,7j] The mode at 460 cm^{-1} and 461 cm^{-1} is the most distinct to the Co ferrite phase, and it can be observed that all four spectrum clearly have modes in the range of 300 cm^{-1} to 307 cm^{-1}. Comparing the 460 cm^{-1}/461 cm^{-1} modes to the CoO spectrum there is a similar shoulder on the main mode of CoO, however, fitting of the spectrum produced a value of 447 cm^{-1}. To ensure this value was outside of experimental uncertainties three measurements were performed on the nanoflower sample yielding a mean and standard deviation of this

mode to be 466 cm^{-1} ± 5 cm^{-1}, suggesting this is a different mode not coming from the CoO phase. Lastly, comparing to the ferrite spectrum, a mode is identified at 465 cm^{-1}, however, the fit is poor due to the low intensity, and this most closely matches the E_g mode of maghemite.[1j] Since we have already concluded that the maghemite phase is no longer present in the nanoflowers and clusters, the mode at 460 cm^{-1}/461 cm^{-1} gives further support to the formation of a Co ferrite phase. Fittings of the Raman spectrum are presented in the supplemental information Figure S3.

[00191] Based on the Raman spectrum and STEM elemental mapping the following model is proposed, Co diffuses into the surface layer of the ferrite particles followed by growth of the CoO phase, leaving nano-objects with three distinct phases: CoO, a Co doped ferrite region/layer, and a magnetite core. The Raman spectrum support the formation of a lightly doped Co ferrite due to the disappearance of the maghemite modes and presence of a low intensity mode at 460 cm^{-1}/461 cm^{-1}. STEM mapping shows the core remains iron rich, we can conclude that the center of the particles is most likely still magnetite.

[00192] Magnetic Characterization

[00193] Zero-field cooled (ZFC) temperature dependent magnetization measurements and temperature dependent AC susceptibility (ACS) were used to investigate the thermosensivity of the MNOs. The ZFC measurements of liquid samples (hexanes) of the nanoflowers and clusters are shown in Figure 5 (a). The samples have approximate concentration of 10 mg solids/mL and are normalized by the total mass of the samples, solid material and solvent. The magnetization of the clusters increases with increasing temperature in the range of 200 K and 285 K. In contrast, the nanoflower sample shows an entirely different behavior, with a sharp increase in magnetization between 200 K and 220 K, and a decreasing trend from 220 K to 310 K. Due to a difference in concentration of the liquid samples the relative change in magnetization with temperature for the clusters and nanoflower samples was compared to the ferrites by normalizing by the maximum magnetization in the 200 K to 310 K temperature range, Figure 5 (b). The bare ferrite particles show a nearly linear drop in magnetization between 200 K and 310 K, compared to the sharper rise in magnetization over nearly the entire range for the clusters, and sharp change in magnetization at the low end of this range for the nanoflowers. The ZFC and field-

cooled (FC) measurements normalized by total sample mass of the ferrite particles, nanoflowers and clusters are shown in Figure S4. Additional magnetic measurements of samples with Ni doping are shown in Figure S5. These samples have similar temperature dependent magnetization behavior as the clusters.

[00194] To probe the exchange interactions between the FiM ferrite and AFM CoO, an exchange bias measurement was performed on the liquid samples. The samples were field cooled in 1 Tesla to 100 K, below the freezing point of hexane, to immobilize the MNOs from physical rotation, after which a 7 Tesla hysteresis loop was performed, Figure 5 (c). The nanoflowers show a square hysteresis loop, with an exchange bias field of approximately 50 mT. It is likely that the particles form chains during the field cooling causing a cascading magnetic reversal resulting in the loop squareness. Alternatively, the clusters show a more rounded hysteresis suggesting less uniformity in the magnetic reversal. The clusters have an approximate exchange bias field of 643 mT. The difference in exchange bias is most likely related to the uniformity of coverage and thickness of the antiferromagnetic CoO.[b2] The highest exchange bias is measured for the sample with largest amount of CoO phase. The saturation magnetization is higher in the nanoflowers since it is majority ferrite phase compared to the clusters which are majority CoO phase, Figure 5 (c,d).

[00195] To further investigate the temperature dependent behavior of the nanoflowers ACS measurements were performed between 200 K and 310 K. At 200 K there is a sharp decrease in the ACS signal in the low frequency range suggesting energy is not entering the system, Figure 6 (a). At 210 K there is an increase followed by a steady decrease with increasing frequency and between 220 K and 300 K the ACS signal is nearly flat suggesting a balance of energy in the system. Since the magnetocrystalline anisotropy is likely not changing significantly over the range of 200 K to 220 K, we believe the change in the ACS signal is related to a change in the exchange bias field between the ferrite and CoO. Figure 6 (b) shows the ACS at 1 kHz as a function of temperature along with the DC ZFC measurement of the nanoflowers. The same trend is observed between the ACS and DC ZFC, and we believe the sharp change in magnetization and the susceptibility is related to a reduction of exchange bias field due to passing through the Néel temperature of the CoO.

[00196] Room temperature liquid (hexanes) magnetic particle spectroscopy (MPS) measurements were performed to test the AC magnetic response of the MNOs under more realistic AC field conditions that will be used for T-MPI. Most notability the AC drive field amplitudes are typically much higher than what is used in ACS. Figure 7 shows the MPS measurements at a frequency of 1 kHz with approximately 14 mT, Figure 7 (a), and 21 mT, Figure 7 (b), drive field peak amplitudes. The samples were normalized by the total mass of solid material in kilograms. At 14 mT the MPS intensity seems to be proportional to the amount of ferrite in the nano-objects with the nanoflower sample having a higher signal than the clusters. At the higher drive field peak amplitude of 21 mT the MPS intensity of the nanoflower sample is comparable to that of the bare ferrite. With a drive field peak amplitude of 14 mT the nanoflower MPS intensity was determined to be about 73% of the ferrite particles, and at 21 mT the signal increased to about 93% of the ferrite particles MPS intensity. The fast Fourier transform of the 21 mT, 1 kHz data is shown in Figure S6. Additionally, MPS measurements were performed at 7 kHz with a 14 mT drive field peak amplitude, Figure S7, which shows an increase in the overall signal with improved signal to noise.

[00197] Thermosensitivity of MNOs

[00198] The thermosensitivity is a change in magnetization with temperature, but this needs to be defined to compare materials. Using the definition from thermometry[1k,2k], but replacing the changing property of resistance with magnetization, we get the following:

$$S_M = \left|\left(\frac{T}{M(T)}\right)\left(\frac{dM(T)}{dT}\right)\right| \quad (1)$$

where M is magnetization and T is temperature. However, it is important to note that the thermosensitivity is only one parameter that will affect the performance of a material for T-MPI.

[00199] Using equation 1, thermosensitivity curves as a function of temperature are calculated from the liquid DC ZFC measurements, shown in Figure 9. The thermosensitivity of the ferrite particles is nearly constant, being close to approximately 1 over the measured range. In contrast the thermosensitivity is greatly enhanced in some ranges of temperature in the FiM/AFM nano-objects. The nanoflowers show a large thermosensitivity of greater than 10 at 200 K, which rapidly

decrease to be in line with the ferrite particles at higher temperatures. In the clusters the mean thermosensitivity is approximately 6 between 200 K and 260 K decreasing to about 1 at 275 K. The results show that thermosensitivity can be induced by interface effects and can be greatly affected by sample morphology (particle-like nanoflowers vs. clusters) in liquid samples.

[00200] Material Synthesis and Characterization Methods

[00201] Synthesis of Ferrites Particles. The ferrites were synthesized by thermal decomposition of iron (III) acetylacetonate, $Fe(acac)_3$, in a mixture of 9 mL oleylamine (70 %) and 1 mL oleic acid.[1l] The $Fe(acac)_3$ was combined with the organic compounds at room temperature with a magnetic stir bar and put under vacuum followed by the addition of an Ar blanket. Under continuous Ar flow and stirring at 700 RPM the mixture was heated to approximately 383 K (set point) for 30 minutes and heated to reflux at approximately 573 K (set point) for 1 hour. After cooling, the particles were precipitated with ethanol and separated by centrifugation. The particles were redistributed in hexanes and precipitated again with ethanol and separated again by centrifugation and before finally being dispersed in hexanes.

[00202] Synthesis of CoO. The CoO was synthesized by thermal decomposition of cobalt (III) acetylacetonate, $Co(acac)_3$, in 10 mL of olelyamine (70 %). The $Co(acac)_3$ was combined at room temperature with the oleylamine using a magnetic stir bar, the temperature controller was set to 393 K and vacuum was pulled as the mixture was heated while stirring at 700 RPM. Vacuum was held at approximately 393 K (set point) for about 15 minutes, followed by the addition of an Ar blanket. The mixture was then heated to 413 K (set point) for 20 minutes followed by heating to 488 K (set point) for 1 hour. Once cooled the material was precipitated by the addition of ethanol and separated by centrifuge. The materials were dispersed in hexanes for storage. The synthesis of CoO materials was adapted from the work of Shi and He.

[00203] Synthesis of Ferrite/CoO nano-objects. The ferrite/CoO nano-objects were grown by adding the ferrite particles in a hexanes colloidal suspension to the mixture of $Co(acac)_3$ and oleylamine at room temperature. In detail, approximately 32 mg or 48 mg ferrites in hexanes were added by micropipette to 1 mmol or 0.75 mmol

of $Co(acac)_3$ in 10 mL of oleylamine (70 %) while the mixture was continuously stirred at 700 RPM by magnetic stir bar. The reaction vessel was sealed, and temperature was set to 393K while vacuum was pulled. During the heating vacuum was carefully controlled as the hexanes began to boil off, and vacuum was maintained at approximately 393 K (set point) for 15 minutes to ensure the hexanes was completely removed. The heating procedure was then performed in the same manner as the synthesis of the CoO synthesis. Once cooled the material was precipitated by the addition of ethanol and separated by centrifugation and dispersed in hexanes for storage.

[00204] Characterization of Magnetic Nano-objects. Powder X-ray diffraction (XRD) was performed with a Bruker D8 Discover X-ray diffractometer utilizing a Cu Kα radiation source. Bright field TEM images were taken with a FEI Titan 80-300 at 300 kV. HAADF-STEM images and EDXS elemental maps were collected using a different FEI Titan 80-300 TEM operating at an accelerating voltage of 300 kV and equipped with an EDAX r-TEM spectrometer. For EDXS analysis of the data K-shell transitions, which do not appreciably overlap, were chosen. Samples were drop cast onto 300-mesh carbon-Formvar copper grids (Ted Pella). Dynamic light scattering (DLS) was measured using a Malvern Instruments Zetasizer Nano operated in backscatter mode at 173° with a 633 nm wavelength laser. The DLS was performed on dilute samples (≥ 0.1 mg solids/mL) in hexanes. Raman spectrums were collected on samples drop cast on Au-coated Si using a Renishaw inVia system (1200 grooves / mm grating, 1" CCD detector), with 785 nm wavelength and at different powers as indicated. Liquid magnetic characterization was performed on a Superconducting Quantum Interference Device Vibrating-Sample Magnetometer (SQUID-VSM, Quantum Design). Liquid samples (about 70 µL) were mounted in LakeShore capsules and sealed using epoxy. The maximum applied field was 5,570,382 A/m (70,000 Oe) for M vs. H and 7964 A/m (100 Oe) for M vs. T measurements. AC susceptibility was made using AC fields of 7.96 A/m (0.1 Oe) and 79.64 A/m (1 Oe), in a frequency range from 1 Hz to 1 kHz. For temperature-dependent AC susceptibility the measurement temperature was changed from 200 K to 310 K. Magnetic particle spectroscopy (MPS) measurements were performed on a NIST built system and the drive field peak amplitudes were measured directly by Hall probe for a given frequency, voltage, and

amplifier gain. MPS was measured on samples in hexanes of approximately 1 mL volume in 2 mL capped vials.

[00205] Temperature Dependent Powder Magnetic Measurements

[00206] ZFC and ACS temperature dependent (fixed frequency) measurements were performed on powders of the ferrite particles, nanoflowers, and clusters, Figure S6. The ferrite particles show minimal change between 100 K and 400 K in the ZFC and real part of the ACS measurements, in contract the nanoflowers and clusters show increasing magnetization and real part of the ACS from low temperature toward approximately room temperature. The nanoflowers show similar trends in the ZFC and real part of the ACS as the clusters compared to the difference observed in the liquid samples. We believe this is most likely related to the nanoflowers becoming more cluster-like when in powder form due to being physically fixed and changes in inter-particle interactions from closer proximity.

[00207] While one or more embodiments have been shown and described, modifications and substitutions may be made thereto without departing from the spirit and scope of the invention. Accordingly, it is to be understood that the present invention has been described by way of illustrations and not limitation. Embodiments herein can be used independently or can be combined.

[00208] All ranges disclosed herein are inclusive of the endpoints, and the endpoints are independently combinable with each other. The ranges are continuous and thus contain every value and subset thereof in the range. Unless otherwise stated or contextually inapplicable, all percentages, when expressing a quantity, are weight percentages. The suffix (s) as used herein is intended to include both the singular and the plural of the term that it modifies, thereby including at least one of that term (e.g., the colorant(s) includes at least one colorants). Option, optional, or optionally means that the subsequently described event or circumstance can or cannot occur, and that the description includes instances where the event occurs and instances where it does not. As used herein, combination is inclusive of blends, mixtures, alloys, reaction products, collection of elements, and the like.

[00209] As used herein, a combination thereof refers to a combination comprising at least one of the named constituents, components, compounds, or

elements, optionally together with one or more of the same class of constituents, components, compounds, or elements.

[00210] All references are incorporated herein by reference.

[00211] The use of the terms “a,” “an,” and “the” and similar referents in the context of describing the invention (especially in the context of the following claims) are to be construed to cover both the singular and the plural, unless otherwise indicated herein or clearly contradicted by context. It can further be noted that the terms first, second, primary, secondary, and the like herein do not denote any order, quantity, or importance, but rather are used to distinguish one element from another. It will also be understood that, although the terms first, second, etc. are, in some instances, used herein to describe various elements, these elements should not be limited by these terms. For example, a first current could be termed a second current, and, similarly, a second current could be termed a first current, without departing from the scope of the various described embodiments. The first current and the second current are both currents, but they are not the same condition unless explicitly stated as such.

[00212] The modifier about used in connection with a quantity is inclusive of the stated value and has the meaning dictated by the context (e.g., it includes the degree of error associated with measurement of the particular quantity). The conjunction or is used to link objects of a list or alternatives and is not disjunctive; rather the elements can be used separately or can be combined together under appropriate circumstances.

What is claimed is:

1. A magnetically-responsive thermal sensor for determining the temperature of a local microscale volume, the magnetically-responsive thermal sensor comprising:

a magnetic nano-thermometer that comprises a main magnetic layer and a subordinate magnetic layer disposed on the main magnetic layer, such that:

the main magnetic layer comprises a first magnetic material that:

couples, via magnetic coupling, with the subordinate magnetic layer; or

has a large change in magnetization as a function of temperature that produces a magnetic phase transition of the main magnetic layer; and

the subordinate magnetic layer comprises a second magnetic material that:

couples, via magnetic coupling, with the main magnetic layer; or

has a large change in magnetization as a function of temperature that produces a magnetic phase transition of the subordinate magnetic layer,

wherein the magnetic nano-thermometer produces a magnetic response from which the temperature of the local microscale environment is determined.

2. The magnetically-responsive thermal sensor of claim 1, further comprising a matrix in which the magnetic nano-thermometer are disposed.

3. The magnetically-responsive thermal sensor of claim 1, further comprising a coil disposed proximate to the magnetic nano-thermometer and that subjects the magnetic nano-thermometer to a magnetic field.

4. The magnetically-responsive thermal sensor of claim 3, wherein the magnetic nano-thermometer includes a plurality of the coil arranged as a pair that is opposingly disposed such that the magnetic nano-thermometer is interposed between each coil of the pair of coils.

5. The magnetically-responsive thermal sensor of claim 4, wherein the magnetic nano-thermometer includes single pair of coils, two pairs of coils, or three pairs of coils, such that each coil in a pair is independently controlled, and each pair of coils is independently controlled to produce a separate and orthogonally oriented magnetic field.

6. The magnetically-responsive thermal sensor of claim 3, wherein the magnetic nano-thermometer receives the magnetic field and produces a magnetic response in response to the magnetic field.

7. The magnetically-responsive thermal sensor of claim 6, further comprising a sensor disposed proximate to the magnetic nano-thermometer and that receives the magnetic response from the magnetic nano-thermometer and produces a sensor signal based on the magnetic response received from the magnetic nano-thermometer.

8. The magnetically-responsive thermal sensor of claim 7, wherein the sensor comprises a pick-up coil, a superconducting quantum interference device, a hall sensor, a flux gate, a magnetoresistive sensor, or a combination comprising at least one of the foregoing type of sensor.

9. The magnetically-responsive thermal sensor of claim 7, further comprising a temperature analyzer in electrical communication with the sensor and that receives the sensor signal from the sensor and determines a temperature of the local microscale environment based on the magnetic response produced by the magnetic nano-thermometer.

10. The magnetically-responsive thermal sensor of claim 1, wherein the magnetic nano-thermometer further comprises a medial magnetic layer disposed on the main magnetic layer and interposed between the main magnetic layer and the subordinate magnetic layer.

11. The magnetically-responsive thermal sensor of claim 10, wherein the medial magnetic layer comprises a non-magnetic material and facilitates antiferromagnetic coupling between the main magnetic layer and the subordinate magnetic layer.

12. The magnetically-responsive thermal sensor of claim 1, wherein the magnetic nano-thermometer further comprises a substrate on which is disposed the main magnetic layer and the subordinate magnetic layer and arranged in a pillar structure on the substrate.

13. The magnetically-responsive thermal sensor of claim 1, wherein the magnetic nano-thermometer further comprises a core-shell structure comprising a core and a shell disposed on and surrounding the core, wherein the main magnetic layer is arranged in the core and the subordinate magnetic layer is arranged in the shell.

14. The magnetically-responsive thermal sensor of claim 1, wherein the magnetic nano-thermometer includes a plurality of the main magnetic layer and a plurality of the subordinate magnetic layer arranged so that layers of the main magnetic layer and layers of the subordinate magnetic layer sequentially alternate in the magnetic nano-thermometer.

15. The magnetically-responsive thermal sensor of claim 1, wherein the main magnetic layer comprises iron.

16. The magnetically-responsive thermal sensor of claim 1, wherein the subordinate magnetic layer comprises gadolinium.

17. The magnetically-responsive thermal sensor of claim 1, wherein the magnetic coupling between the main magnetic layer and the subordinate magnetic layer is antiferromagnet coupling.

18. The magnetically-responsive thermal sensor of claim 1, wherein the magnetic coupling between the main magnetic layer and the subordinate magnetic layer is ferromagnetic coupling.

19. The magnetically-responsive thermal sensor of claim 1, wherein the matrix comprises a solid, a fluid, or a combination comprising at least one of the foregoing states of matter.

20. A process for determining the temperature of a local microscale volume with a magnetically-responsive thermal sensor, the process comprising:

disposing the magnetically-responsive thermal sensor in the local microscale environment, the magnetically-responsive thermal sensor comprising:

a magnetic nano-thermometer that comprises a main magnetic layer and a subordinate magnetic layer disposed on the main magnetic layer, such that:

the main magnetic layer comprises a first magnetic material that:

couples, via magnetic coupling, with the subordinate magnetic layer; or

has a large change in magnetization as a function of temperature that produces a magnetic phase transition of the main magnetic layer; and

the subordinate magnetic layer comprises a second magnetic material that:

couples, via magnetic coupling, with the main magnetic layer; or

has a large change in magnetization as a function of temperature that produces a magnetic phase transition of the subordinate magnetic layer;

a matrix in which the magnetic nano-thermometer are disposed;

a coil disposed proximate to the magnetic nano-thermometer; and

a sensor disposed proximate to the magnetic nano-thermometer;

producing, by the coil, a magnetic field, wherein the magnetic field comprises an alternating magnetic field such that a field-free point or line is produced in a volume of the local microscale environment in which is disposed the magnetic nano-thermometer;

subjecting the local microscale environment and the magnetic nano-thermometer to the magnetic field from the coil;

producing, by the magnetic nano-thermometer, a magnetic response in response to the magnetic nano-thermometer receiving the magnetic field from the coil;

receiving, by the sensor, the magnetic response from the magnetic nano-thermometer;

producing, by the sensor, a sensor signal in response to receiving the magnetic response from the magnetic nano-thermometer;

receiving, by the temperature analyzer, the sensor signal from the sensor; and

determining, by the temperature analyzer, the temperature of the local microscale environment based on the magnetic response by obtaining frequency components in the sensor signal; comparing a set of harmonic frequency components to calibration data from which the temperature is obtained.

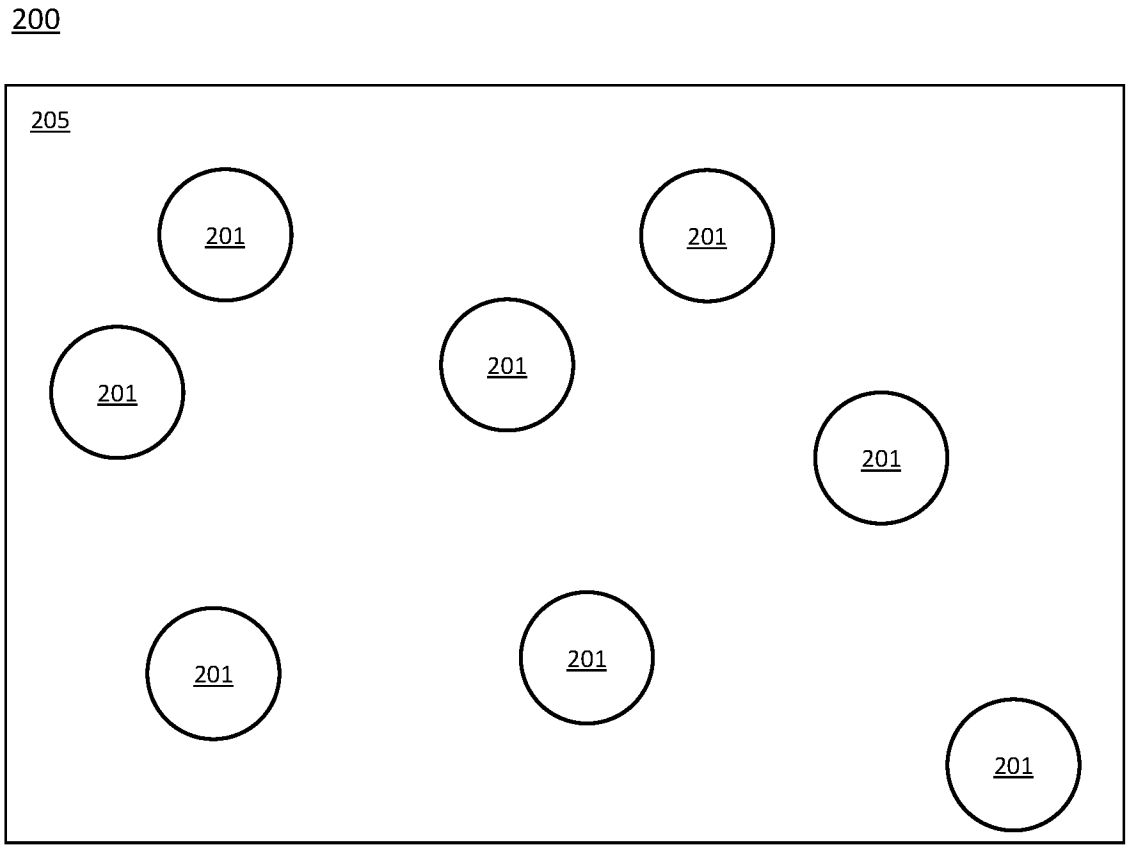

FIG. 1

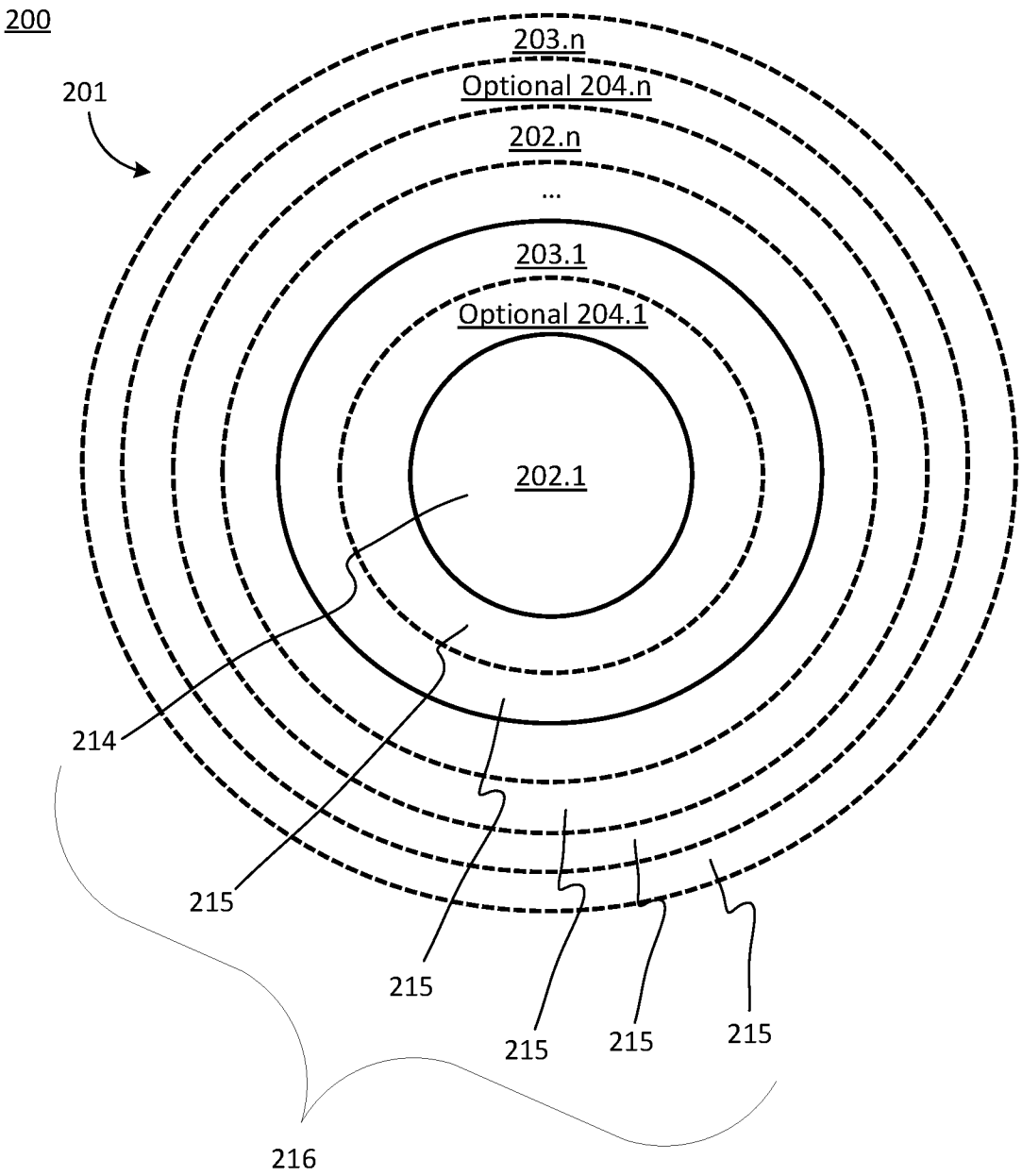
200
201
203.n
Optional 204.n
202.n
...
203.1
Optional 204.1
202.1
214
215
215
215
215
215
216

FIG. 2

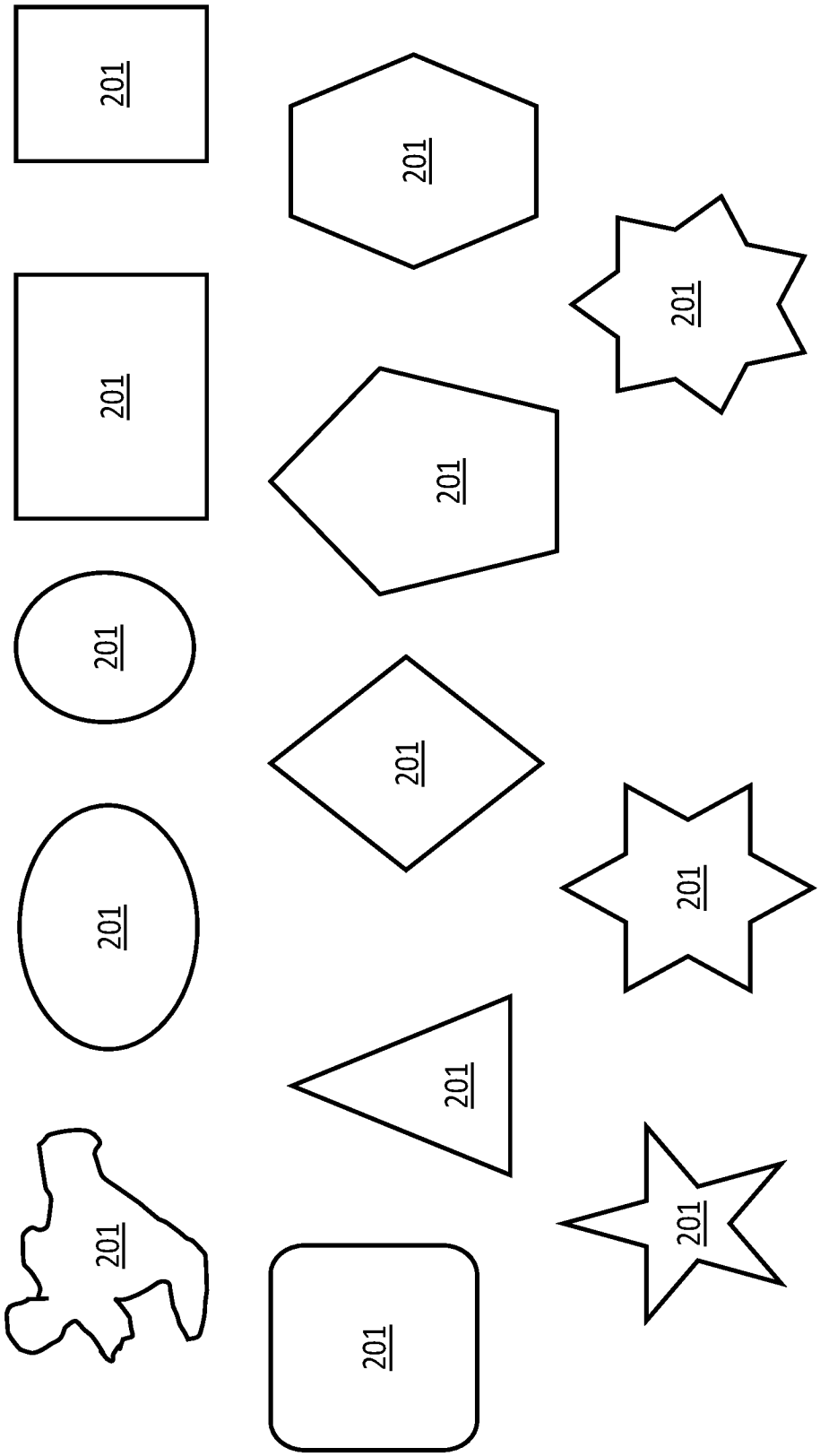

FIG. 3

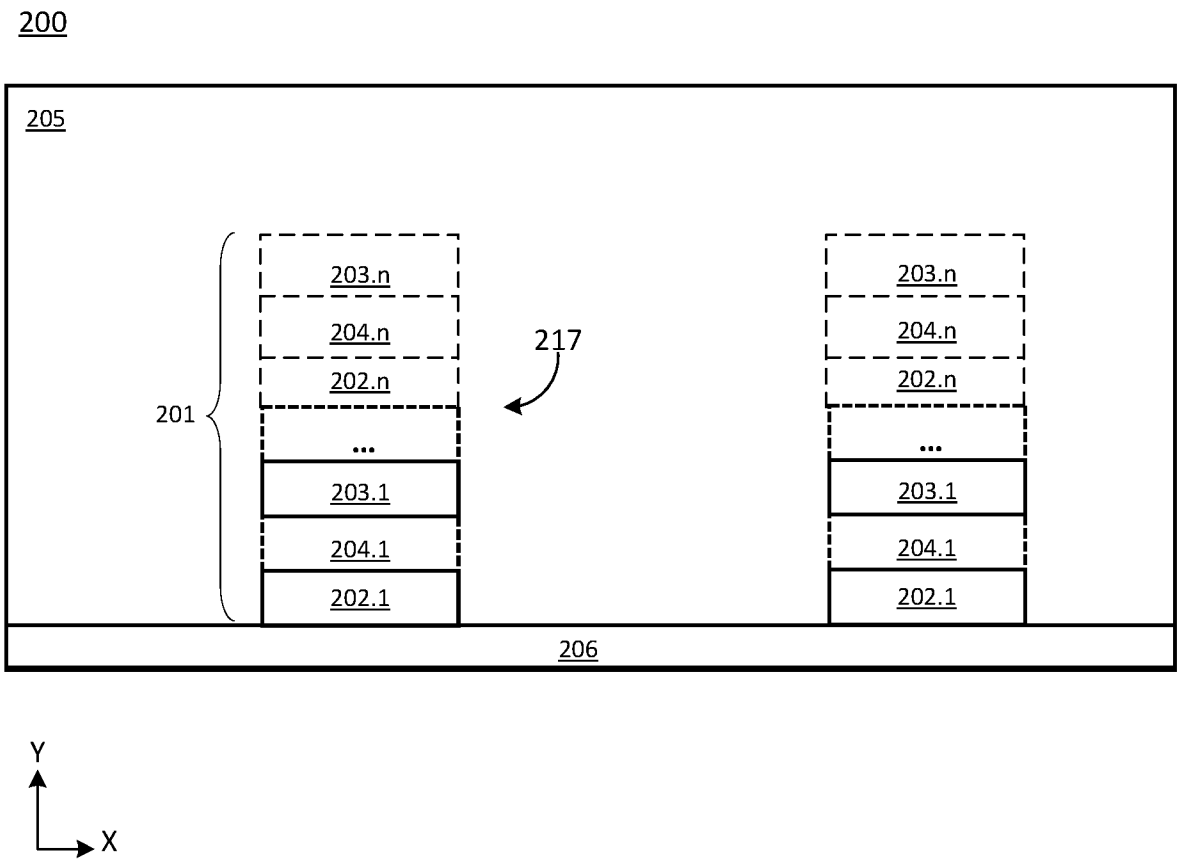
200
205
203.n
204.n
202.n
...
203.1
204.1
202.1
201
217
203.n
204.n
202.n
...
203.1
204.1
202.1
206
Y
X

FIG. 4

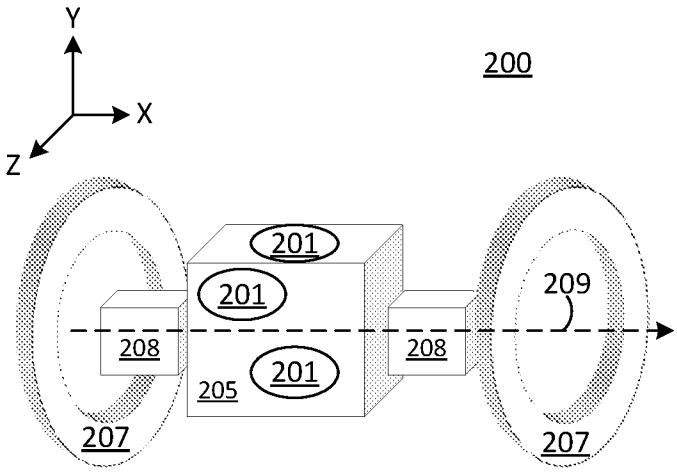

FIG. 5

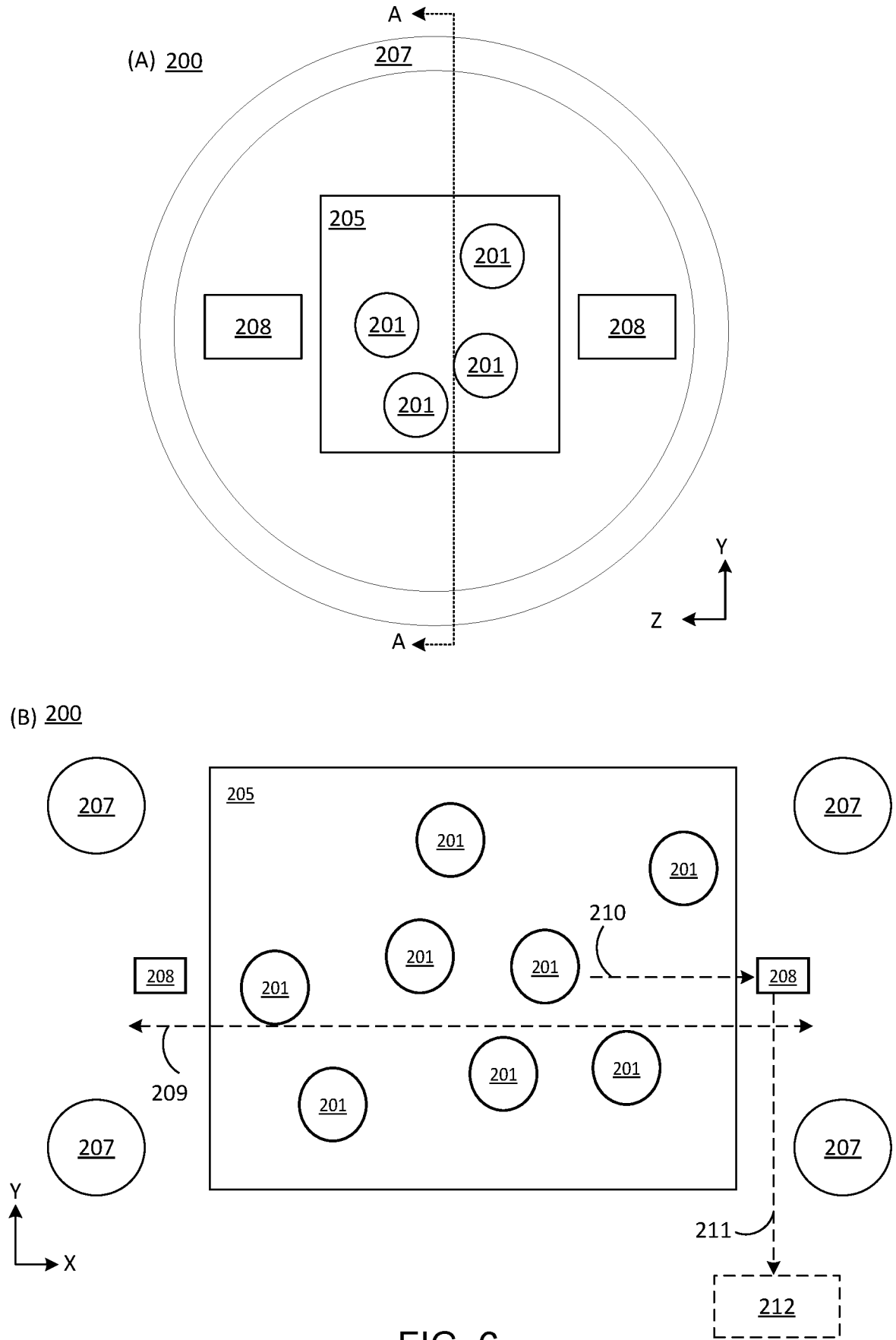
(A) 200
A
207
205
201
208
208
201
201
201
A
Y
Z
(B) 200
207
205
207
201
201
210
208
201
201
208
201
209
201
201
207
207
Y
X
211
212

FIG. 6

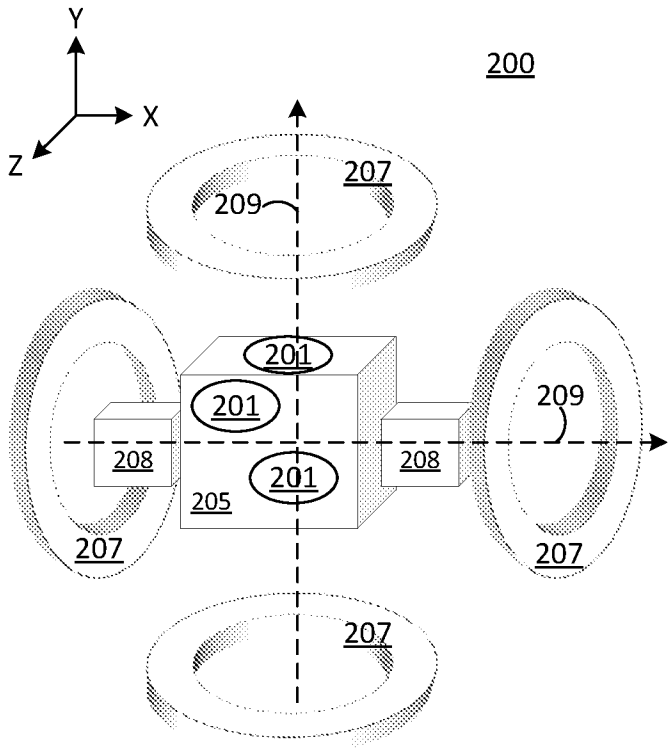

FIG. 7

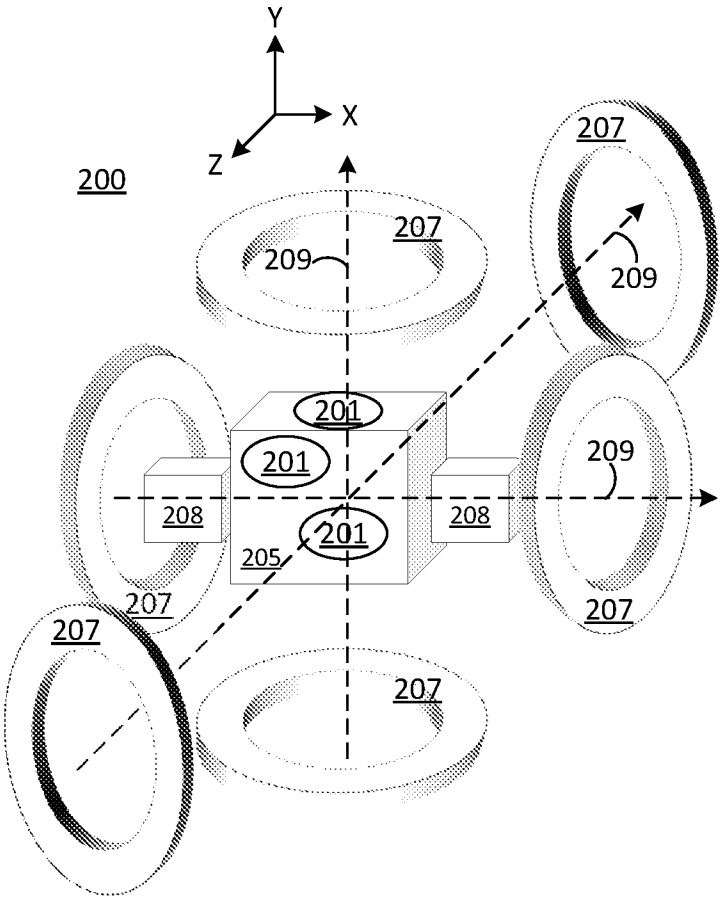

FIG. 8

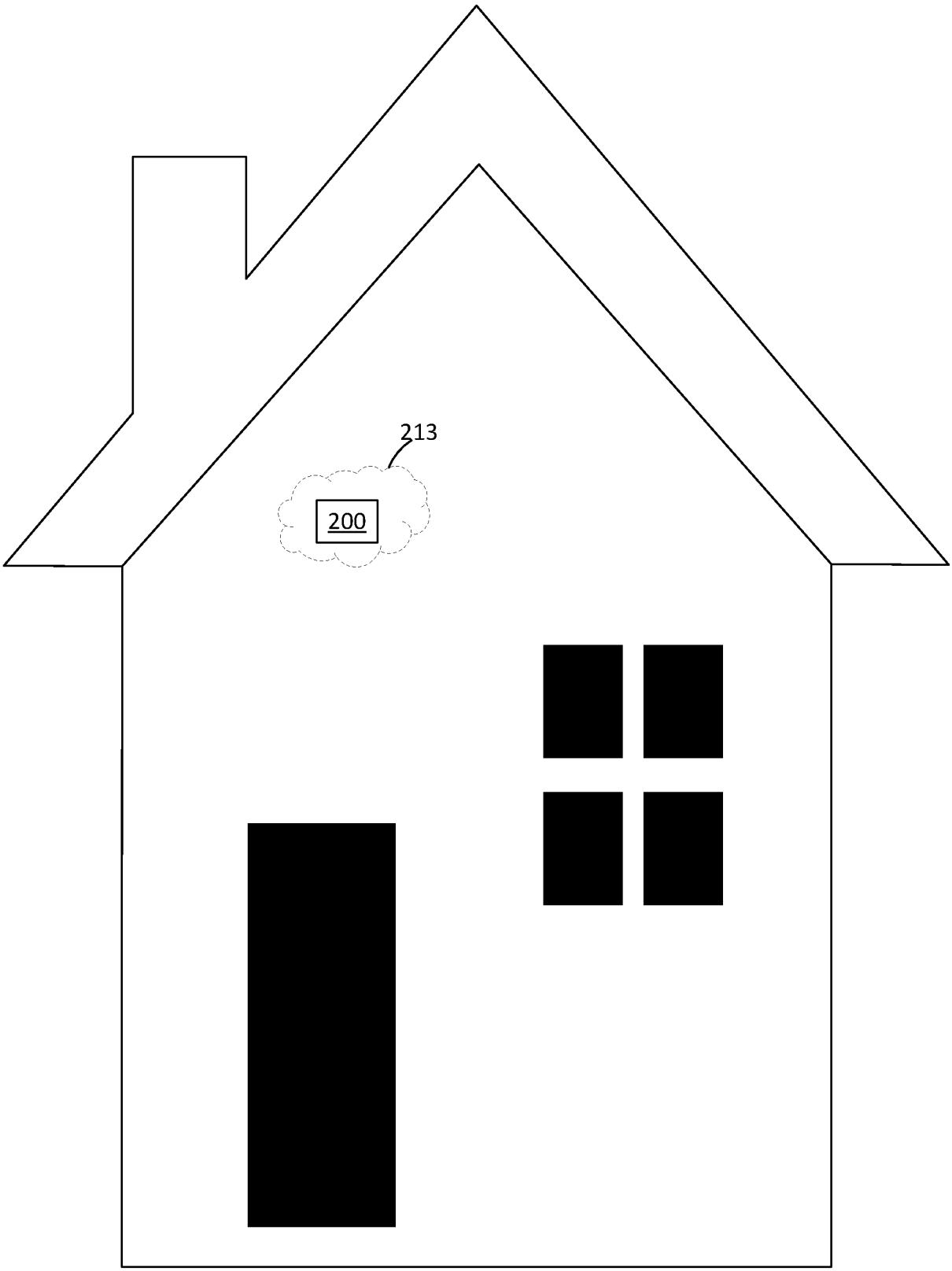

FIG. 9

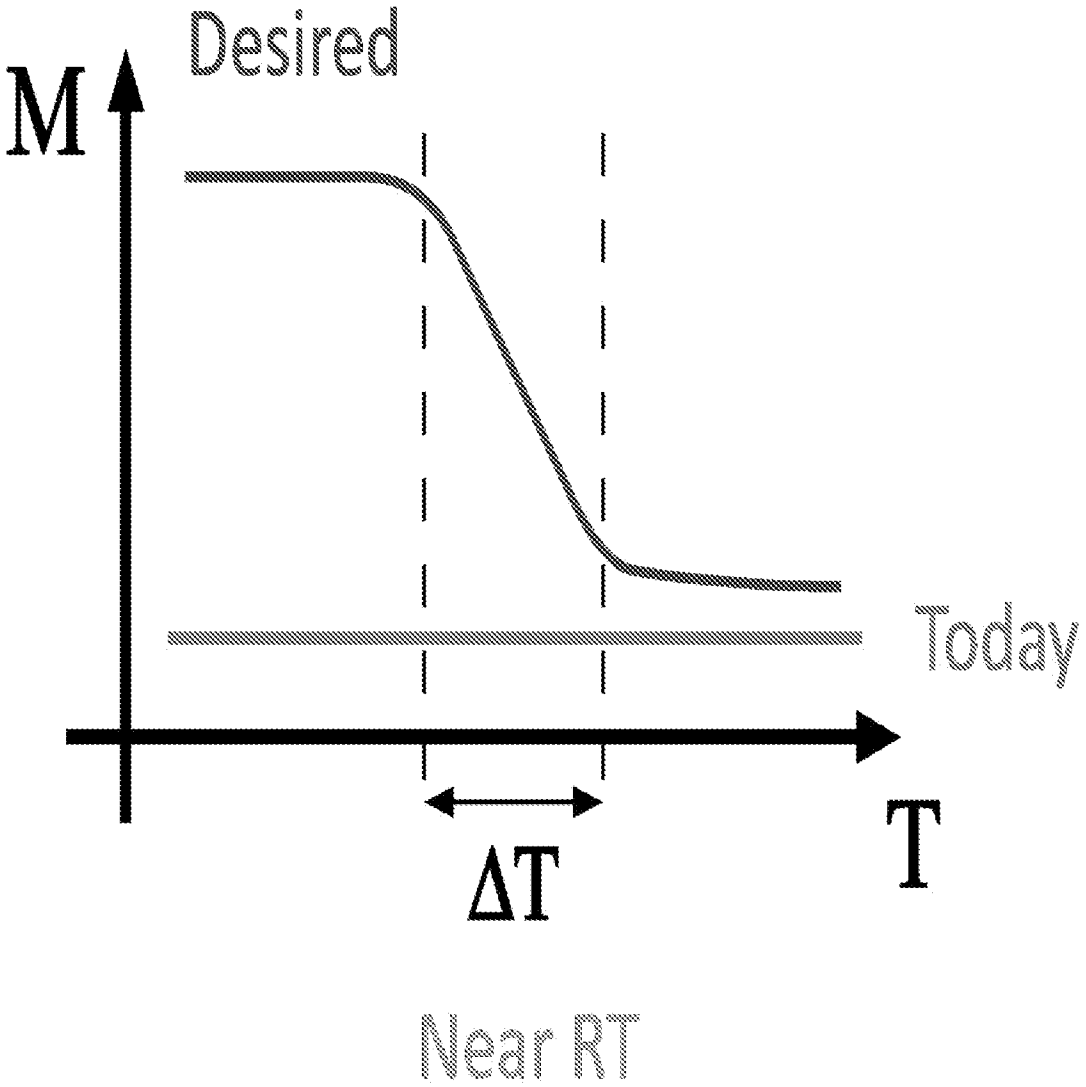

FIG. 10

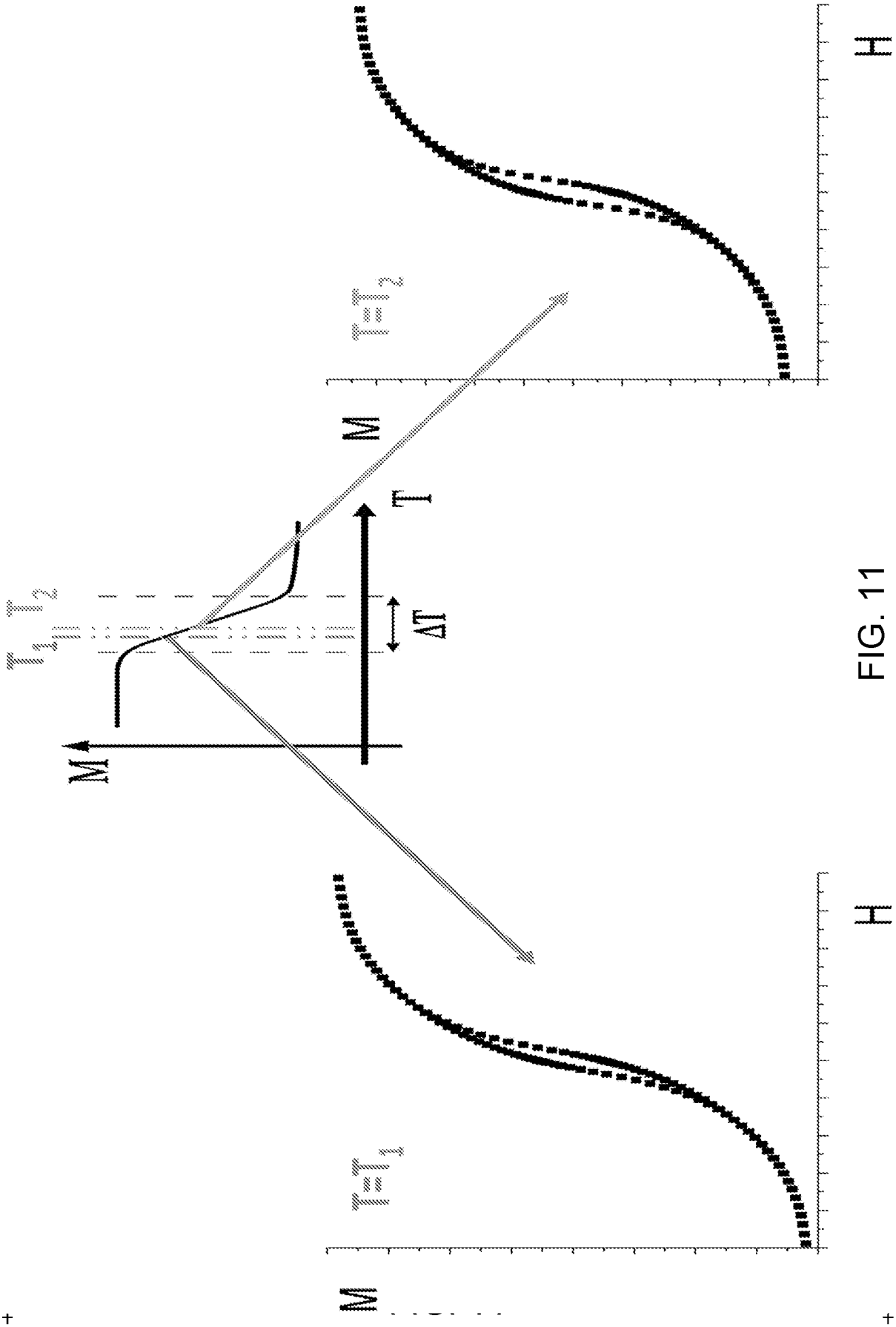

FIG. 11

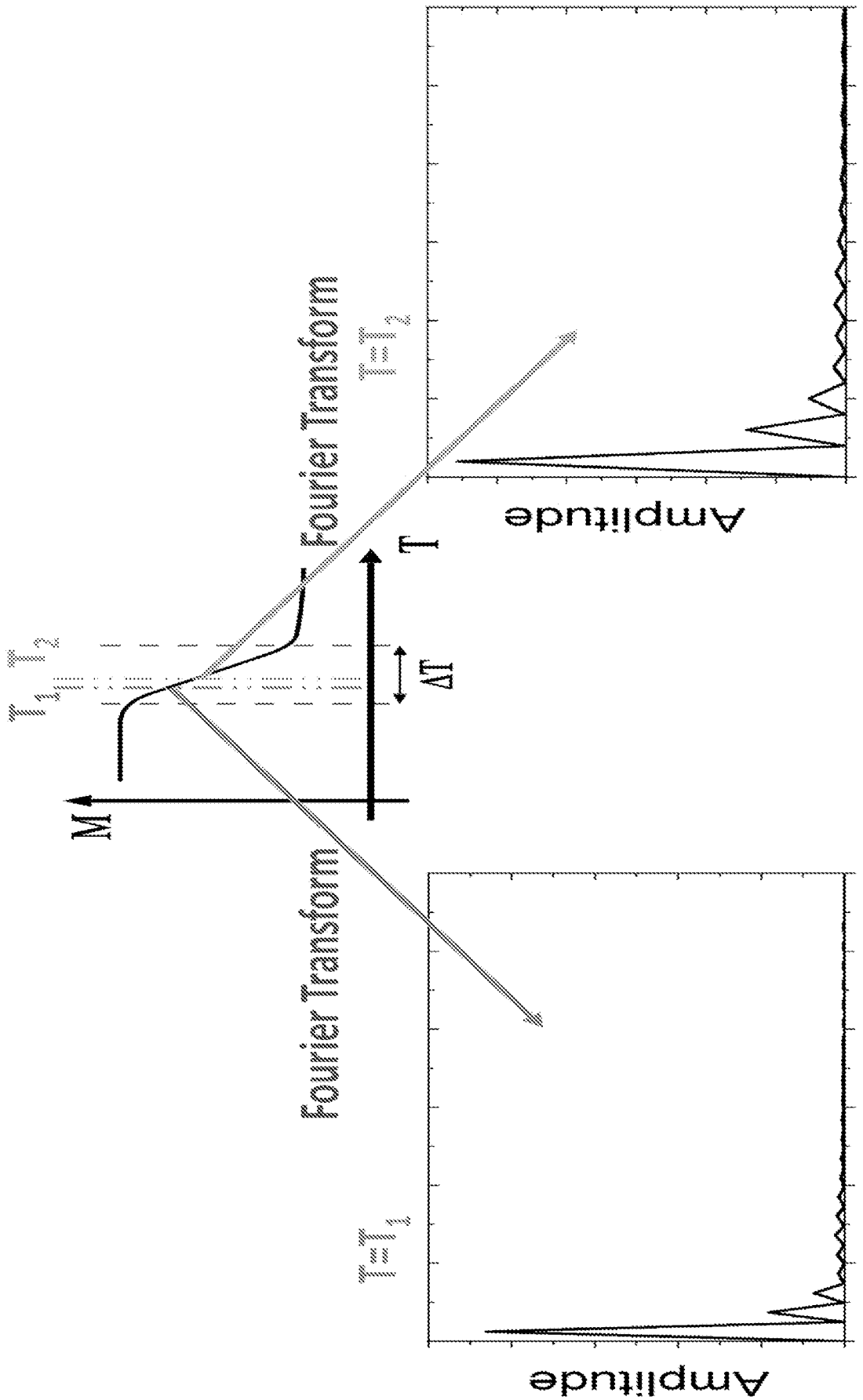
Amplitude
Components
T=T1
Fourier Transform
M
T1 T2
ΔT
T
Fourier Transform
T=T2
Amplitude
Components

FIG. 12

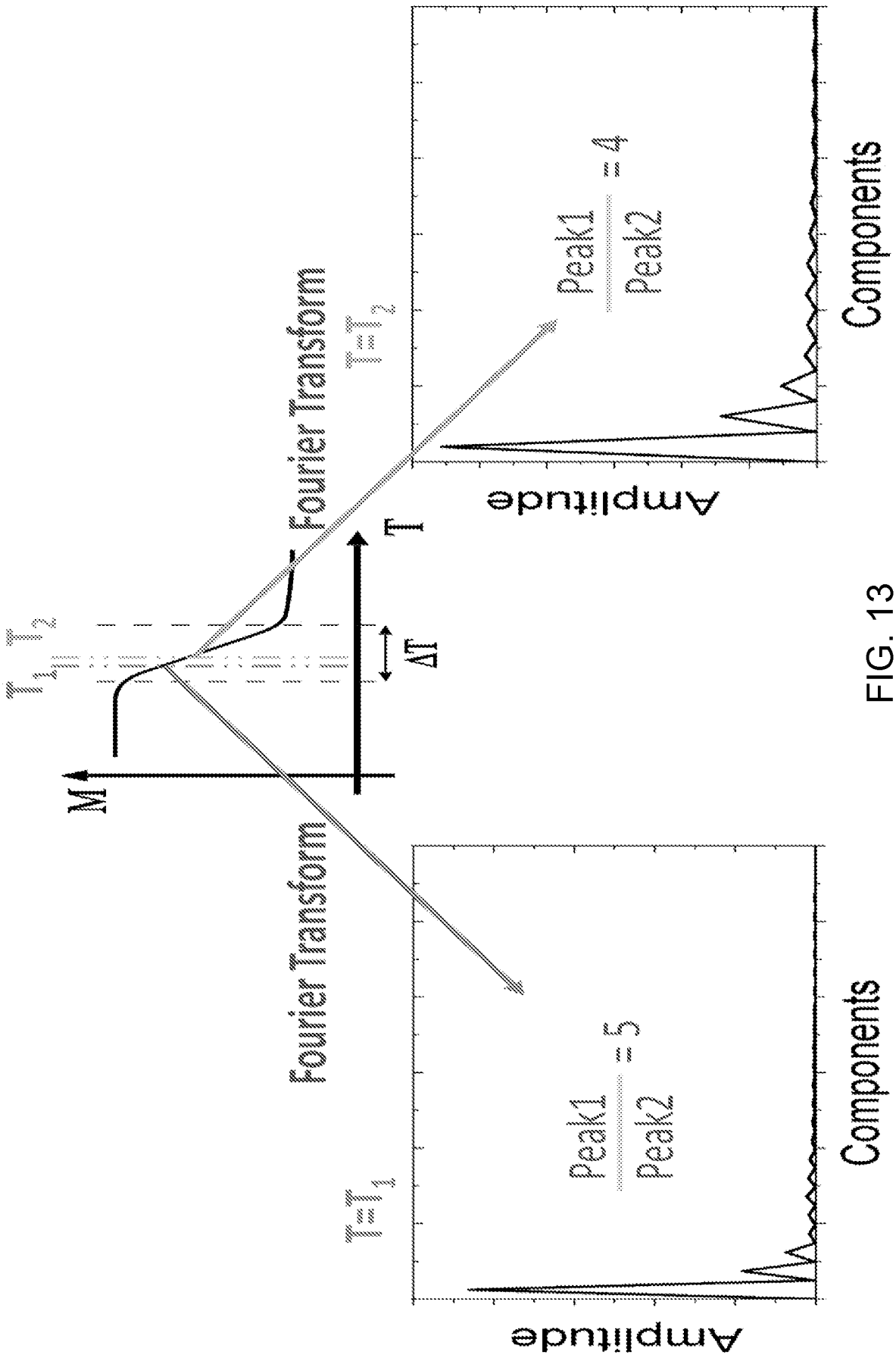
M
T
ΔT
T1 T2
Fourier Transform
Fourier Transform
T=T1
T=T2
Peak1 / Peak2 = 5
Peak1 / Peak2 = 4
Amplitude
Components
Amplitude
Components

FIG. 13

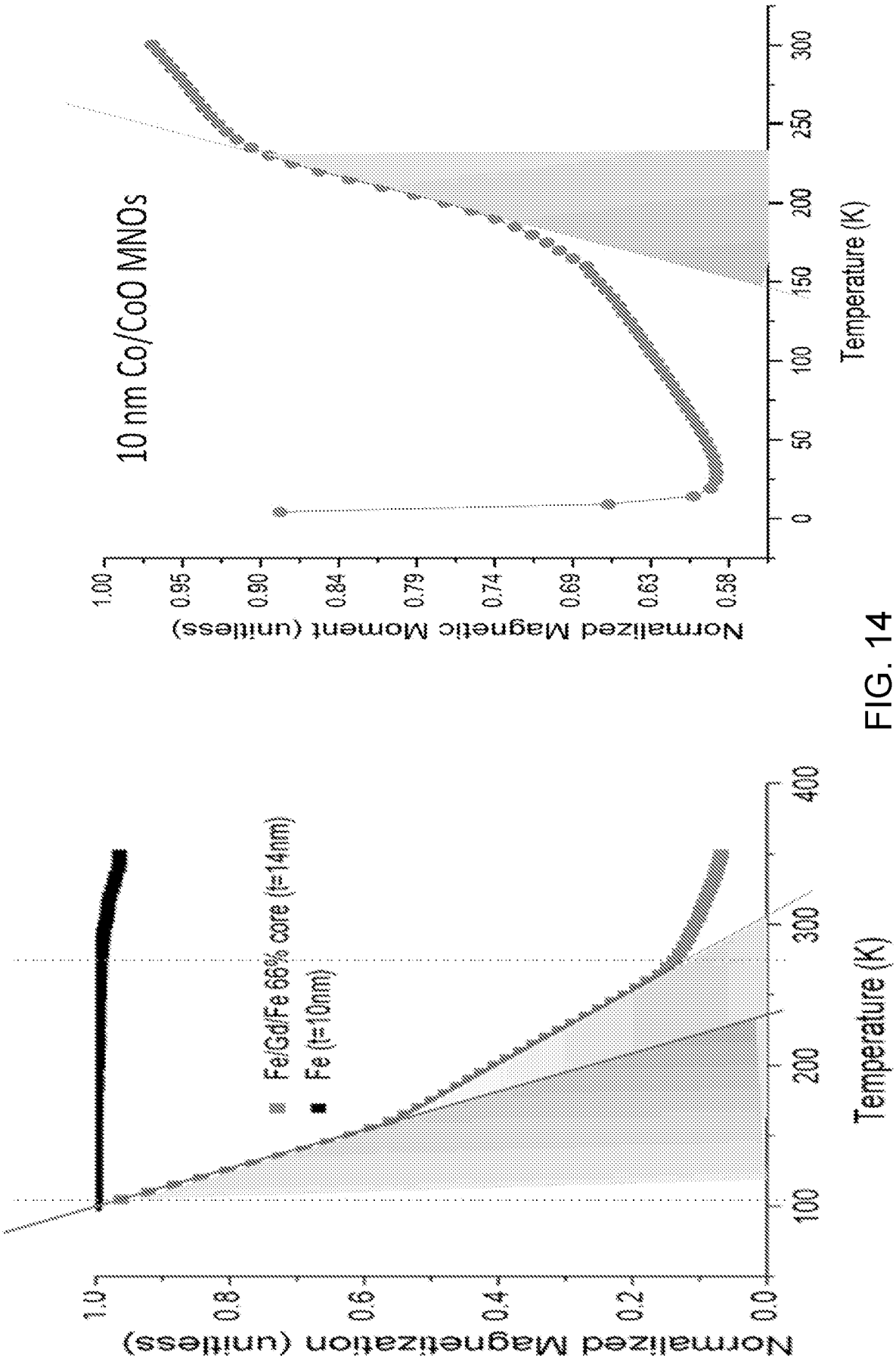
Normalized Magnetization (unitless)
1.0
0.8
0.6
0.4
0.2
0.0
100
200
300
400
Temperature (K)
Fe/Gd/Fe 66% core (t=14nm)
Fe (t=10nm)
10 nm Co/CoO MNOs
Normalized Magnetic Moment (unitless)
1.00
0.95
0.90
0.84
0.79
0.74
0.69
0.63
0.58
0
50
100
150
200
250
300
Temperature (K)

FIG. 14

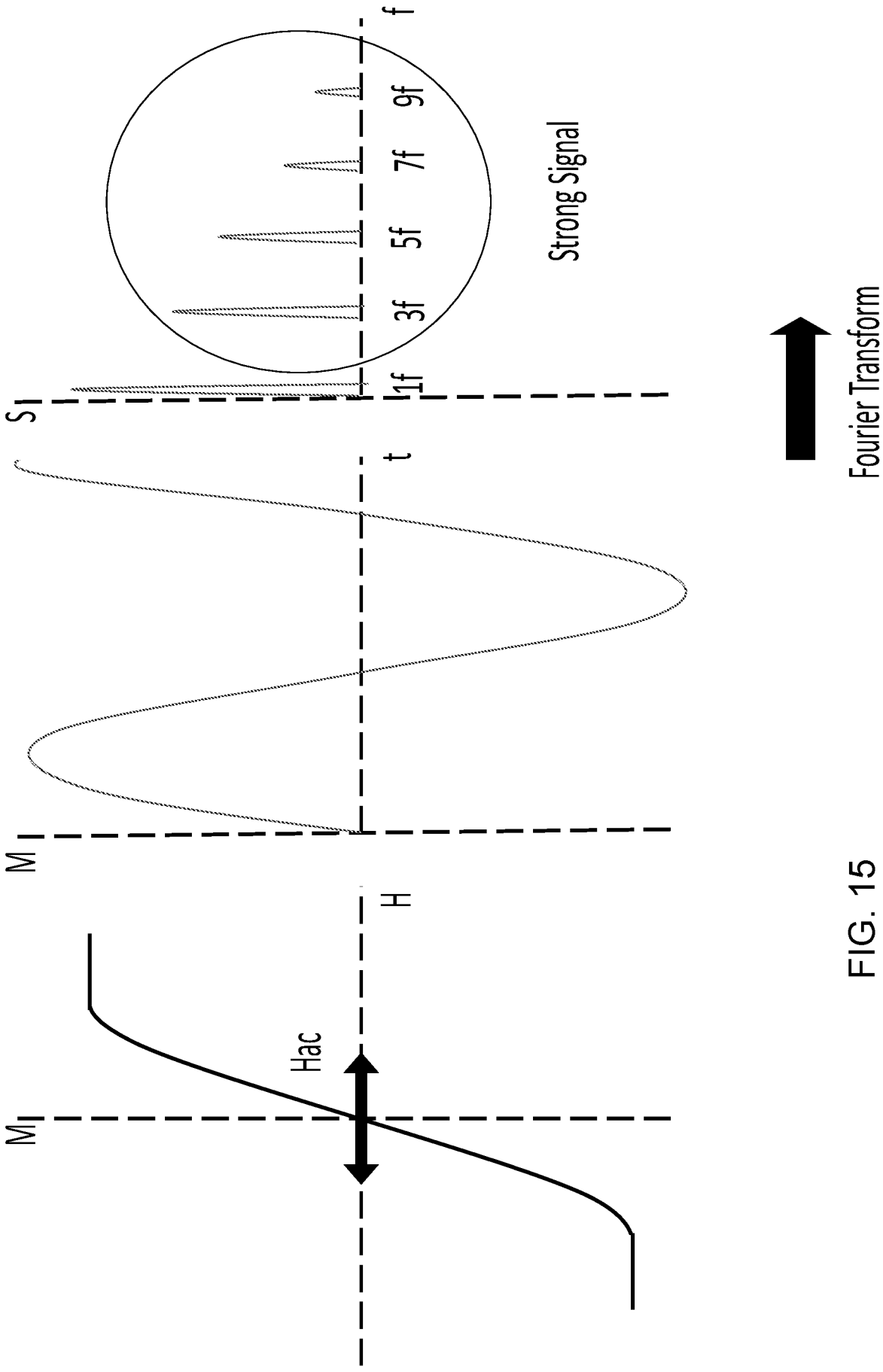

FIG. 15

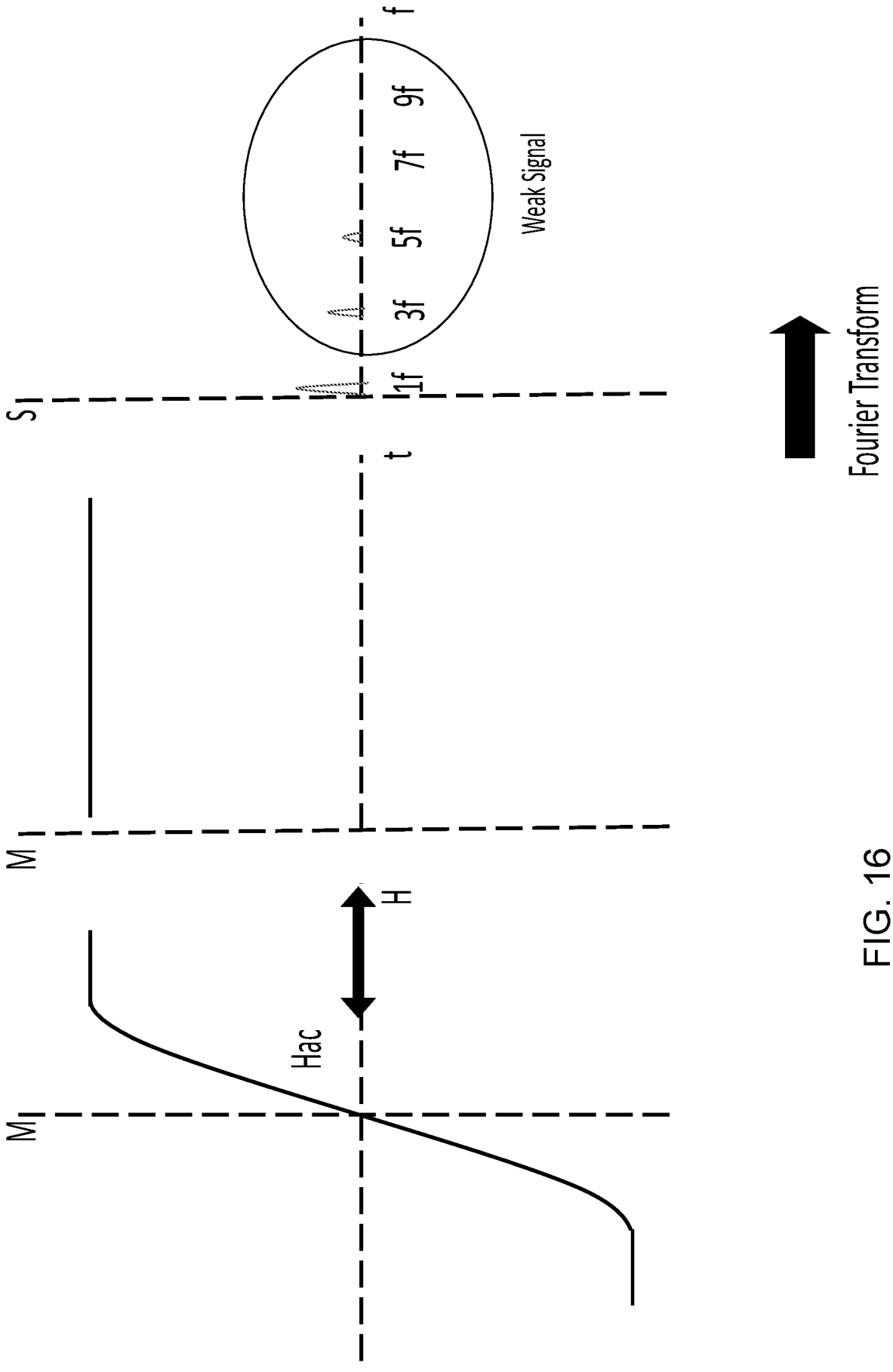

FIG. 16

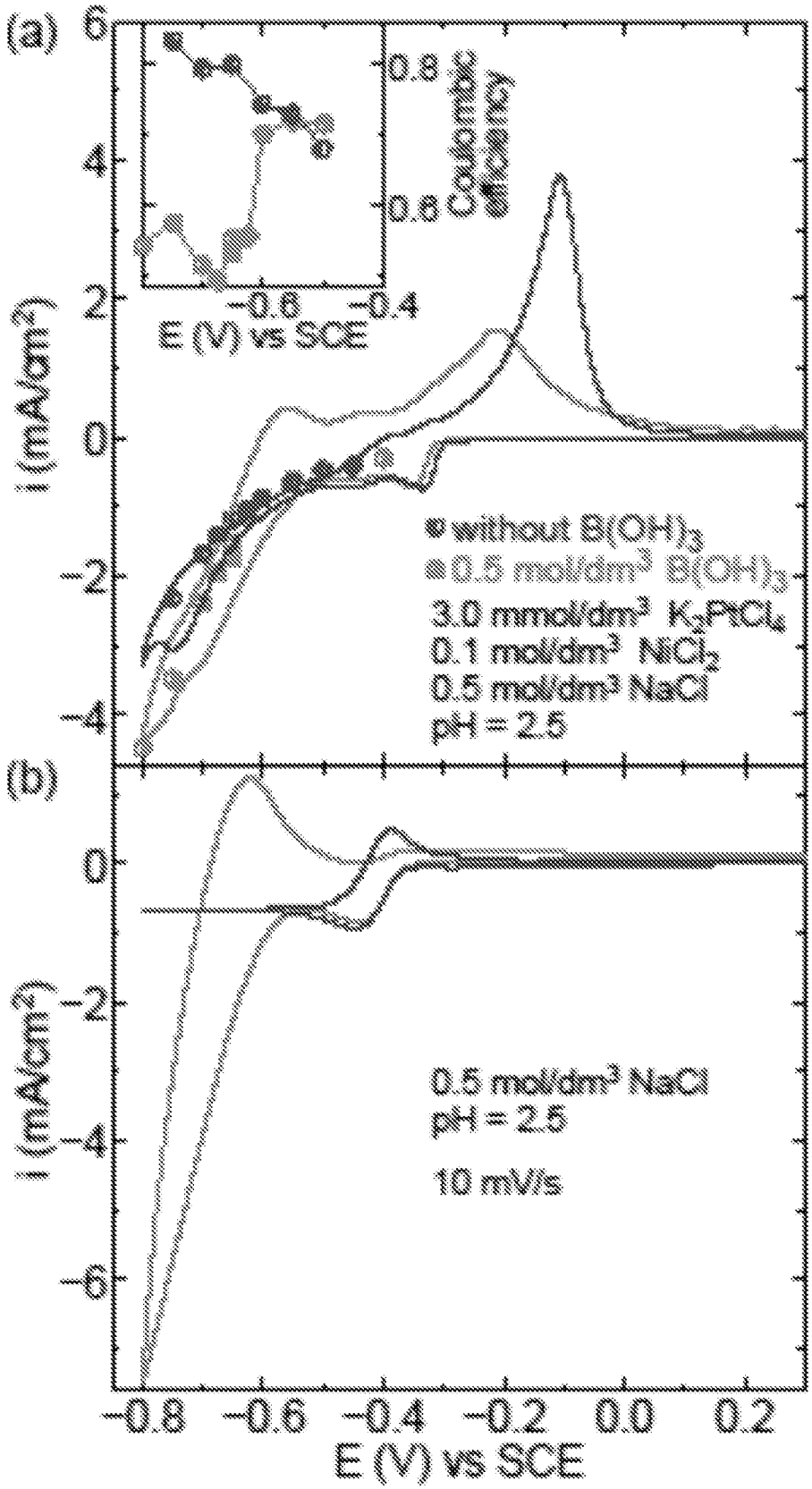
(a)
(b)
i (mA/cm²)
E (V) vs SCE
Coulombic efficiency
without B(OH)3
0.5 mol/dm³ B(OH)3
3.0 mmol/dm³ K2PtCl4
0.1 mol/dm³ NiCl2
0.5 mol/dm³ NaCl
pH = 2.5
10 mV/s

FIG. 17

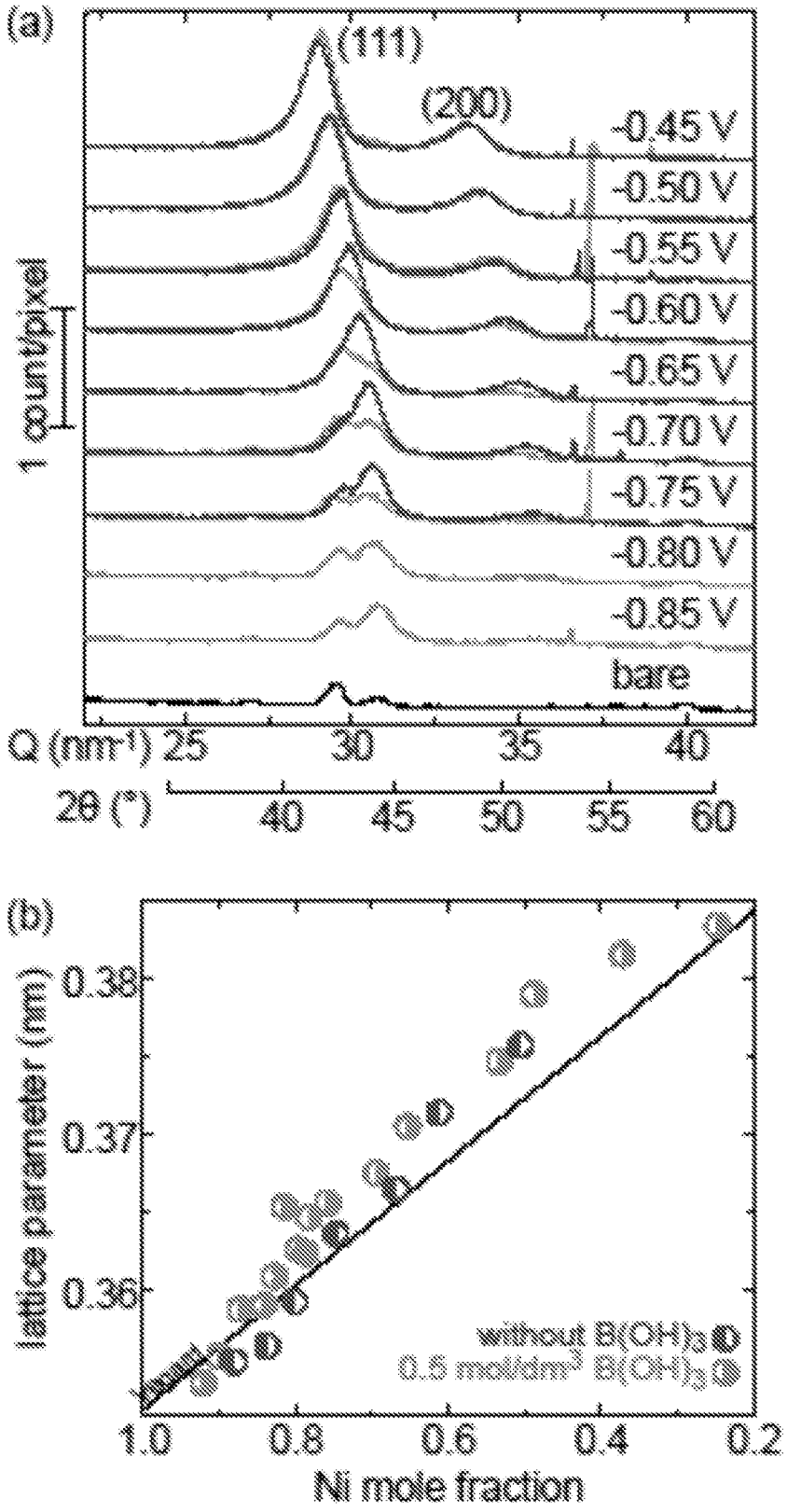
(a)
(111)
(200)
-0.45 V
-0.50 V
-0.55 V
-0.60 V
-0.65 V
-0.70 V
-0.75 V
-0.80 V
-0.85 V
bare
1 count/pixel
Q (nm-1) 25 30 35 40
2θ (°) 40 45 50 55 60
(b)
lattice parameter (nm)
0.38
0.37
0.36
without B(OH)3
0.5 mol/dm3 B(OH)3
1.0 0.8 0.6 0.4 0.2
Ni mole fraction

FIG. 18

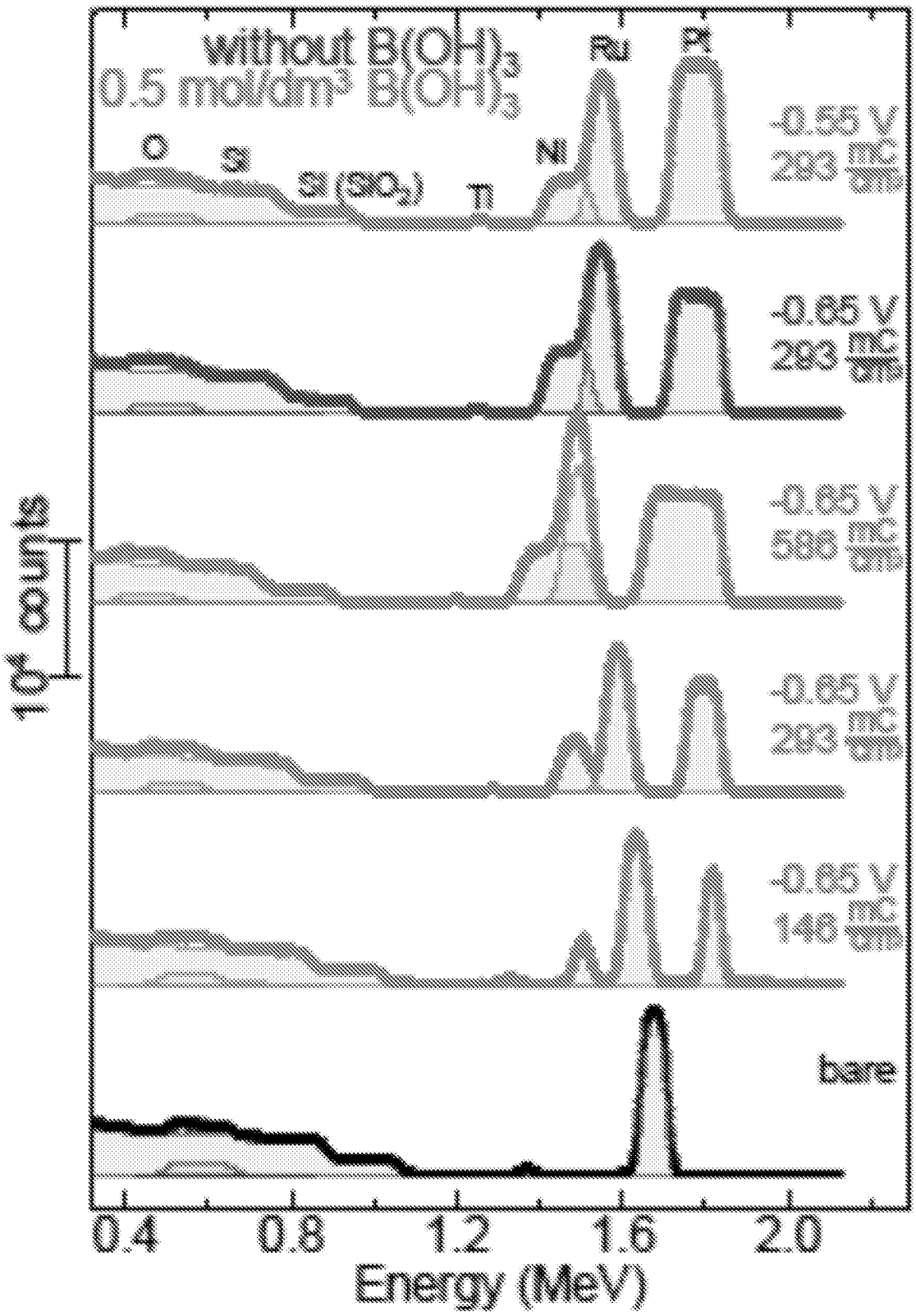
without B(OH)3
0.5 mol/dm3 B(OH)3
O
Si
Si (SiO2)
Ti
Ni
Ru
Pt
-0.55 V
293 mC/cm2
-0.65 V
293 mC/cm2
-0.65 V
586 mC/cm2
-0.65 V
293 mC/cm2
-0.65 V
146 mC/cm2
bare
10^4 counts
0.4
0.8
1.2
1.6
2.0
Energy (MeV)

FIG. 19

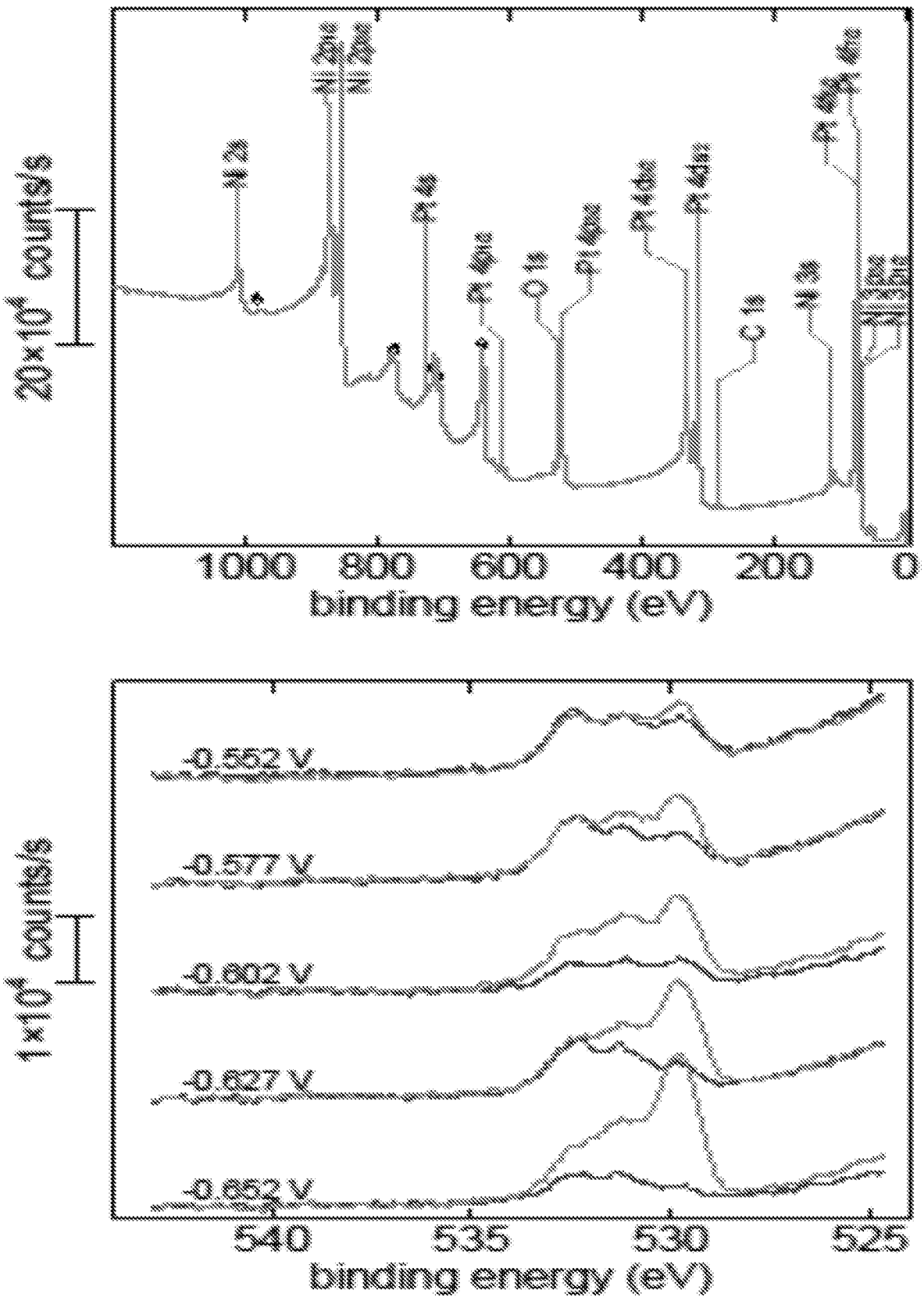
20×10⁴ counts/s
1000
800
600
400
200
0
binding energy (eV)
1×10⁴ counts/s
-0.562 V
-0.577 V
-0.602 V
-0.627 V
-0.652 V
540
535
530
525
binding energy (eV)

FIG. 20

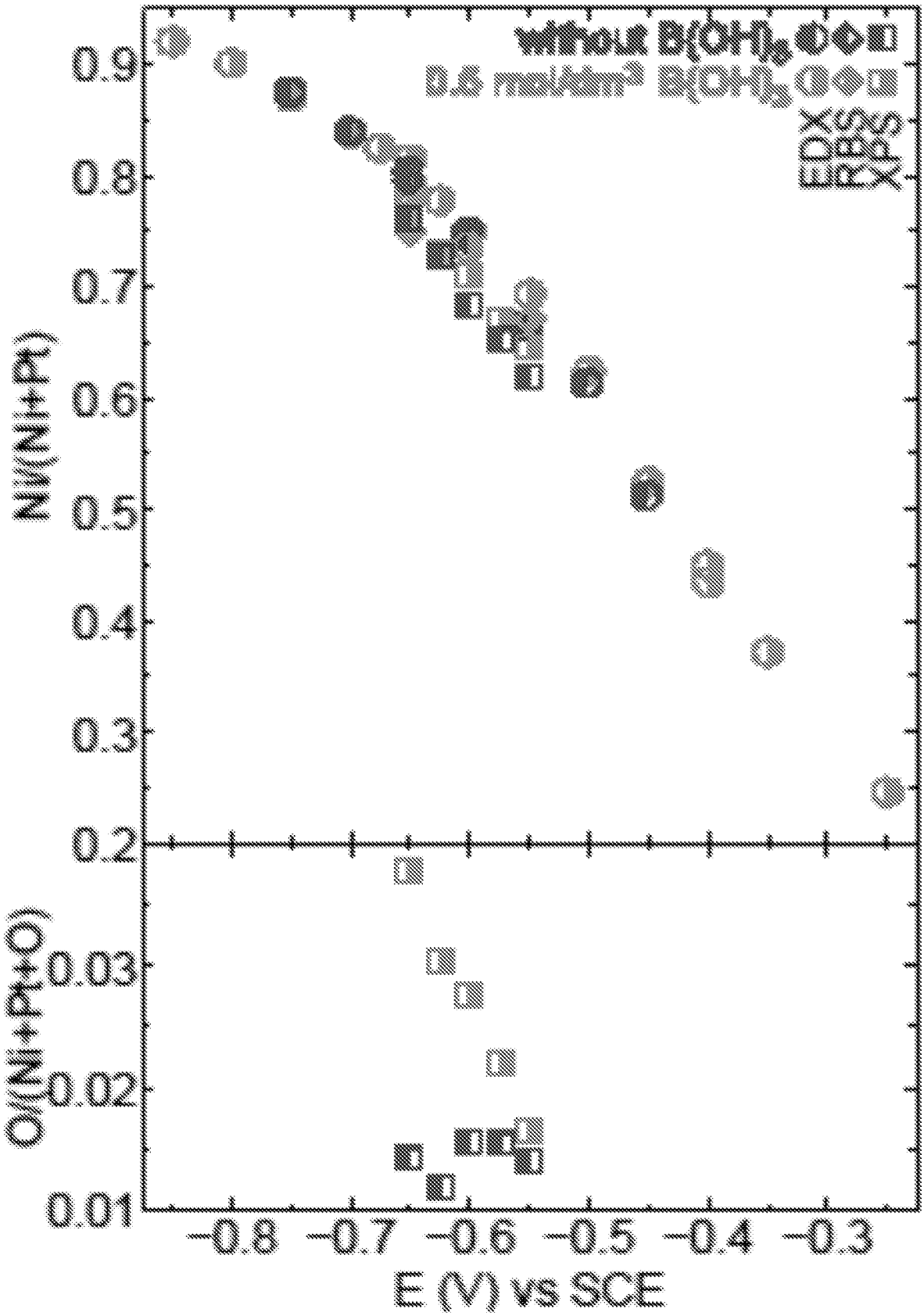
Without B(OH)3
0.6 mol/dm3 B(OH)3
EDX
BBS
XPS
Ni/(Ni+Pt)
O/(Ni+Pt+O)
E (V) vs SCE
0.9
0.8
0.7
0.6
0.5
0.4
0.3
0.2
0.03
0.02
0.01
−0.8
−0.7
−0.6
−0.5
−0.4
−0.3

FIG. 21

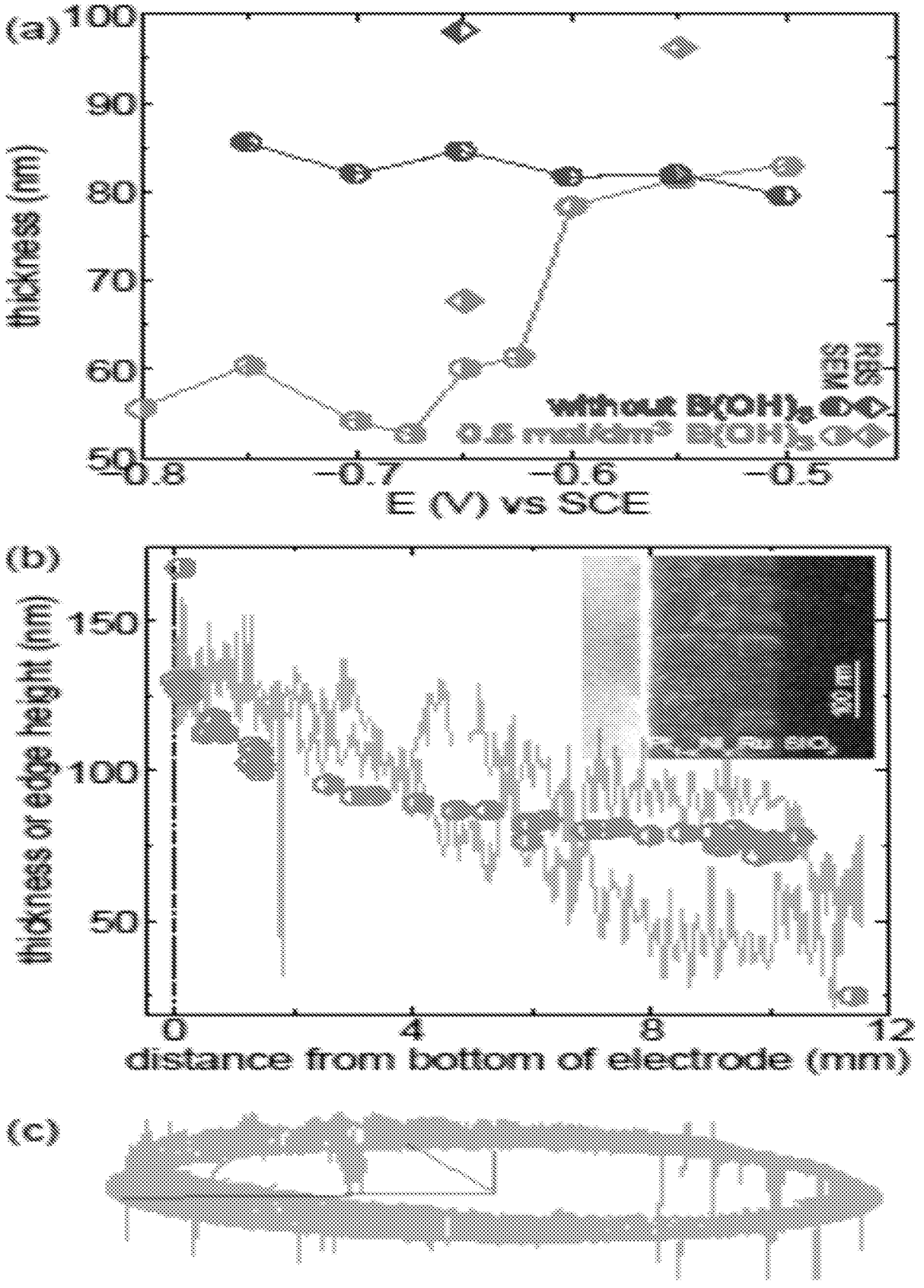
(a)
thickness (nm)
E (V) vs SCE
without B(OH)3
0.8 mol/dm3 B(OH)3
(b)
thickness or edge height (nm)
distance from bottom of electrode (mm)
(c)

FIG. 22

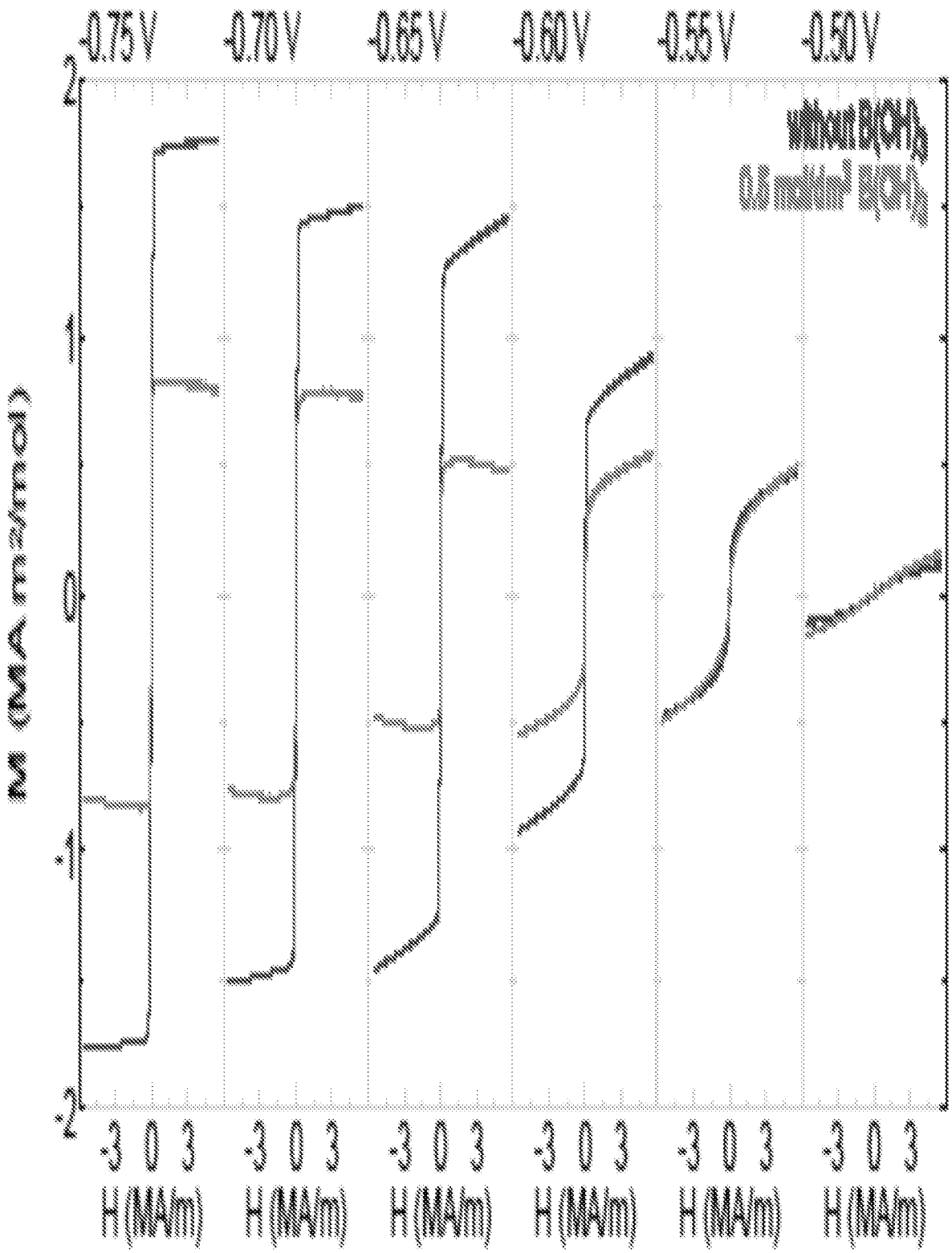
-0.75 V
-0.70 V
-0.65 V
-0.60 V
-0.55 V
-0.50 V
without B(OH)3
0.5 mM H3BO3
M (MA m2/mol)
2
1
0
-1
-2
-3 0 3
H (MA/m)

FIG. 23

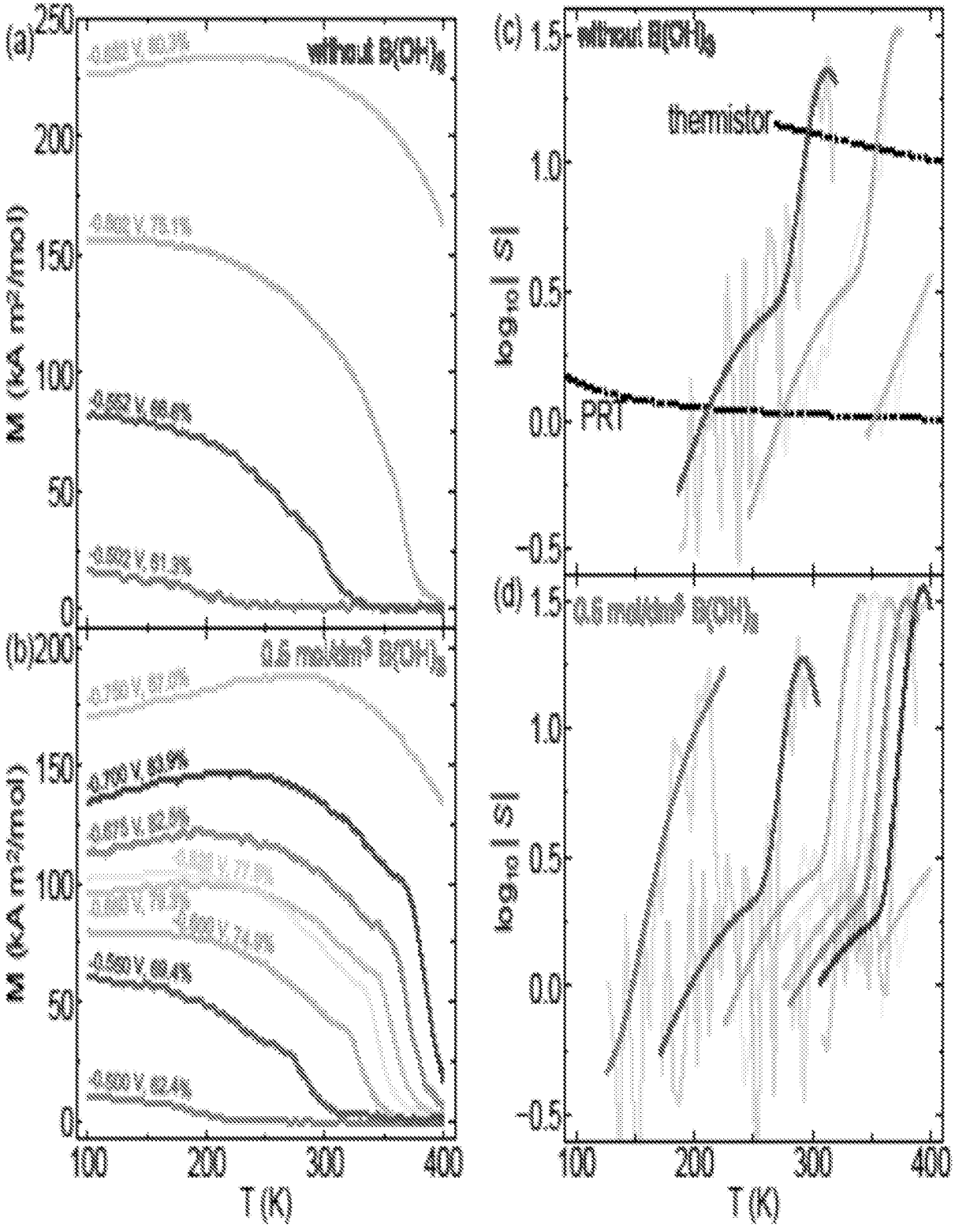
(a)
without B(OH)3
M (kA m2/mol)
(b)
0.6 mol/dm3 B(OH)3
M (kA m2/mol)
T (K)
(c)
without B(OH)3
thermistor
PRT
log10 I (S)
(d)
0.6 mol/dm3 B(OH)3
log10 I (S)
T (K)

FIG. 24

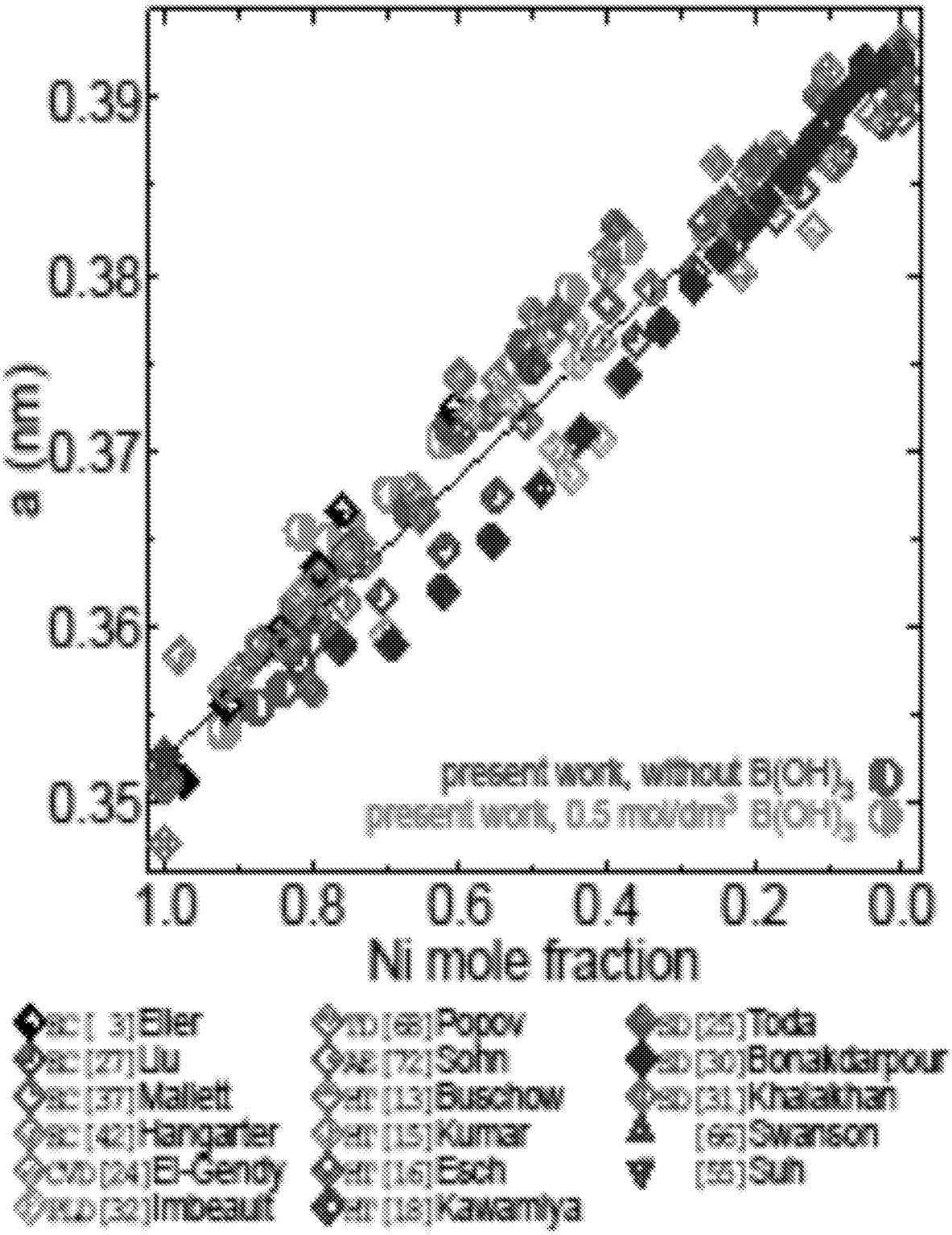
0.39
0.38
0.37
0.36
0.35
a (nm)
present work, without B(OH)3
present work, 0.5 molal B(OH)3
1.0
0.8
0.6
0.4
0.2
0.0
Ni mole fraction
[3]Eler
[27]Liu
[33]Mallett
[42]Hangarter
[24]El-Gendy
[32]Imbeault
[6]Popov
[72]Sohn
[13]Buschow
[15]Kumar
[16]Esch
[18]Kavanmya
[25]Toda
[30]Bonakdarpour
[31]Khataikhan
[66]Swanson
[58]Sun

FIG. 25

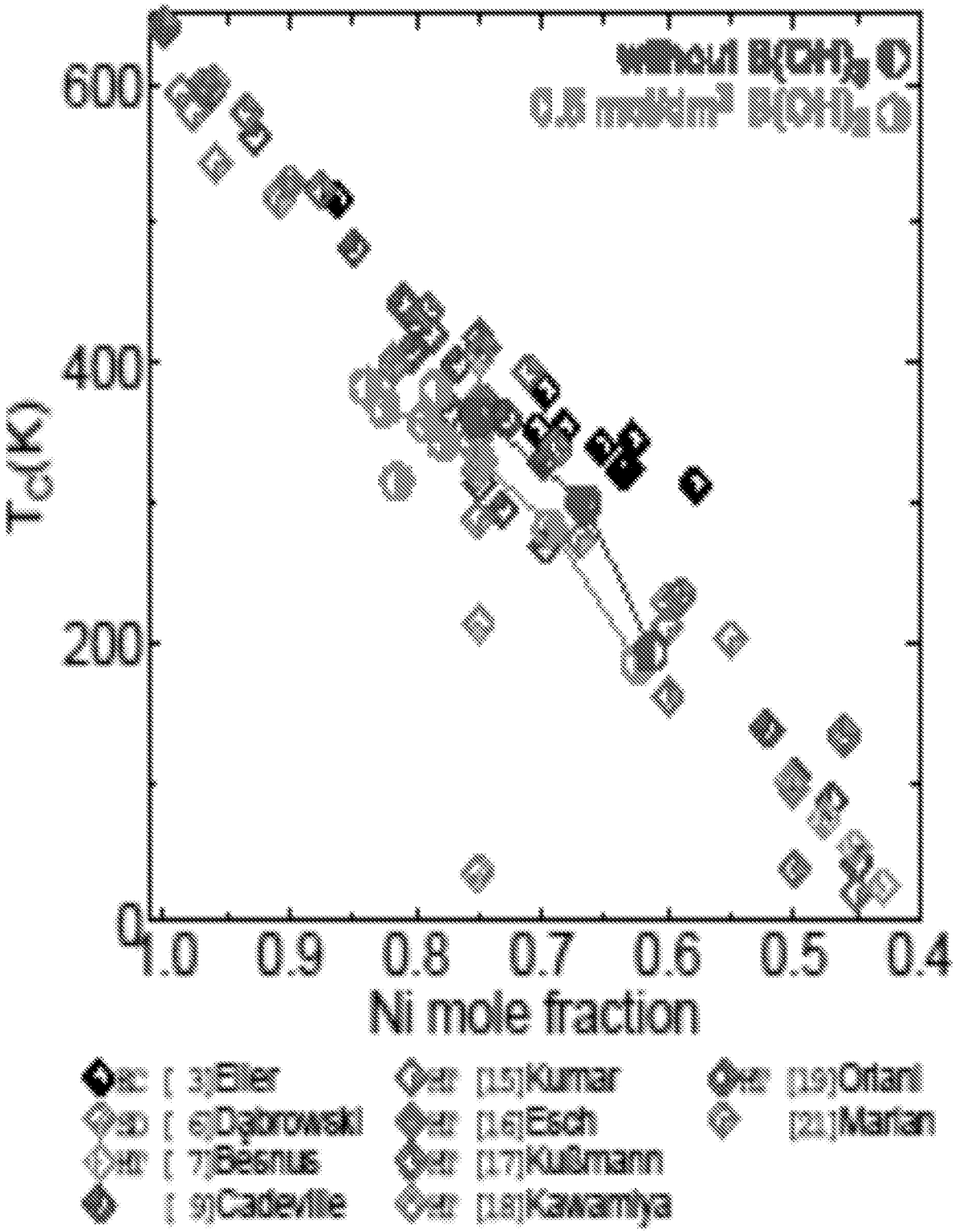
without B(OH)3
0.8 mol% B(OH)3
600
400
200
0
Td(K)
1.0
0.9
0.8
0.7
0.6
0.5
0.4
Ni mole fraction
[3]Eller
[6]Dąbrowski
[7]Besnus
[9]Cadeville
[15]Kumar
[16]Esch
[17]Küßmann
[18]Kamatya
[19]Ortani
[23]Marian

FIG. 26

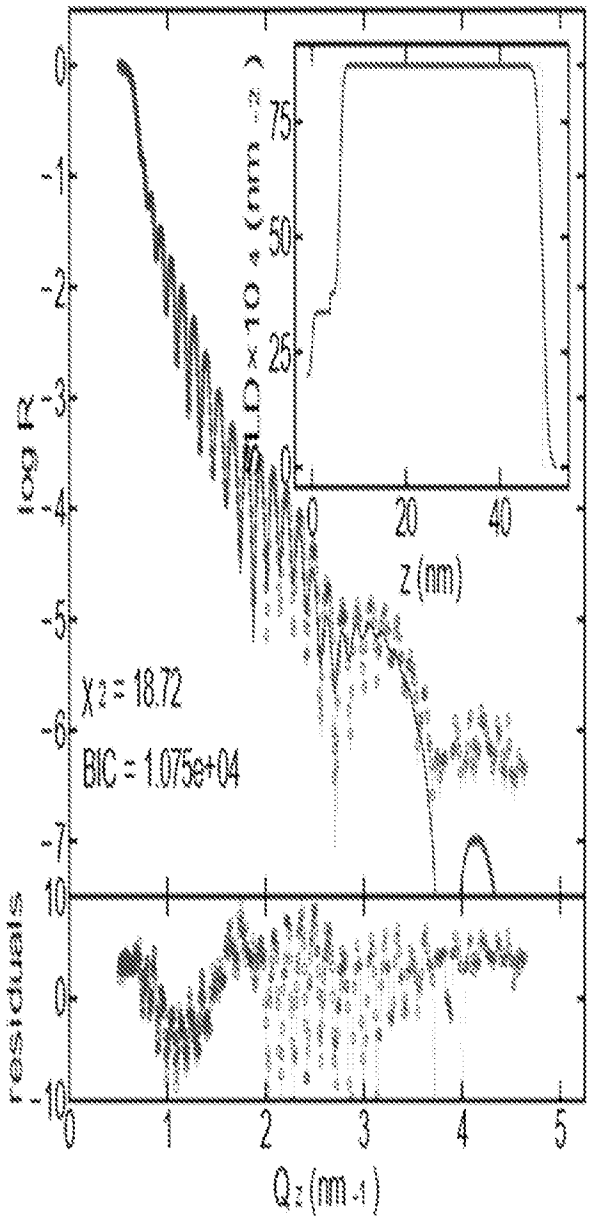

Best fit parameter values and confidence intervals.

name	best	68%	68%	95%	95%
Backgr	-7.084E-08	-7.402E-08	-6.441E-08	-8.198E-08	-5.941E-08
Inten	1.1678	1.1652	1.1698	1.1645	1.1714
Th_Off	-0.0077373	-0.0082976	-0.0075698	-0.0086596	-0.0071616
Si_Int	3.2407	3.1733	3.352	3.0906	3.4254
L02_SLD	33.599	33.467	33.772	33.357	33.921
L02_T	37.811	37.735	37.925	37.617	38.043
L03_SLD	37.652	37.529	37.78	37.428	37.916
L03_T	21.87	21.765	21.95	21.66	22.064
L04_SLD	87.296	87.052	87.372	86.903	87.541
L04_T	432	431.95	432.15	431.85	432.24
L02_Intf	0.0023825	0.0020761	0.011518	0.0003302	0.016157
L03_Intf	0.23711	0.23657	0.23685	0.2343	0.23926
L04_Intf	0.021935	0.021911	0.021946	0.021893	0.021965

FIG. 27

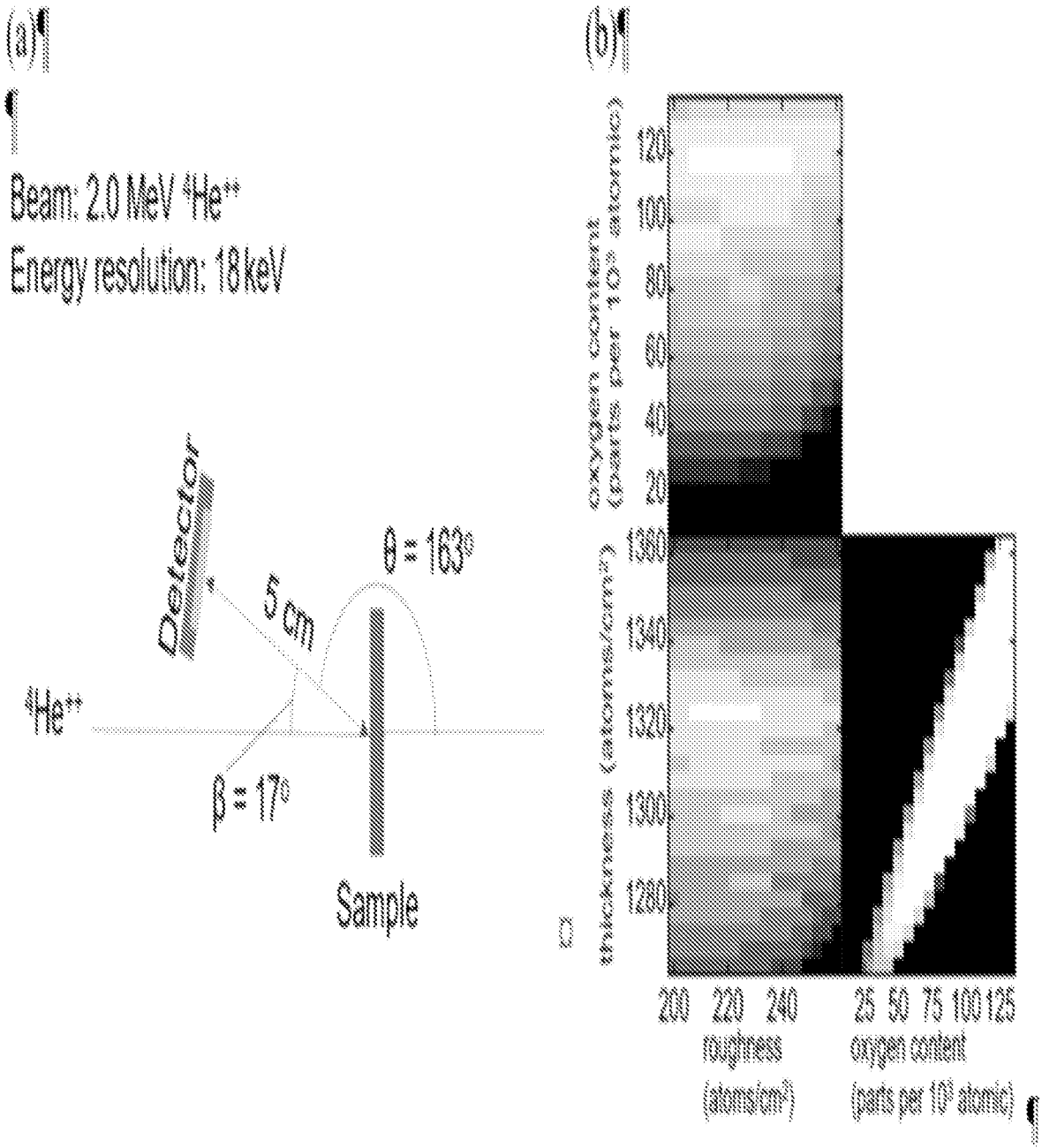
(a)
Beam: 2.0 MeV $^4He^{++}$
Energy resolution: 18 keV
Detector
5 cm
θ = 163°
$^4He^{++}$
β = 17°
Sample
(b)
oxygen content (counts per 10^5 atomic)
thickness (atoms/cm²)
120
100
80
60
40
20
1360
1340
1320
1300
1280
200 220 240
roughness (atoms/cm²)
25 50 75 100 125
oxygen content (parts per 10^5 atomic)

FIG. 28

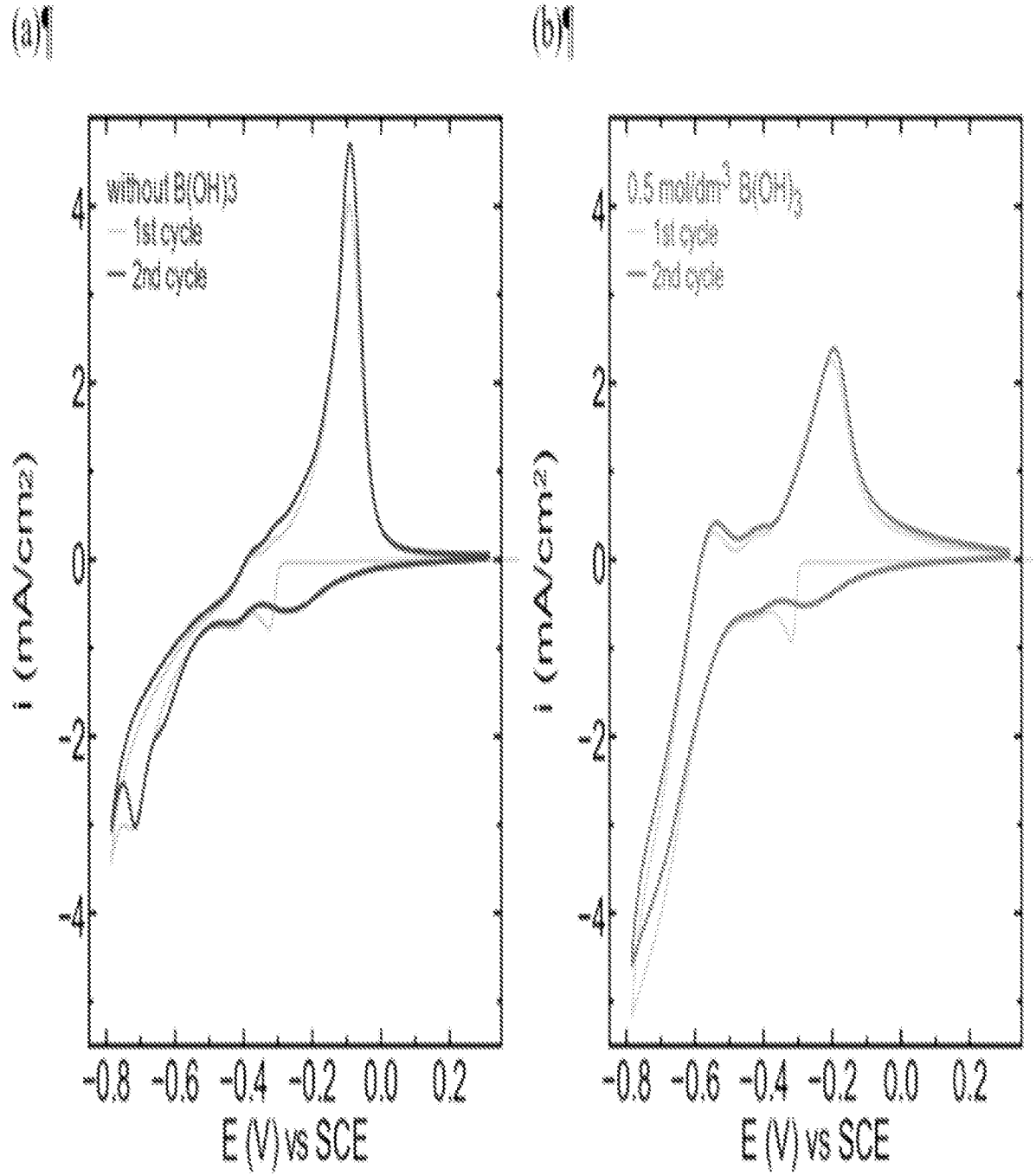
(a)
without B(OH)3
1st cycle
2nd cycle
i (mA/cm2)
E (V) vs SCE
(b)
0.5 mol/dm3 B(OH)3
1st cycle
2nd cycle
i (mA/cm2)
E (V) vs SCE

FIG. 29

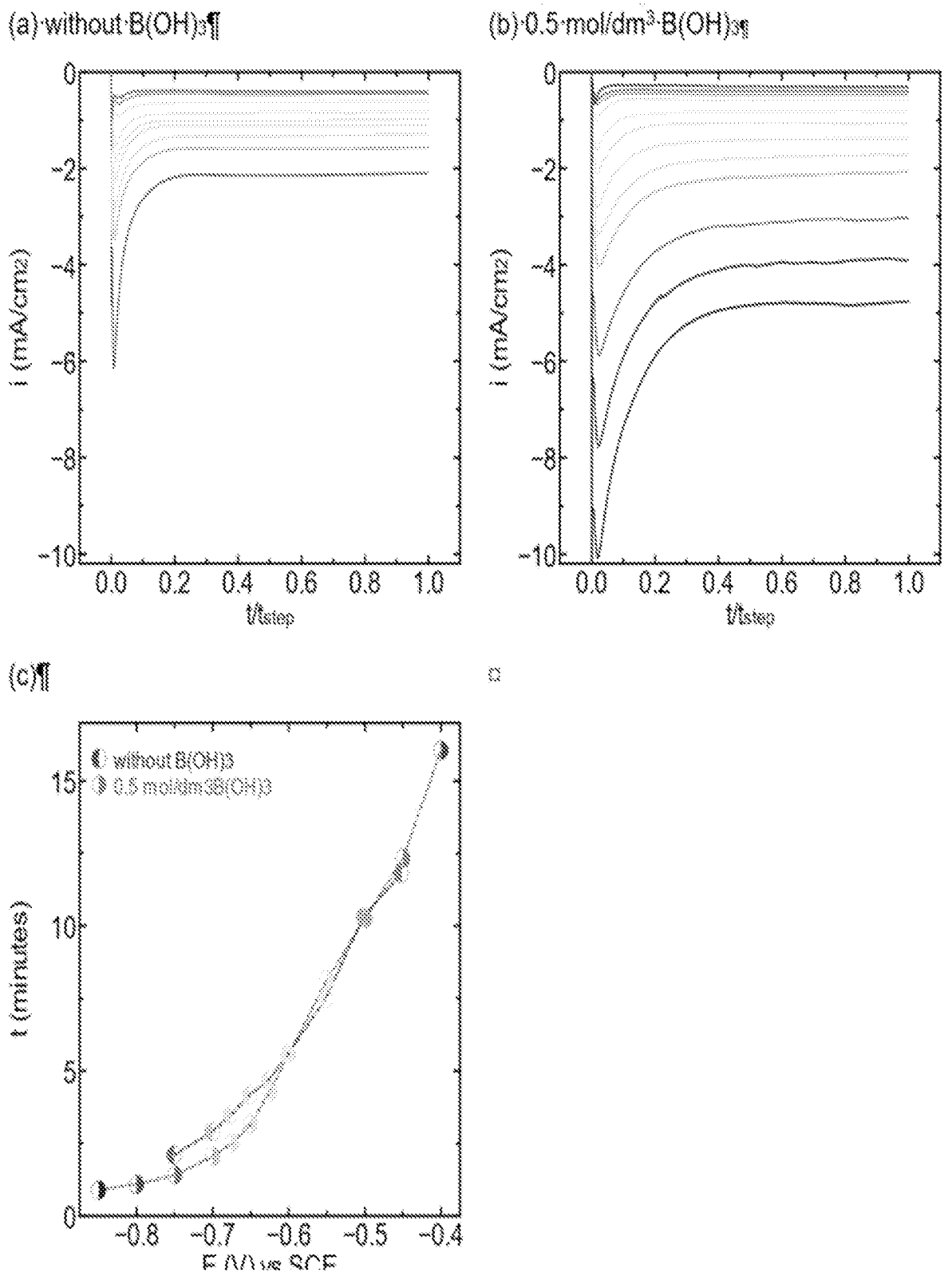
(a) without B(OH)3
(b) 0.5 mol/dm3 B(OH)3
(c)
i (mA/cm2)
t/tstep
t (minutes)
without B(OH)3
0.5 mol/dm3B(OH)3
E (V) vs SCE

FIG. 30

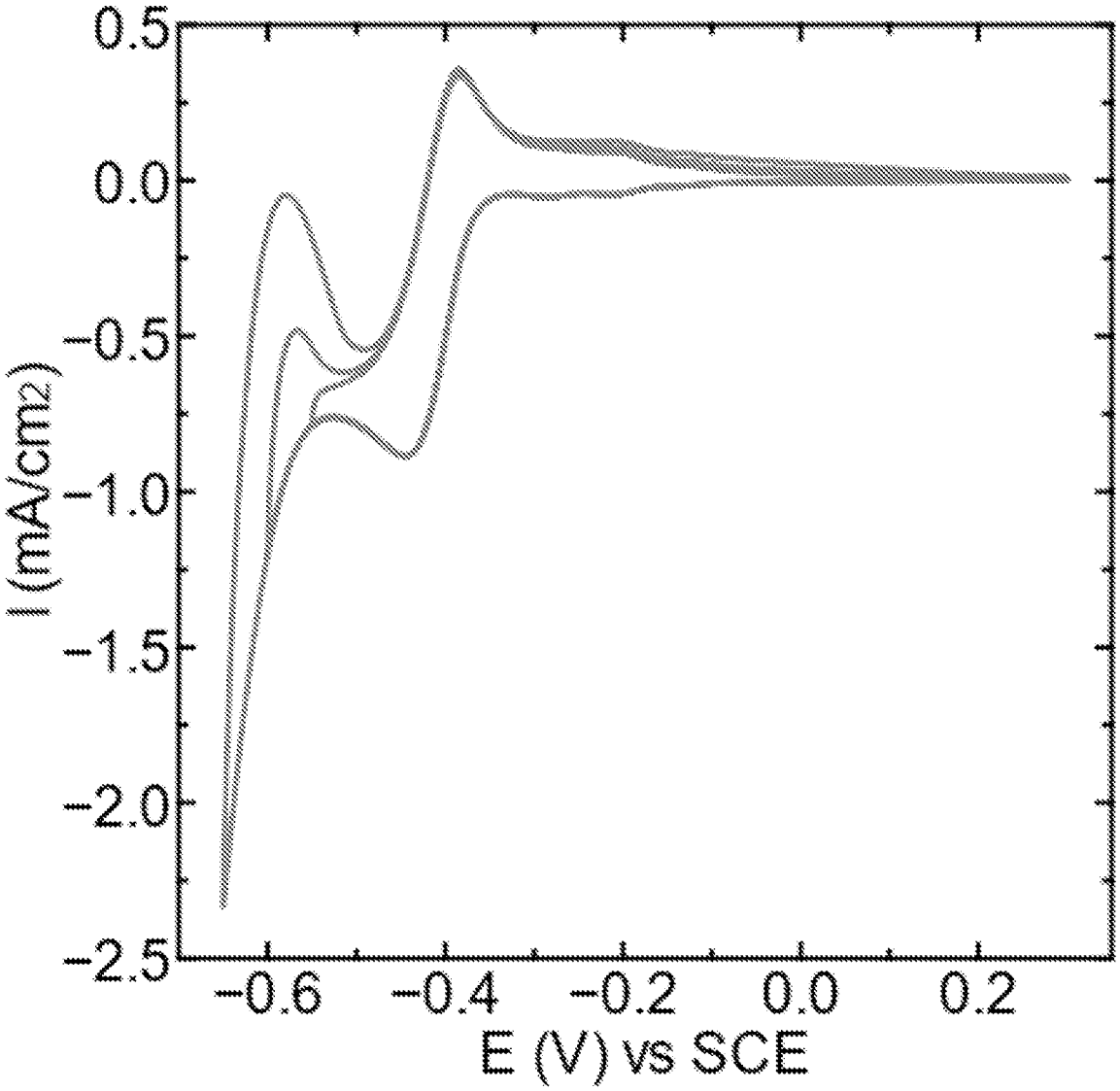

FIG. 31

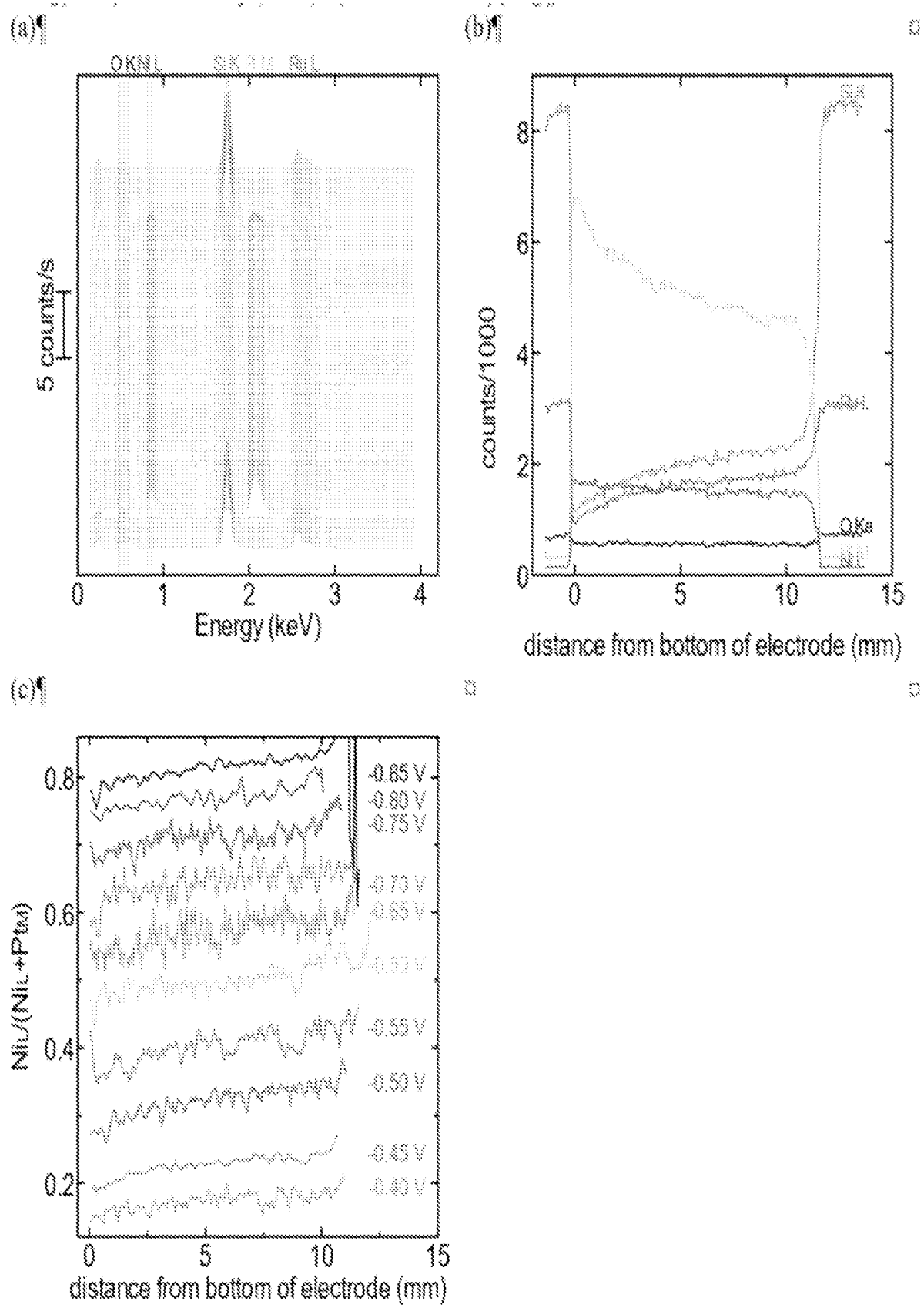
(a)
OKNL
5 counts/s
0
1
2
3
4
Energy (keV)
(b)
counts/1000
0
2
4
6
8
0
5
10
15
distance from bottom of electrode (mm)
(c)
NiL/(NiL+PtM)
0.2
0.4
0.6
0.8
-0.85 V
-0.80 V
-0.75 V
-0.70 V
-0.65 V
-0.60 V
-0.55 V
-0.50 V
-0.45 V
-0.40 V
0
5
10
15
distance from bottom of electrode (mm)

FIG. 32

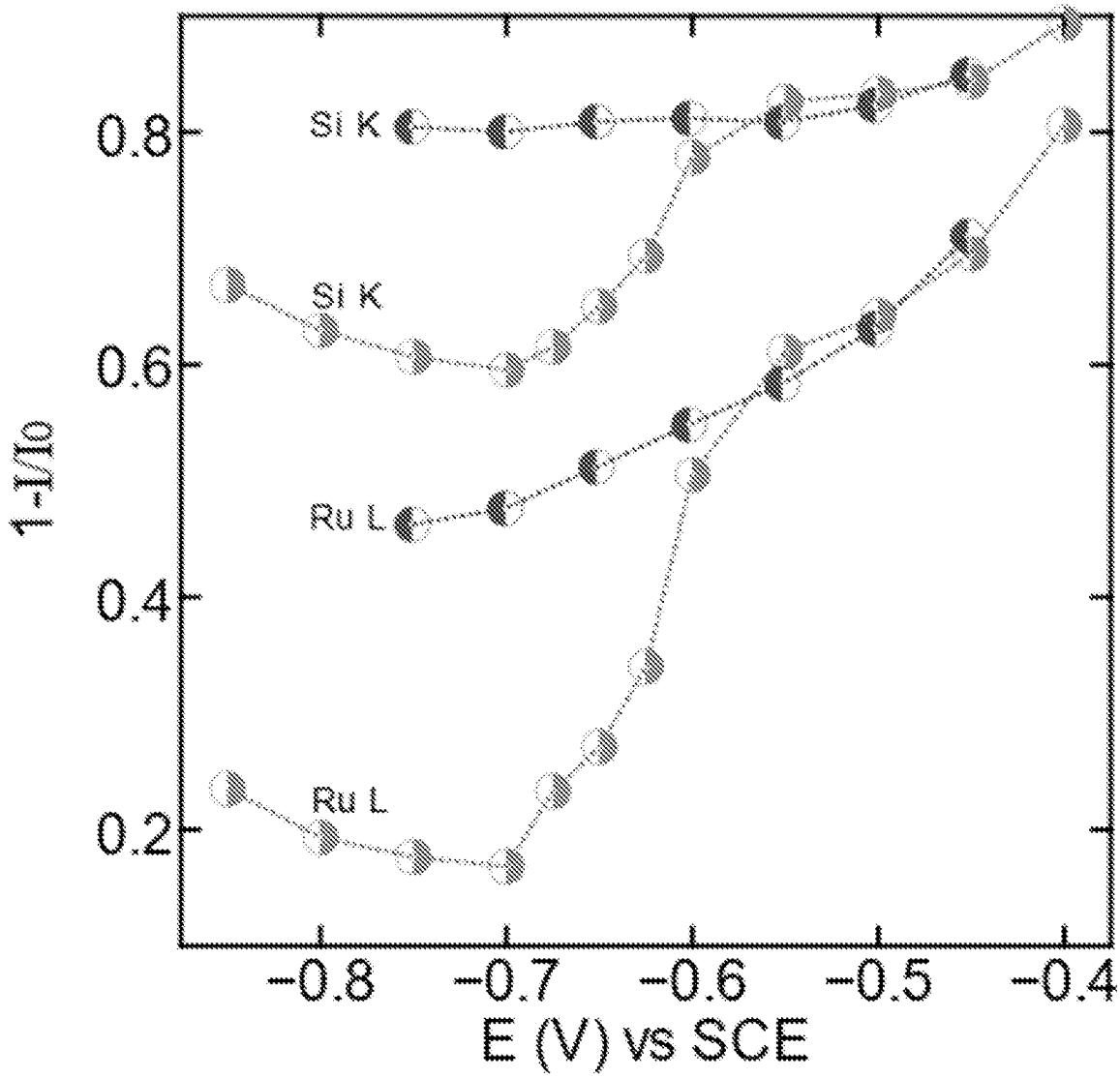

FIG. 33

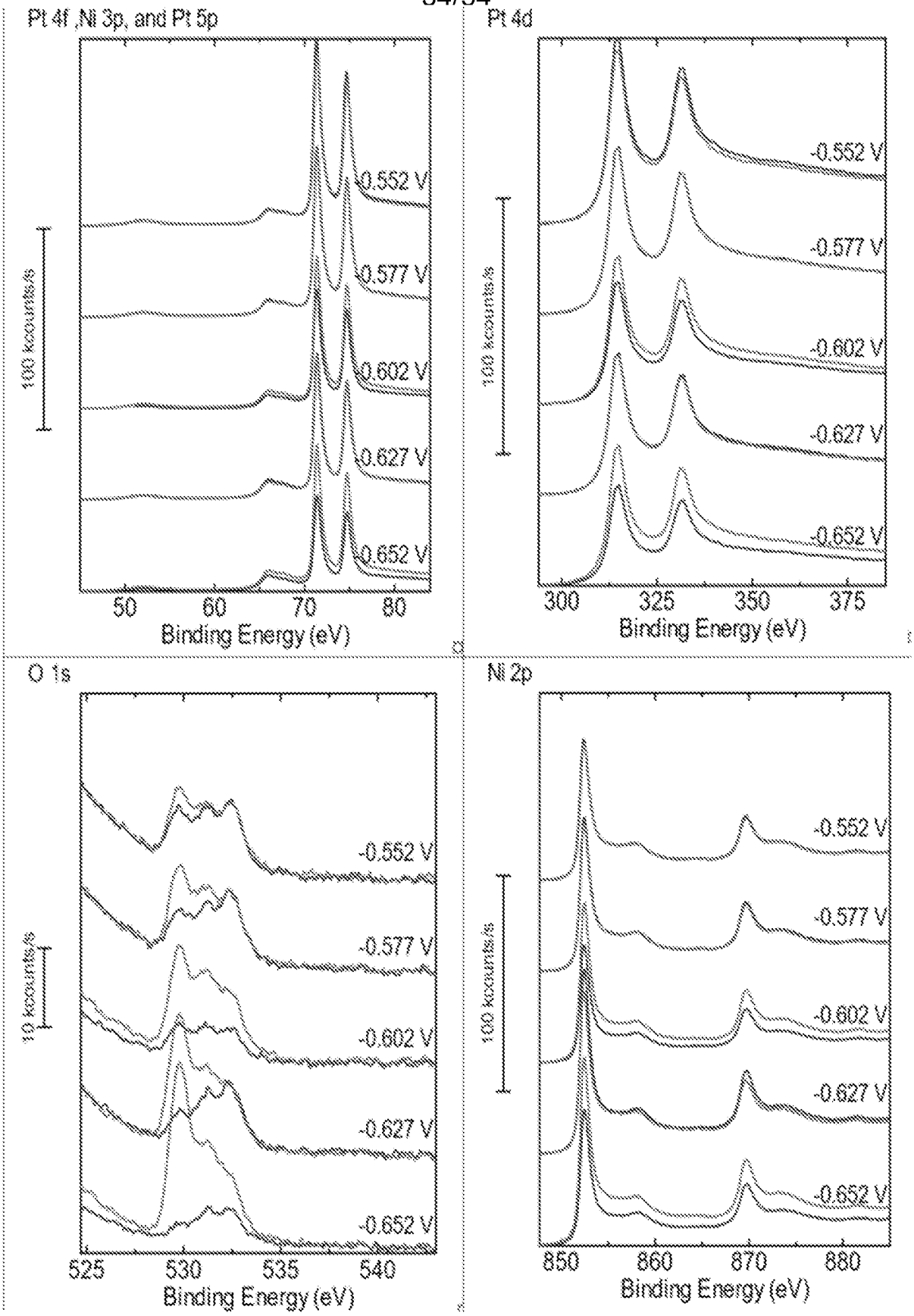
Pt 4f ,Ni 3p, and Pt 5p
-0.552 V
-0.577 V
-0.602 V
-0.627 V
-0.652 V
100 kcounts/s
50
60
70
80
Binding Energy (eV)
Pt 4d
-0.552 V
-0.577 V
-0.602 V
-0.627 V
-0.652 V
100 kcounts/s
300
325
350
375
Binding Energy (eV)
O 1s
-0.552 V
-0.577 V
-0.602 V
-0.627 V
-0.652 V
10 kcounts/s
525
530
535
540
Binding Energy (eV)
Ni 2p
-0.552 V
-0.577 V
-0.602 V
-0.627 V
-0.652 V
100 kcounts/s
850
860
870
880
Binding Energy (eV)

FIG. 34

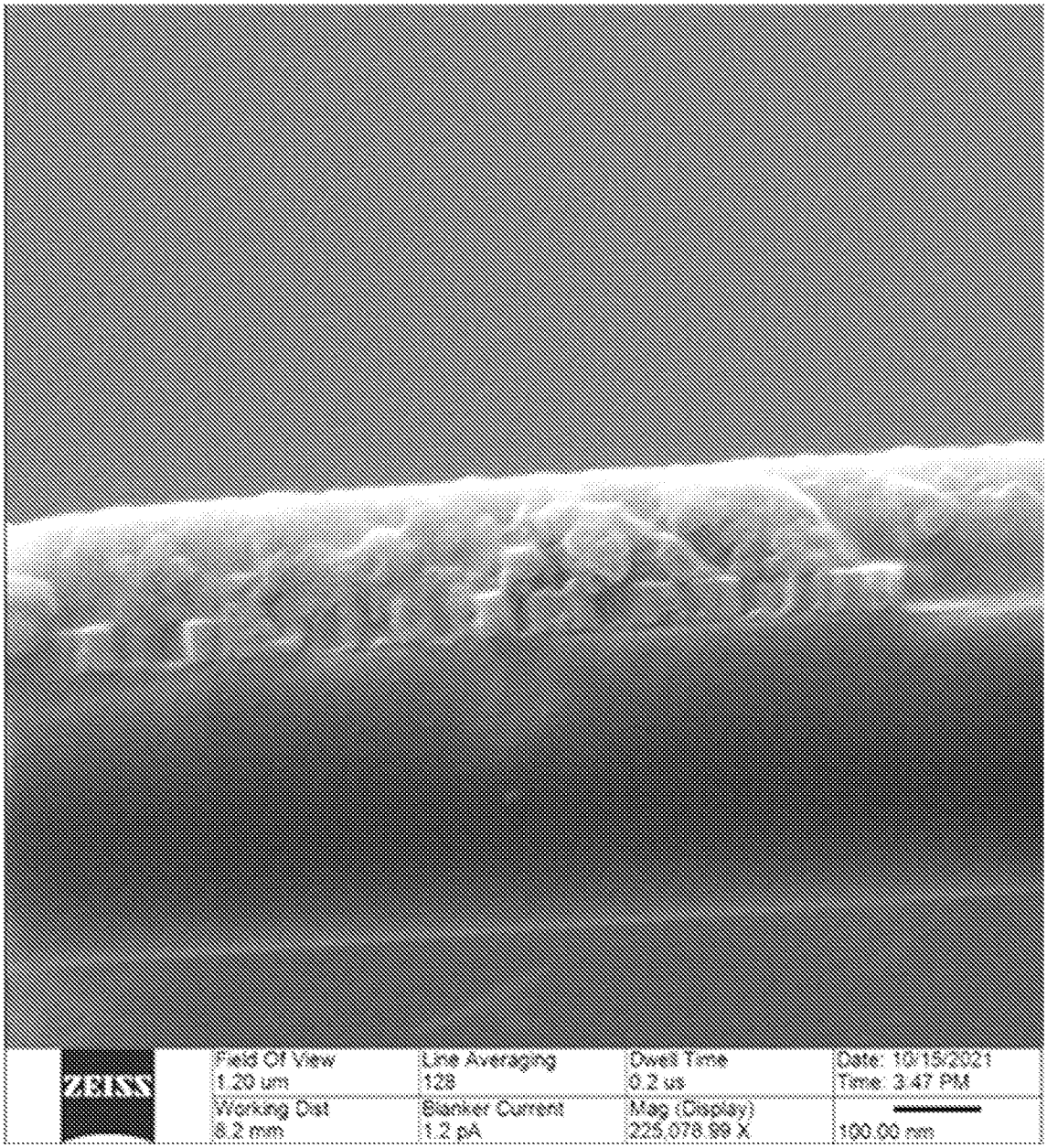
ZEISS
Field Of View
1.20 um
Line Averaging
128
Dwell Time
0.2 us
Date: 10/15/2021
Time: 3:47 PM
Working Dist
8.2 mm
Emitter Current
1.2 pA
Mag (Display)
225,078.59 X
100.00 nm

FIG. 35

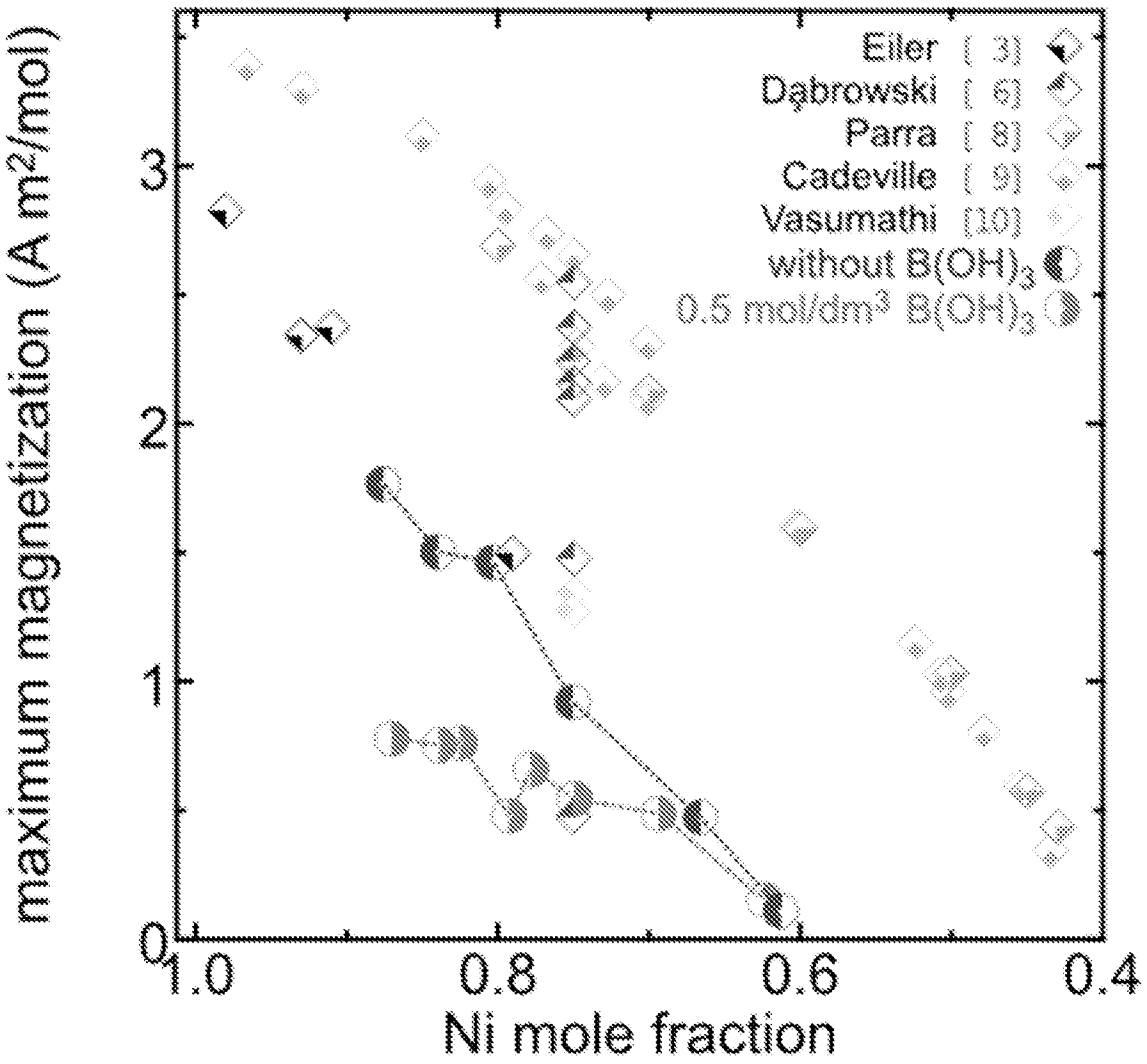
maximum magnetization (A m²/mol)
Ni mole fraction
1.0
0.8
0.6
0.4
0
1
2
3
Eiler [3]
Dąbrowski [6]
Parra [8]
Cadeville [9]
Vasumathi [10]
without B(OH)3
0.5 mol/dm3 B(OH)3

FIG. 36

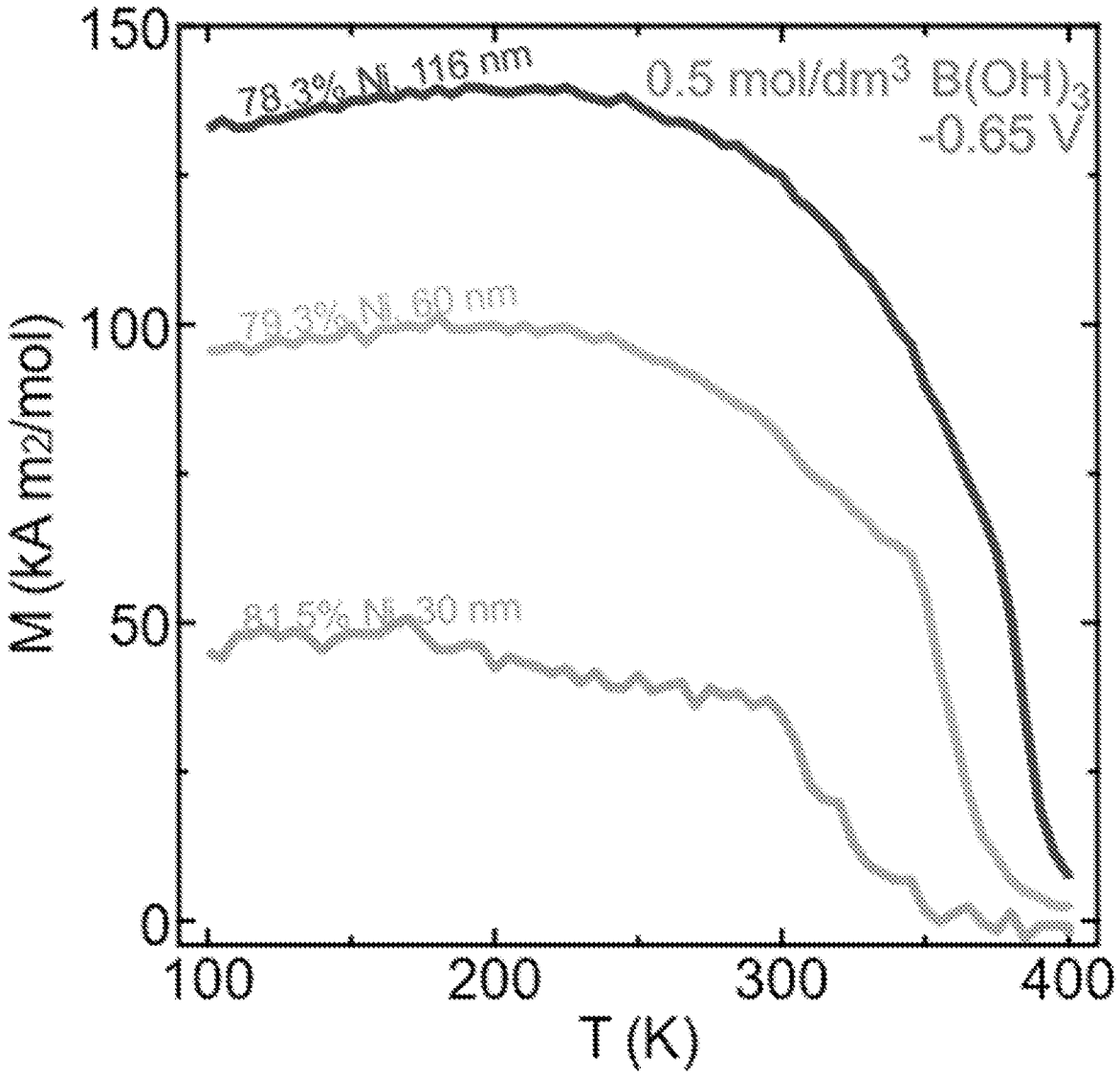
150
100
50
0
M (kA m2/mol)
78.3% Ni, 116 nm
79.3% Ni, 60 nm
81.5% Ni, 30 nm
0.5 mol/dm3 B(OH)3
-0.65 V
100
200
300
400
T (K)

FIG. 37

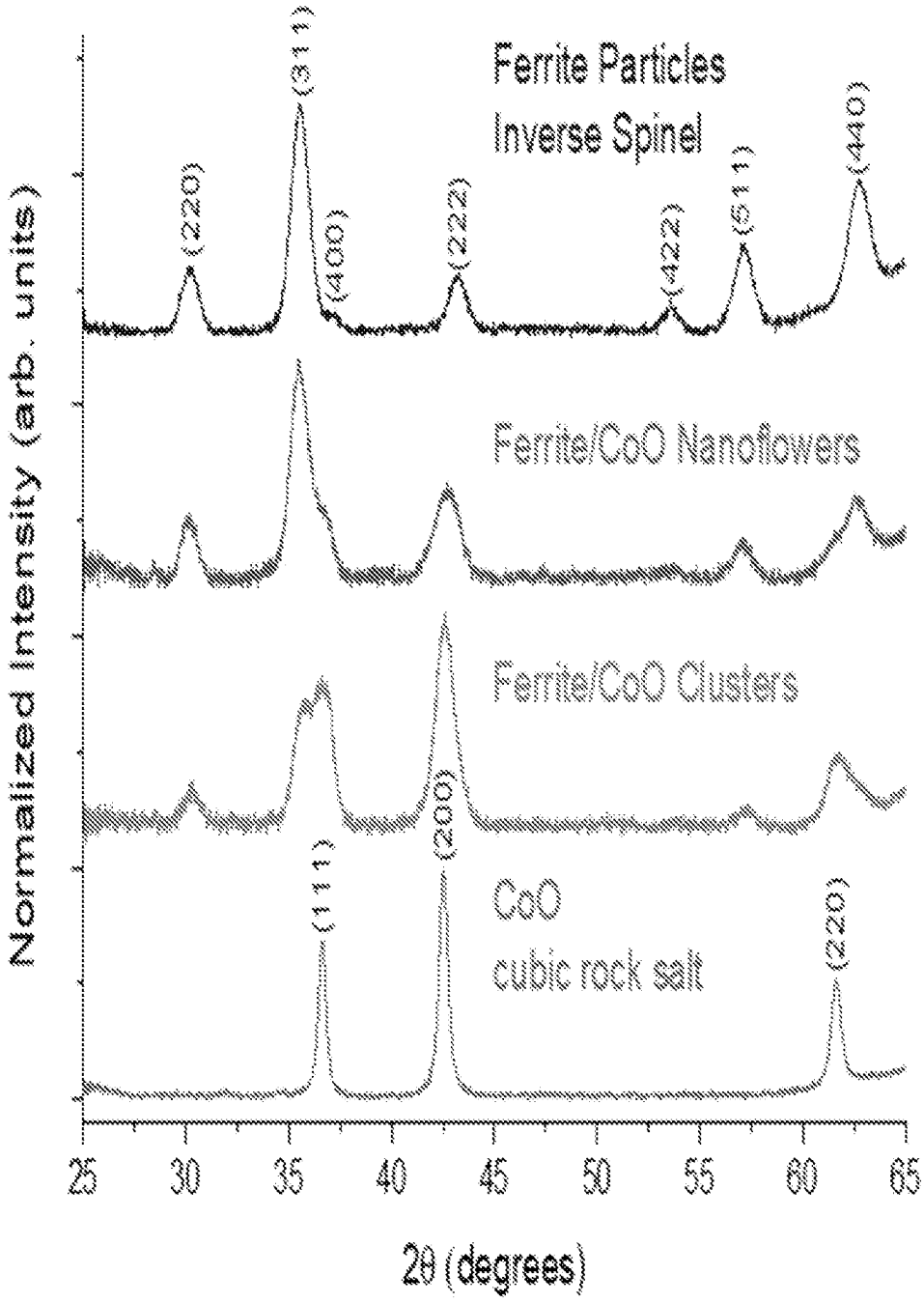
Ferrite Particles
Inverse Spinel
Ferrite/CoO Nanoflowers
Ferrite/CoO Clusters
CoO
cubic rock salt
(220)
(311)
(400)
(222)
(422)
(611)
(440)
(111)
(200)
(220)
Normalized Intensity (arb. units)
25
30
35
40
45
50
55
60
65
2θ (degrees)

FIG. 38

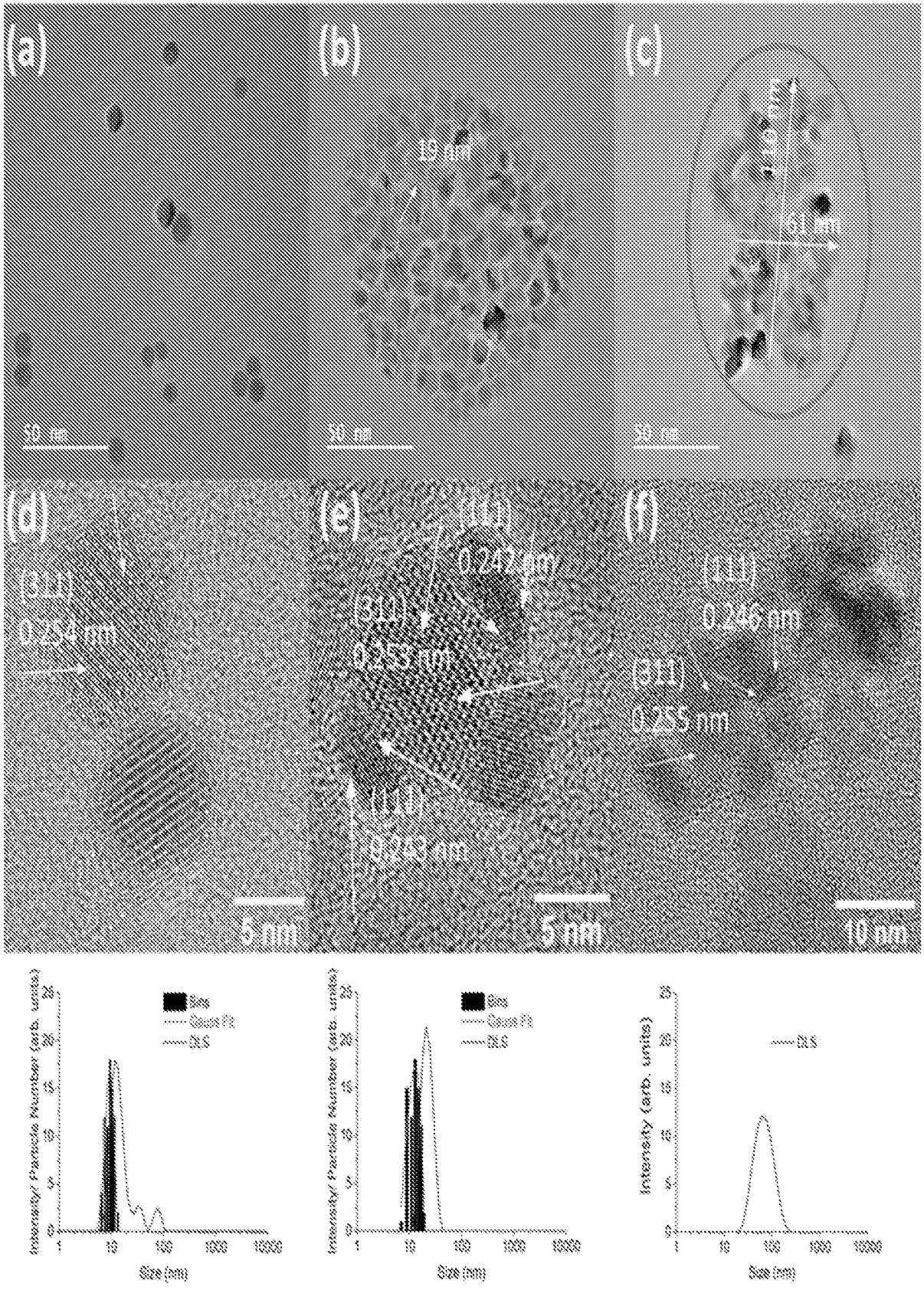
(a)
(b)
(c)
19 nm
61 nm
50 nm
20 nm
50 nm
(d)
(111)
0.234 nm
(e)
(111)
0.242 nm
(200)
0.253 nm
(011)
0.243 nm
(f)
(111)
0.246 nm
(111)
0.255 nm
5 nm
5 nm
10 nm
Data
Gauss Fit
DLS
Intensity/ Particle Number (arb. units)
Size (nm)
Intensity (arb. units)

FIG. 39

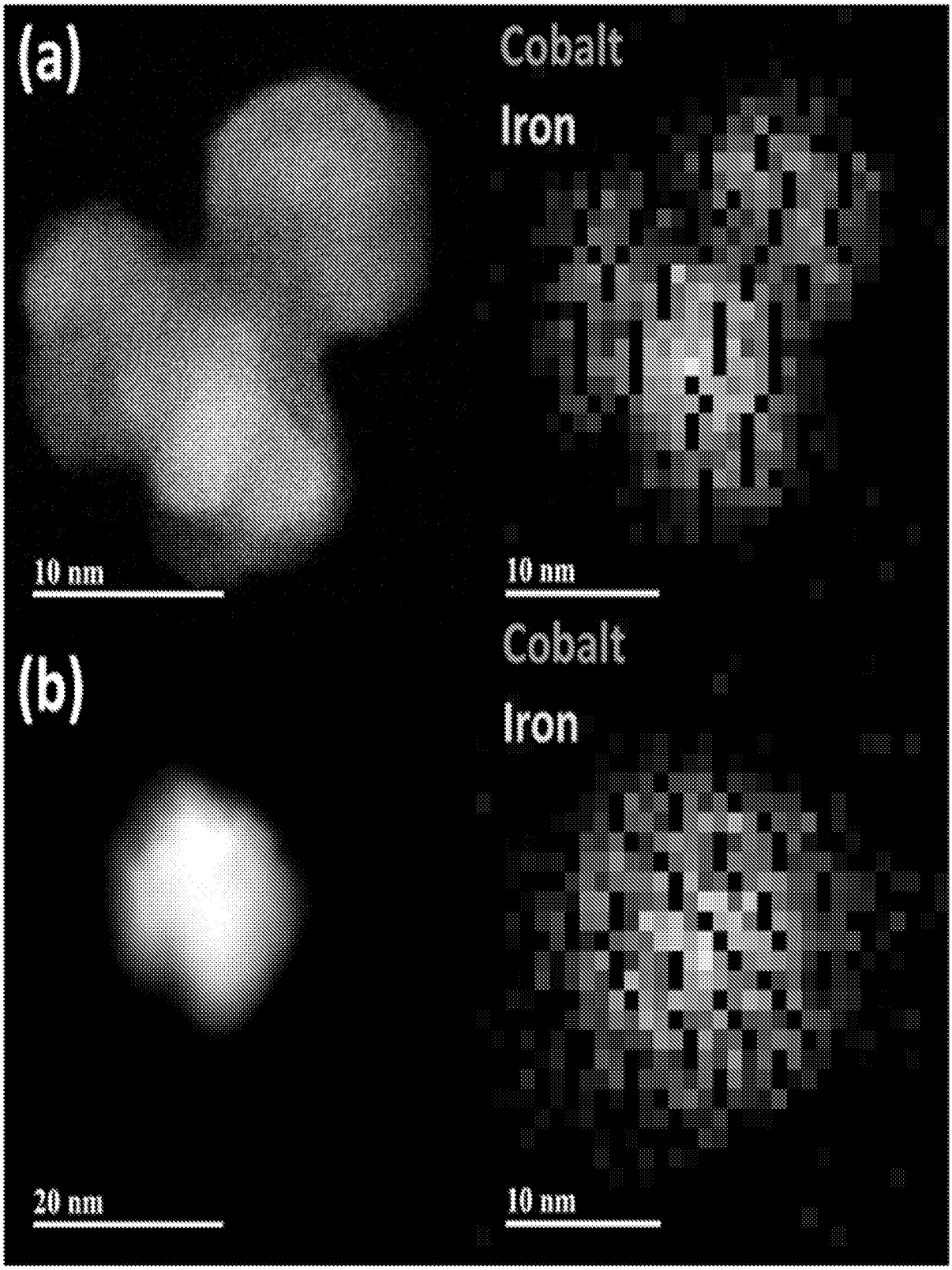

FIG. 40

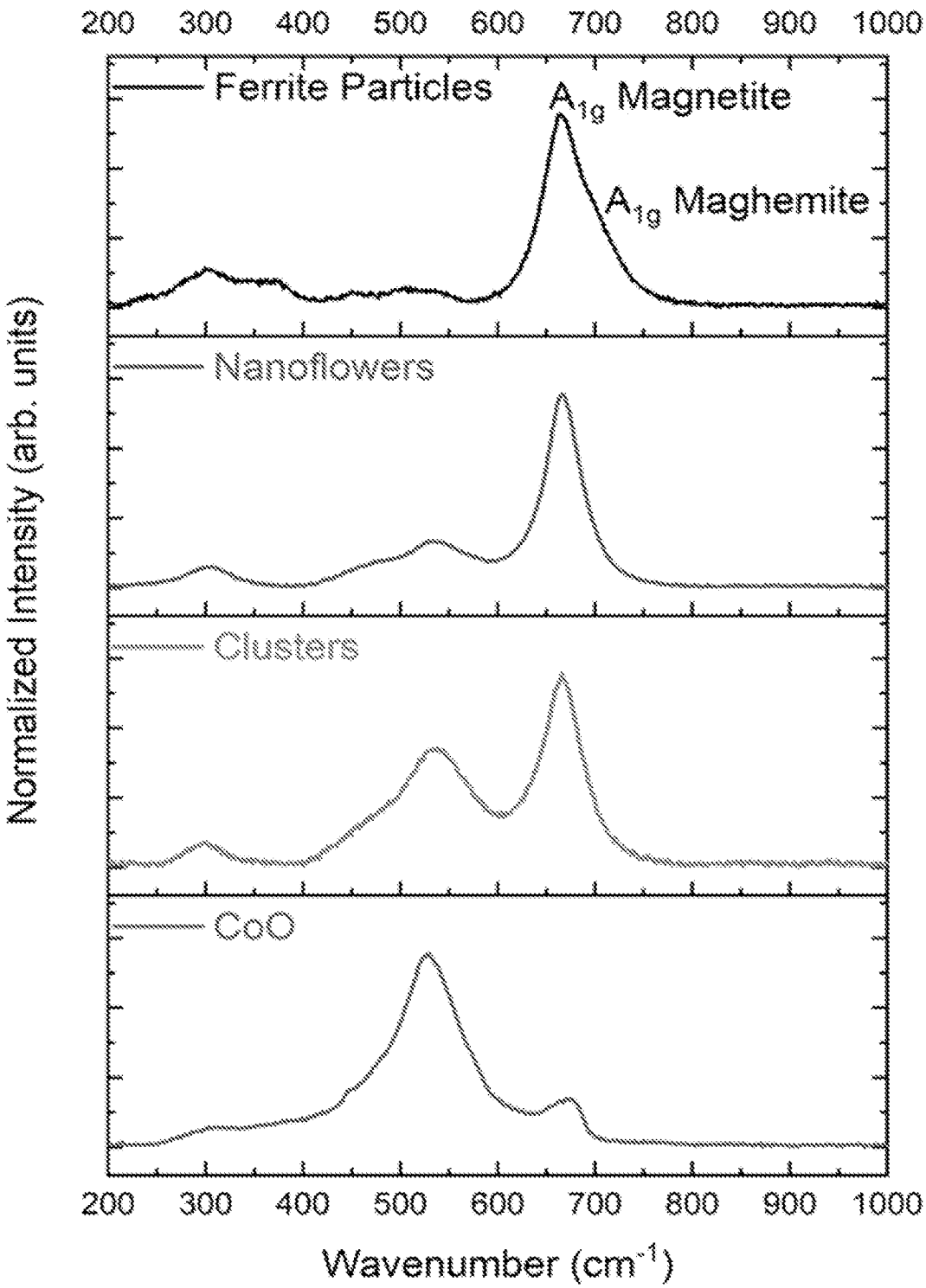
200 300 400 500 600 700 800 900 1000
Ferrite Particles
A_{1g} Magnetite
A_{1g} Maghemite
Nanoflowers
Clusters
CoO
Normalized Intensity (arb. units)
200 300 400 500 600 700 800 900 1000
Wavenumber (cm^{-1})

FIG. 41

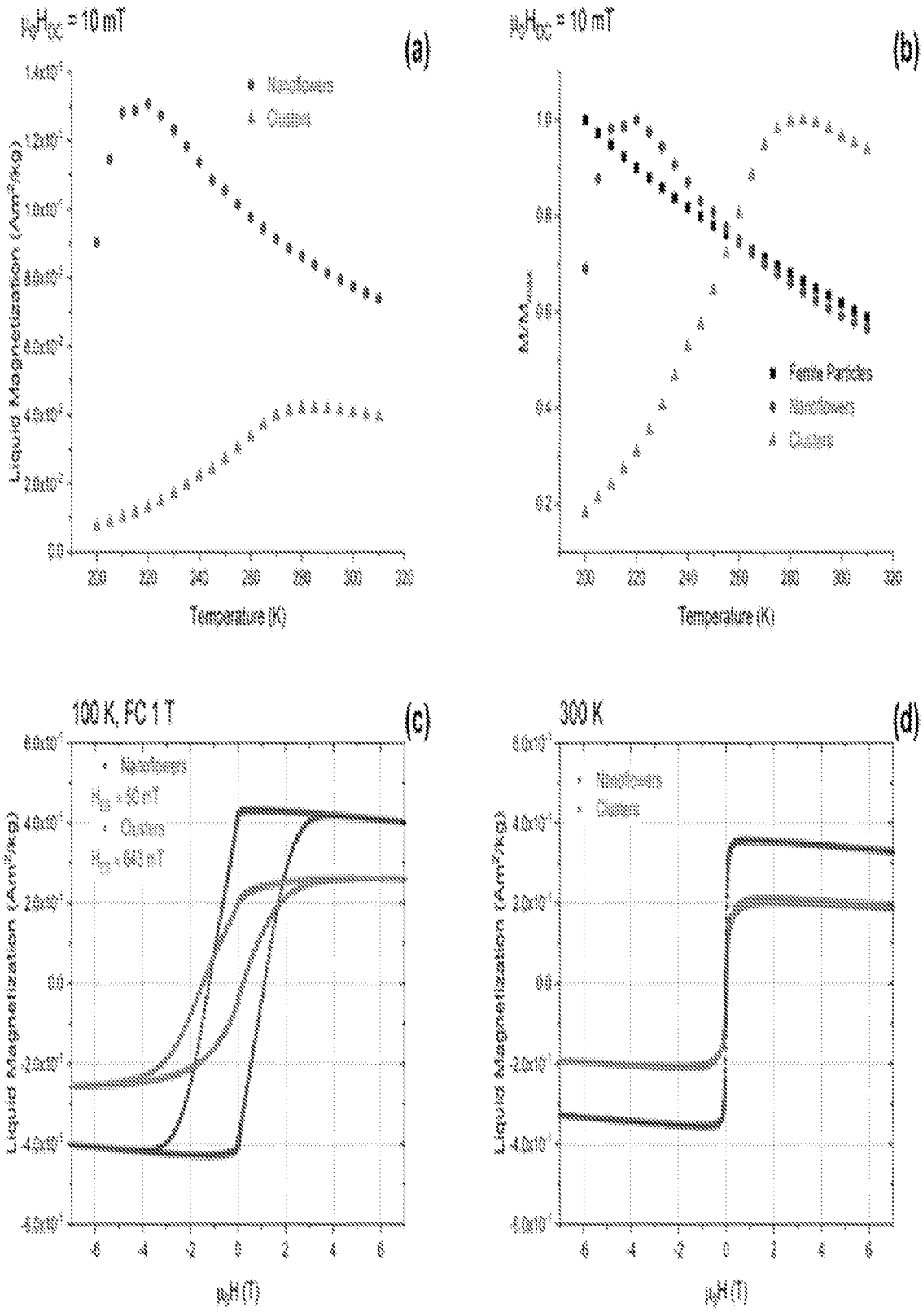
(a)
Nanobowls
Cubes
Temperature (K)
(b)
Ferrite Particles
Nanobowls
Cubes
Temperature (K)
100 K, FC 1 T
(c)
Nanobowls
Cubes
300 K
(d)
Nanobowls
Cubes

FIG. 42

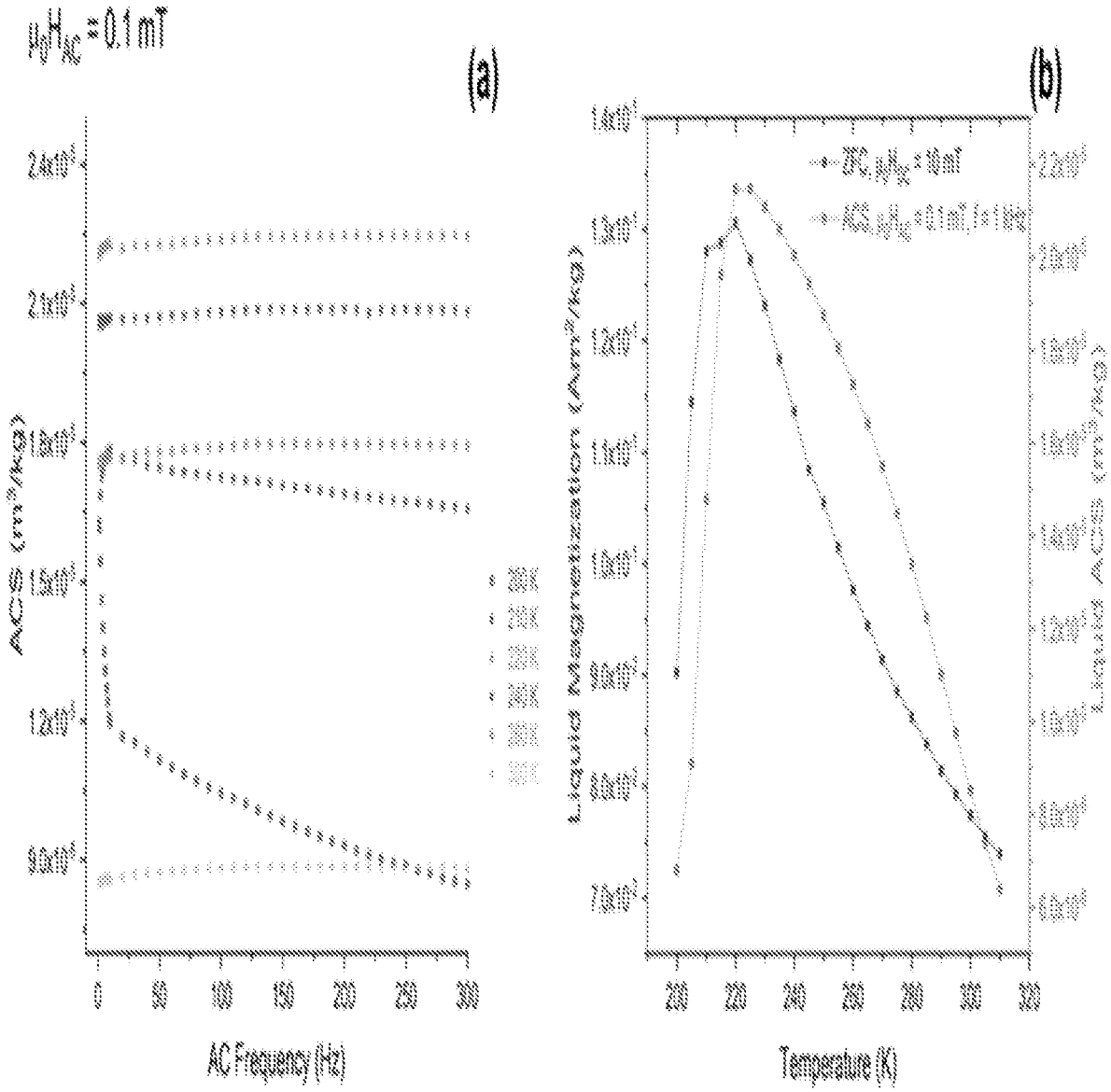
$\mu_0 H_{DC}$ = 0.1 mT
(a)
(b)
AC Frequency (Hz)
Temperature (K)
Liquid Magnetization (Am²/kg)
ZFC, $\mu_0 H_{DC}$ = 0 mT
FC, $\mu_0 H_{DC}$ = 0.1 mT, f = 1 Hz

FIG. 43

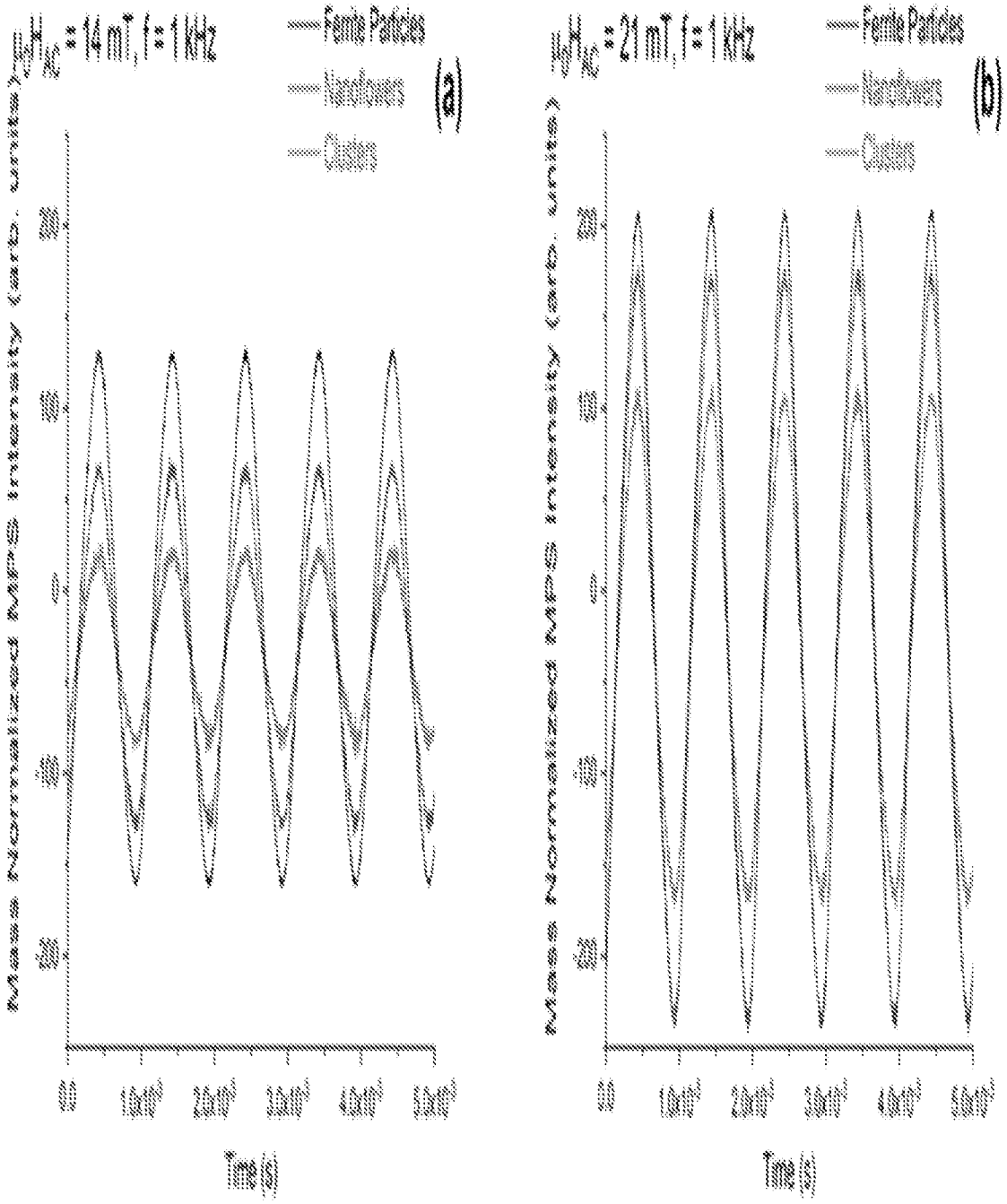
$\mu_0 H_{AC}$ = 14 mT, f = 1 kHz
Ferrite Particles
Nanowires
Clusters
(a)
Mass Normalized MPS Intensity (arb. units)
Time (s)
$\mu_0 H_{AC}$ = 21 mT, f = 1 kHz
Ferrite Particles
Nanowires
Clusters
(b)
Mass Normalized MPS Intensity (arb. units)
Time (s)

FIG. 44

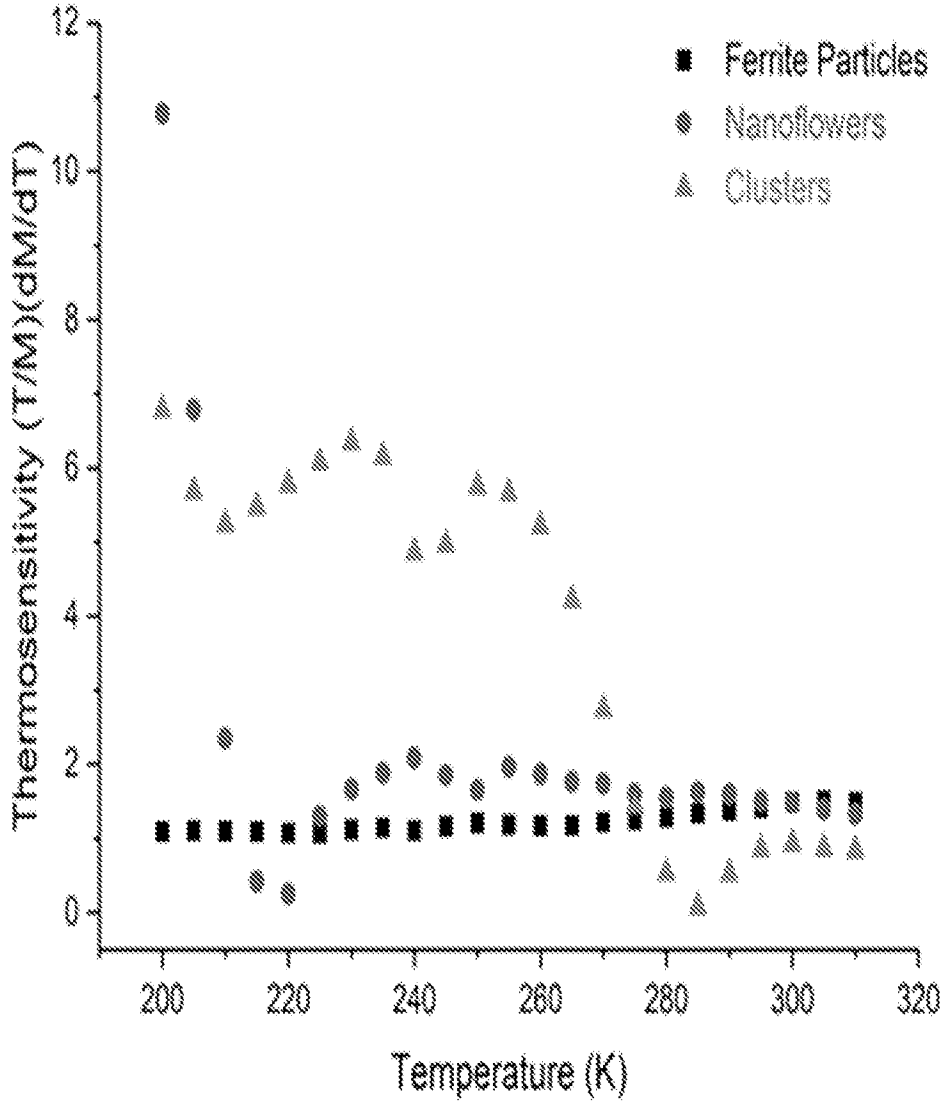
Ferrite Particles
Nanoflowers
Clusters
Thermosensitivity (T/M)(dM/dT)
0
2
4
6
8
10
12
200
220
240
260
280
300
320
Temperature (K)

FIG. 45

MNC Morphology	Ferrite Seed Quantity (mg)	Precursor Quantity (mmol)	Precursors	DLS Size (nm)	TEM Size (nm)
Ferrite Particles	N/A	2	$Fe(acac)_3$	12 (main peak)	10
Clusters	32	1	$Co(acac)_3$	74, 68	N/A
Nanoflowers	48	0.75	$Co(acac)_3$	22, 24	13
Clusters (S1)	48	0.75	$Co(acac)_3$ $Ni(acac)_2$	not stable	N/A
Clusters (S2)	32	1	$Co(acac)_3$ $Ni(acac)_2$	not stable	N/A
Clusters (S3)	32	1.75	$Co(acac)_3$ $Ni(acac)_2$	127 (main peak), 120	N/A
Clusters (S4)	16	1.75	$Co(acac)_3$ $Ni(acac)_2$	not stable	N/A

FIG. 46

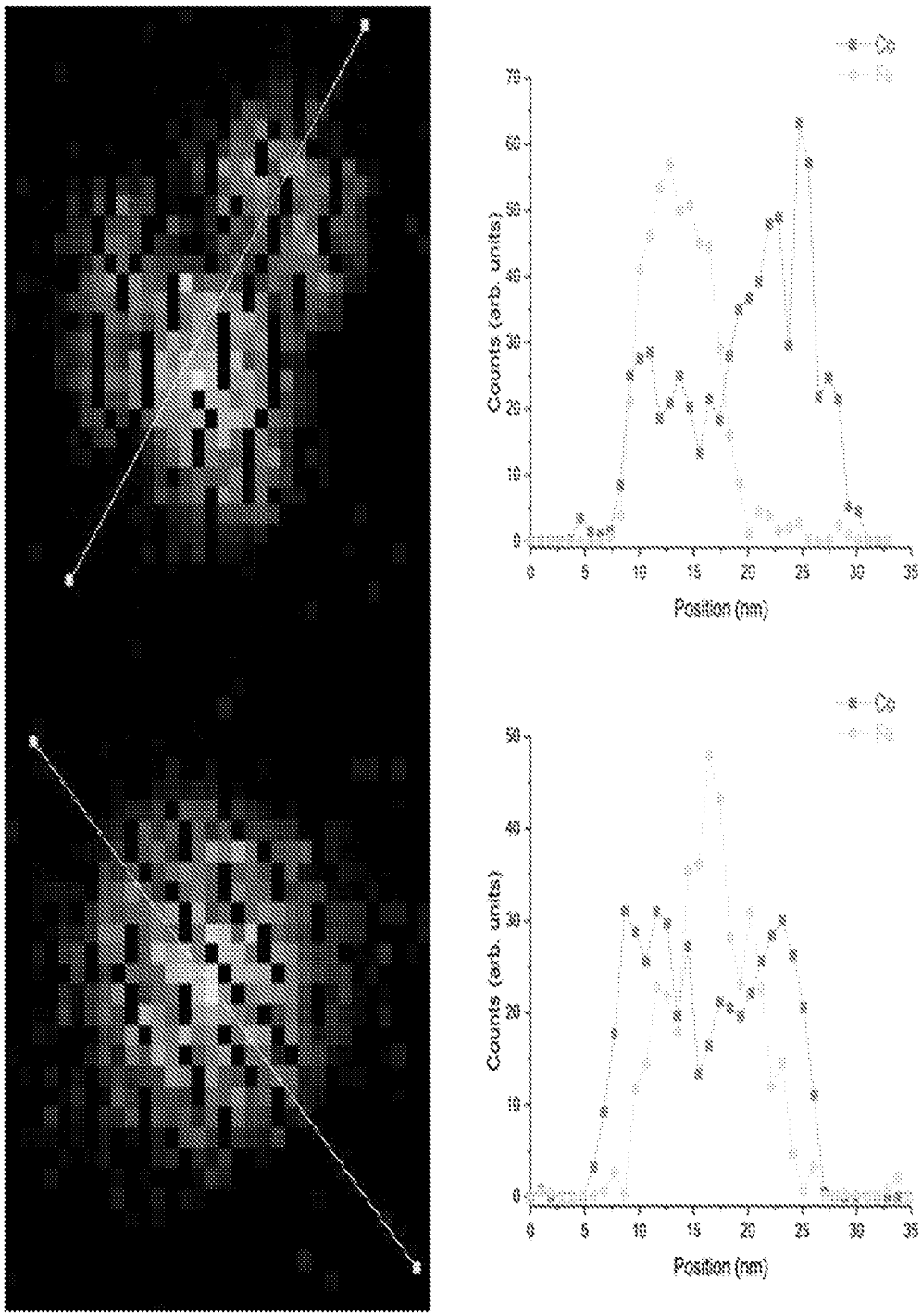

FIG. 47

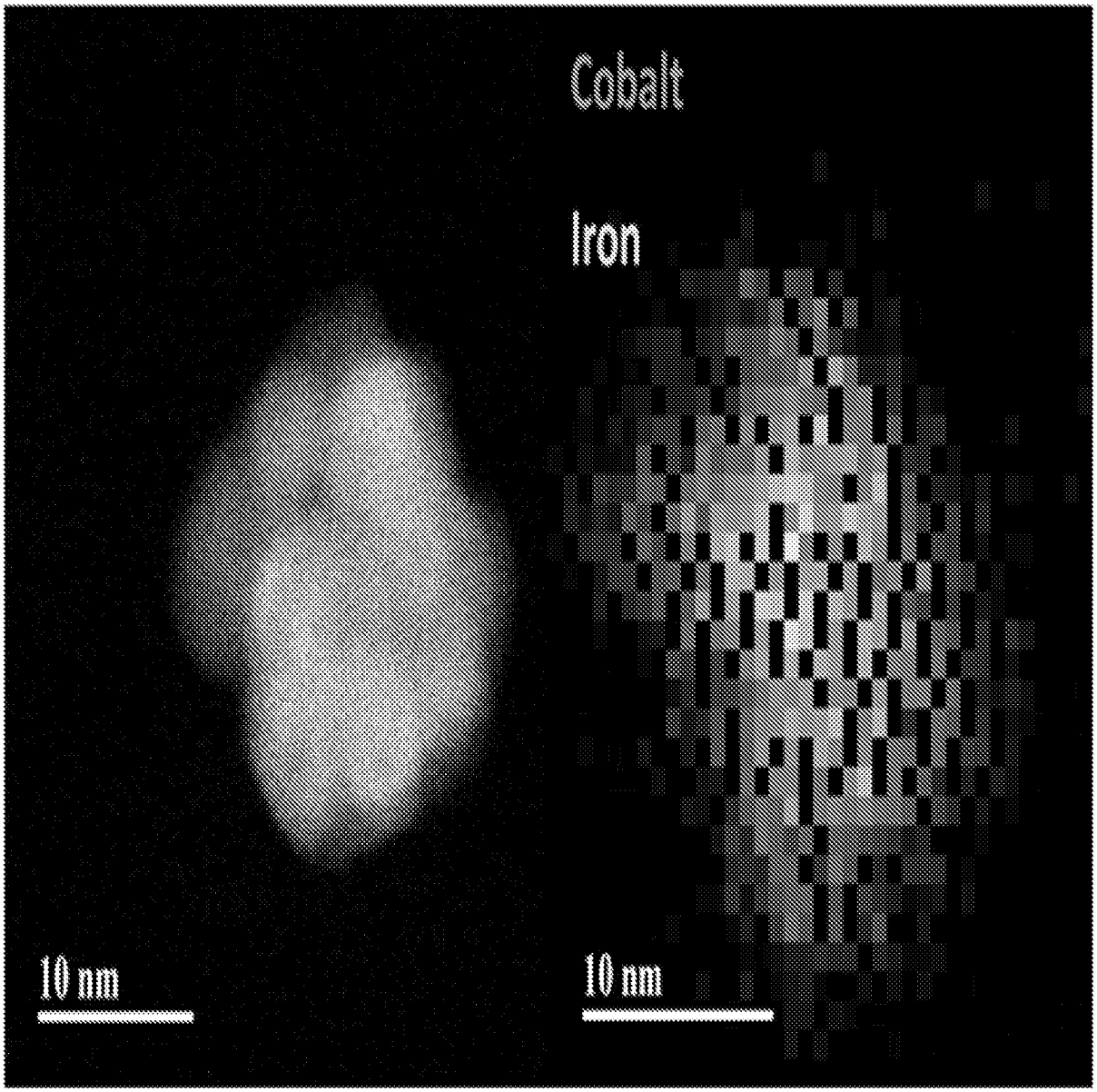

FIG. 48

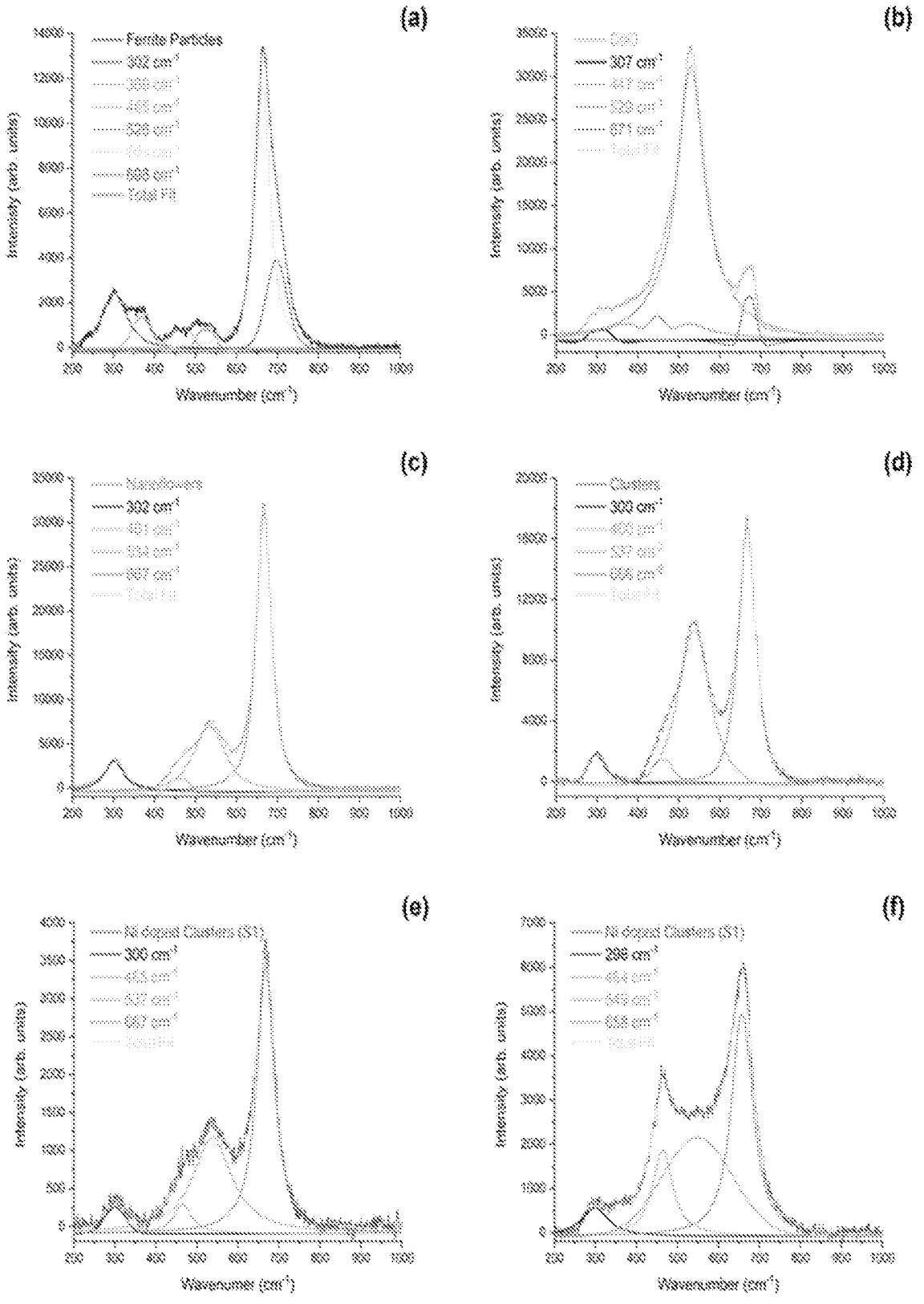
(a)
Ferrite Particles
932 cm⁻¹
(b)
307 cm⁻¹
(c)
302 cm⁻¹
(d)
303 cm⁻¹
(e)
Ni doped Clusters (S1)
300 cm⁻¹
(f)
Ni doped Clusters (S1)
298 cm⁻¹
Intensity (arb. units)
Wavenumber (cm⁻¹)

FIG. 49

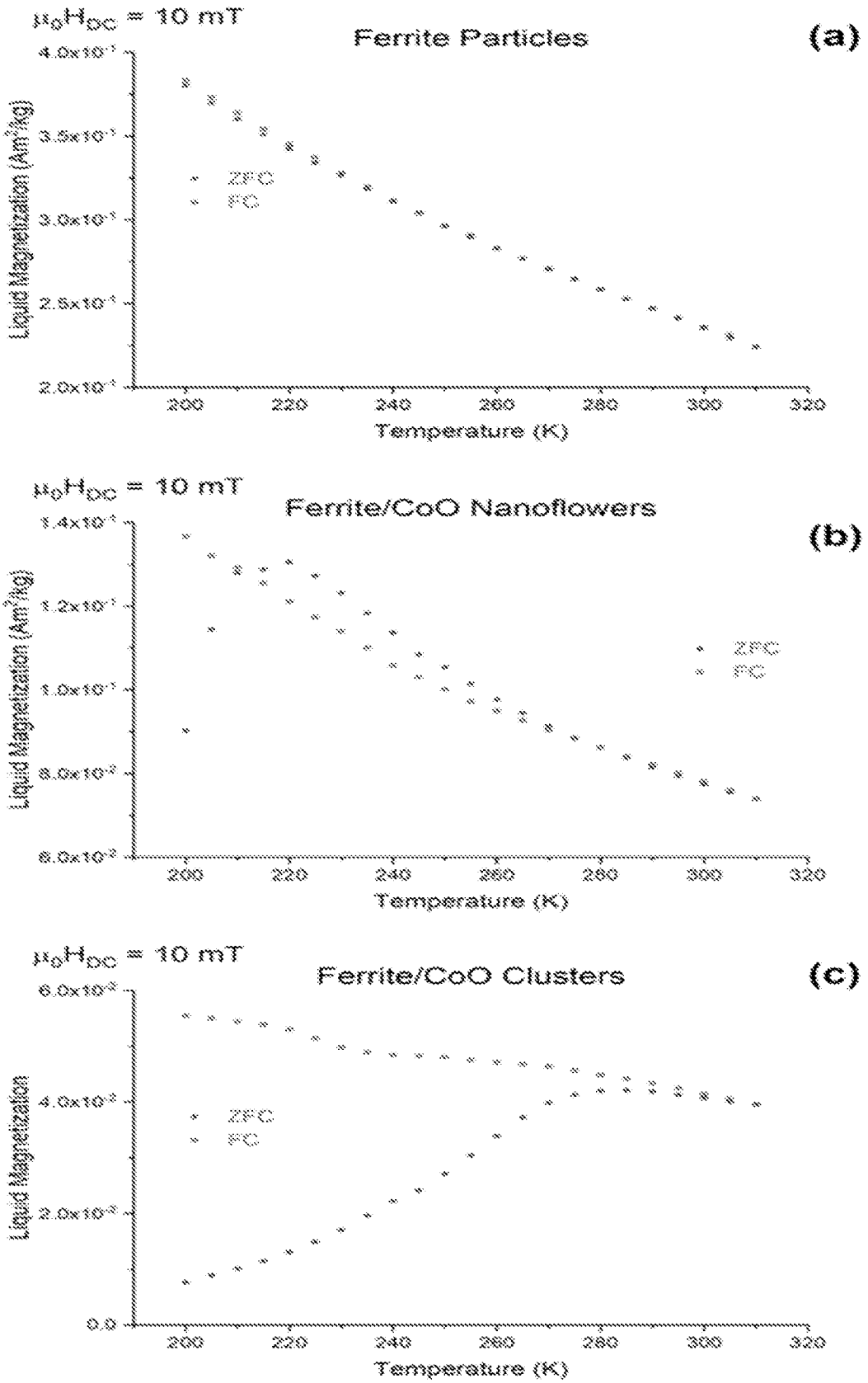
μ0HDC = 10 mT
Ferrite Particles
(a)
Liquid Magnetization (Am²/kg)
4.0x10⁻¹
3.5x10⁻¹
3.0x10⁻¹
2.5x10⁻¹
2.0x10⁻¹
ZFC
FC
200
220
240
260
280
300
320
Temperature (K)
μ0HDC = 10 mT
Ferrite/CoO Nanoflowers
(b)
Liquid Magnetization (Am²/kg)
1.4x10⁻¹
1.2x10⁻¹
1.0x10⁻¹
8.0x10⁻²
6.0x10⁻²
ZFC
FC
200
220
240
260
280
300
320
Temperature (K)
μ0HDC = 10 mT
Ferrite/CoO Clusters
(c)
Liquid Magnetization
6.0x10⁻²
4.0x10⁻²
2.0x10⁻²
0.0
ZFC
FC
200
220
240
260
280
300
320
Temperature (K)

FIG. 50

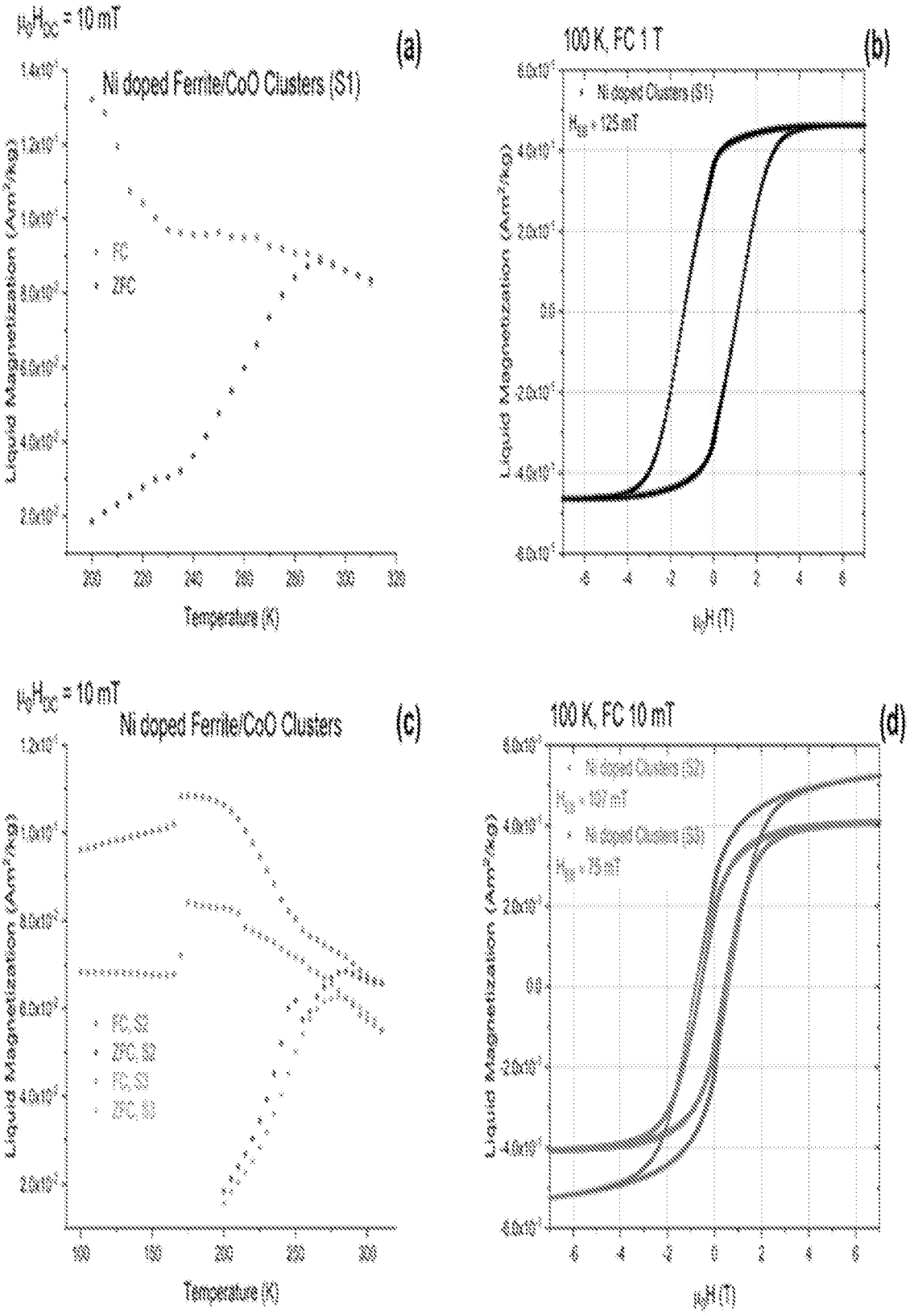
μ0H = 10 mT
(a)
Ni doped Ferrite/CoO Clusters (S1)
FC
ZFC
Liquid Magnetization (Am²/Kg)
Temperature (K)
100 K, FC 1 T
(b)
Ni doped Clusters (S1)
μ0H (T)
μ0H = 10 mT
Ni doped Ferrite/CoO Clusters
(c)
FC, S2
ZFC, S2
FC, S3
ZFC, S3
100 K, FC 10 mT
(d)
Ni doped Clusters (S2)
Ni doped Clusters (S3)

FIG. 51

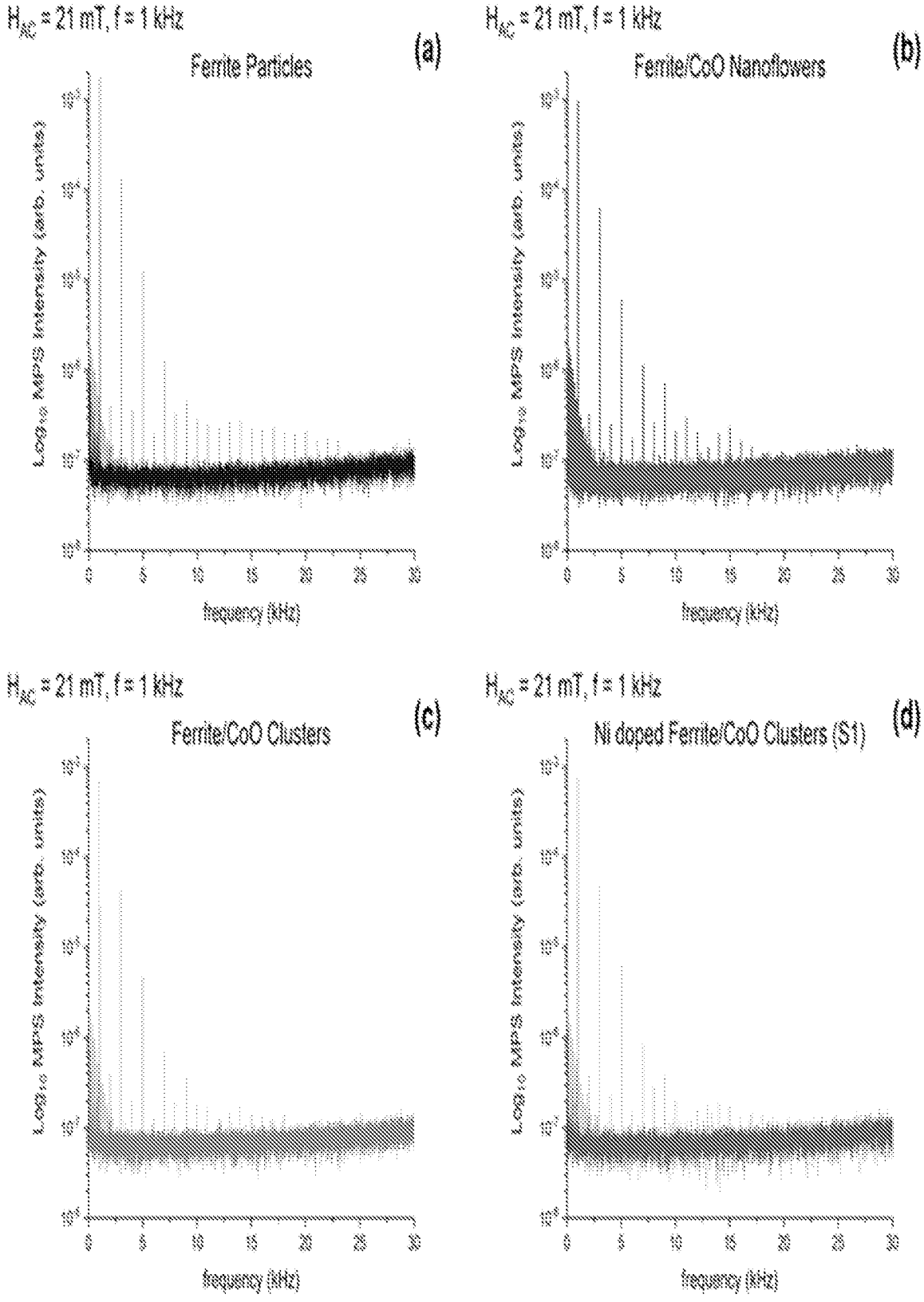
H_{AC} = 21 mT, f = 1 kHz
(a)
Ferrite Particles
Log_{10} MPS Intensity (arb. units)
Frequency (kHz)
H_{AC} = 21 mT, f = 1 kHz
(b)
Ferrite/CoO Nanoflowers
Log_{10} MPS Intensity (arb. units)
Frequency (kHz)
H_{AC} = 21 mT, f = 1 kHz
(c)
Ferrite/CoO Clusters
Log_{10} MPS Intensity (arb. units)
Frequency (kHz)
H_{AC} = 21 mT, f = 1 kHz
(d)
Ni doped Ferrite/CoO Clusters (S1)
Log_{10} MPS Intensity (arb. units)
Frequency (kHz)

FIG. 52

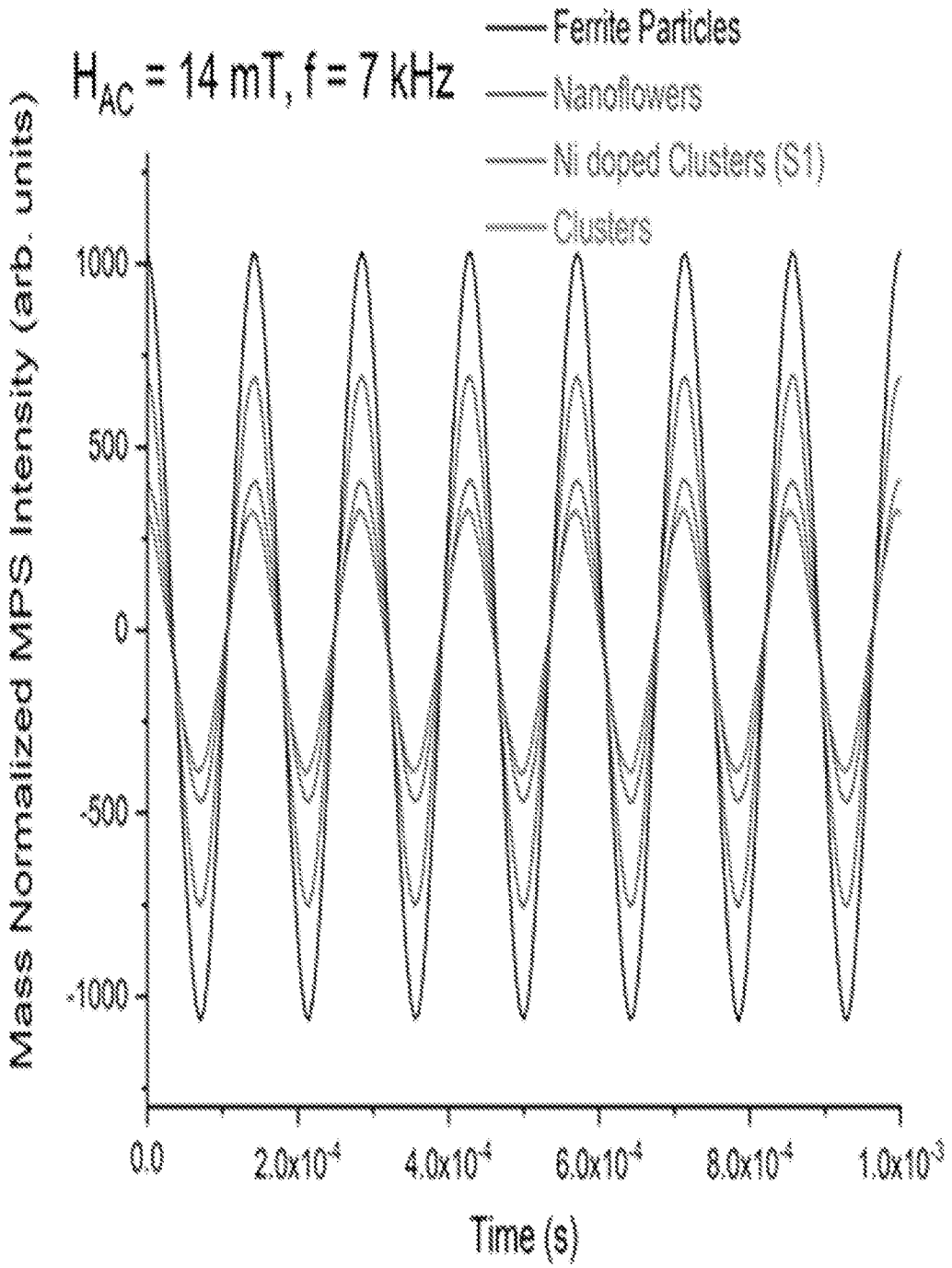
H_{AC} = 14 mT, f = 7 kHz
Ferrite Particles
Nanoflowers
Ni doped Clusters (S1)
Clusters
Mass Normalized MPS Intensity (arb. units)
1000
500
0
-500
-1000
0.0
2.0x10⁻⁴
4.0x10⁻⁴
6.0x10⁻⁴
8.0x10⁻⁴
1.0x10⁻³
Time (s)

FIG. 53

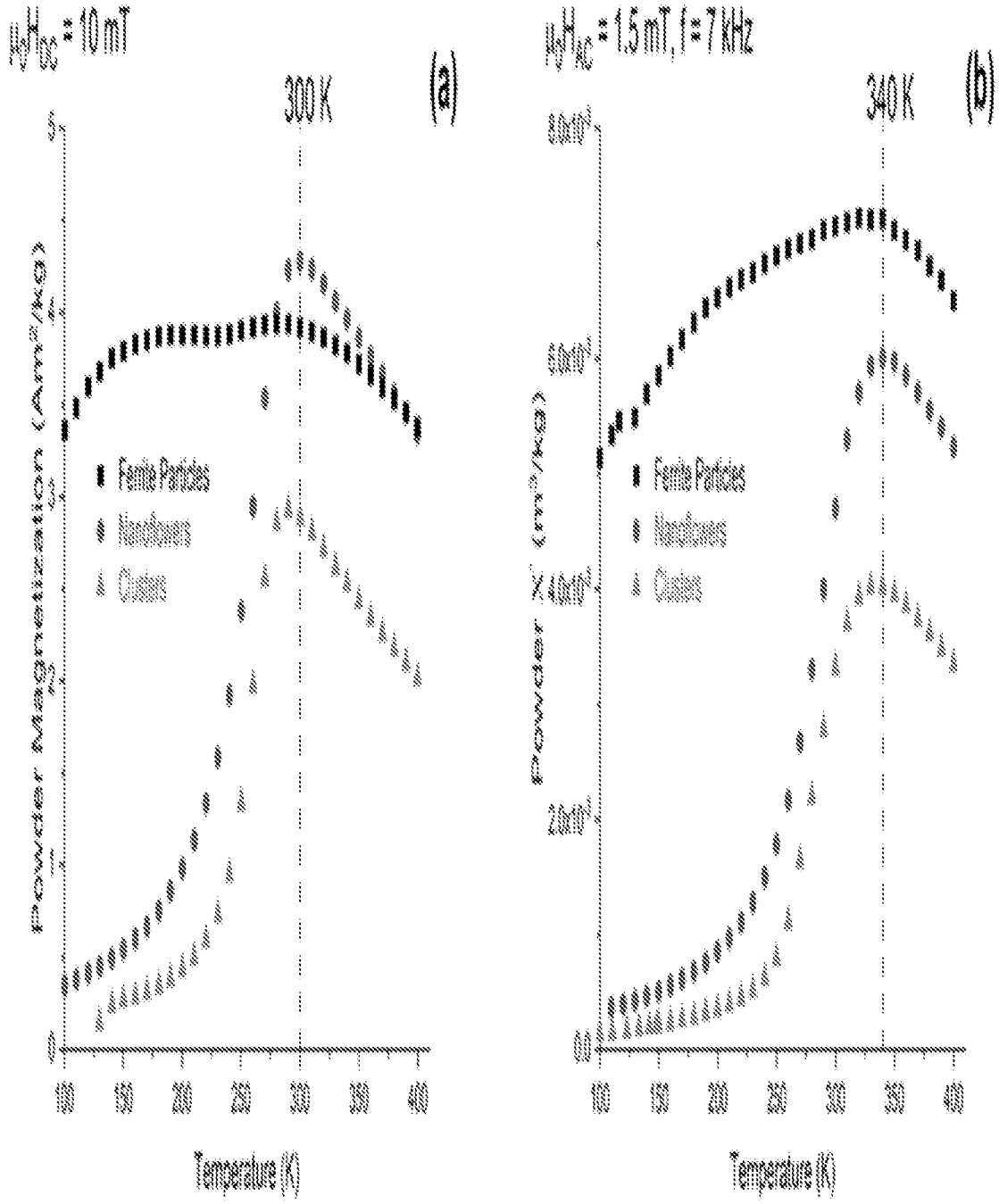
μ0Hac = 10 mT
300 K
(a)
Ferrite Particles
Nanocubes
Cubes
Temperature (K)
μ0Hac = 1.5 mT, f = 7 kHz
340 K
(b)
Ferrite Particles
Nanocubes
Cubes
Temperature (K)

FIG. 54

INTERNATIONAL SEARCH REPORT

International application No
PCT/US2022/043892

A. CLASSIFICATION OF SUBJECT MATTER
INV. G01K1/02 G01K7/36
ADD.

According to International Patent Classification (IPC) or to both national classification and IPC

B. FIELDS SEARCHED

Minimum documentation searched (classification system followed by classification symbols)
G01K

Documentation searched other than minimum documentation to the extent that such documents are included in the fields searched

Electronic data base consulted during the international search (name of data base and, where practicable, search terms used)
EPO-Internal, WPI Data

C. DOCUMENTS CONSIDERED TO BE RELEVANT

Category*	Citation of document, with indication, where appropriate, of the relevant passages	Relevant to claim No.
X	US 4 596 150 A (KUHR GEORGE A [US]) 24 June 1986 (1986-06-24)	1-3,6-9, 15-17, 19,20
Y	column 3, line 16 - column 5, line 44; figures 1-2	1-20
Y	US 9 719 863 B1 (CHANG CHIA-MING [US] ET AL) 1 August 2017 (2017-08-01) column 4, line 15 - column 15, line 11; figures 1-7	1-20

-/--

[x] Further documents are listed in the continuation of Box C.

[x] See patent family annex.

* Special categories of cited documents :

"A" document defining the general state of the art which is not considered to be of particular relevance

"E" earlier application or patent but published on or after the international filing date

"L" document which may throw doubts on priority claim(s) or which is cited to establish the publication date of another citation or other special reason (as specified)

"O" document referring to an oral disclosure, use, exhibition or other means

"P" document published prior to the international filing date but later than the priority date claimed

"T" later document published after the international filing date or priority date and not in conflict with the application but cited to understand the principle or theory underlying the invention

"X" document of particular relevance;; the claimed invention cannot be considered novel or cannot be considered to involve an inventive step when the document is taken alone

"Y" document of particular relevance;; the claimed invention cannot be considered to involve an inventive step when the document is combined with one or more other such documents, such combination being obvious to a person skilled in the art

"&" document member of the same patent family

Date of the actual completion of the international search	Date of mailing of the international search report
13 January 2023	23/01/2023

Name and mailing address of the ISA/	Authorized officer
European Patent Office, P.B. 5818 Patentlaan 2 NL - 2280 HV Rijswijk Tel. (+31-70) 340-2040, Fax: (+31-70) 340-3016	Rosello Garcia, M

1

Form PCT/ISA/210 (second sheet) (April 2005)

INTERNATIONAL SEARCH REPORT

International application No
PCT/US2022/043892

C(Continuation). DOCUMENTS CONSIDERED TO BE RELEVANT

Category*	Citation of document, with indication, where appropriate, of the relevant passages	Relevant to claim No.
T	RUS ERIC D. ET AL: "Magnetic Characterization of Electrodeposited Pt 1-x Ni x Alloy Films: Influence of Deposition Potential and the Presence of Boric Acid", JOURNAL OF THE ELECTROCHEMICAL SOCIETY, vol. 169, no. 9, 21 September 2022 (2022-09-21), page 092518, XP093012748, ISSN: 0013-4651, DOI: 10.1149/1945-7111/ac8ad1 Retrieved from the Internet: URL:https://iopscience.iop.org/article/10.1149/1945-7111/ac8ad1/pdf> [retrieved on 2023-01-11] the whole document -----	1-20
T	ABEL FRANK M ET AL: "Thermosensitivity Through Exchange Coupling in Ferrimagnetic/Antiferromagnetic Nanocrystalline Composites for Spatially Resolved Thermometry (Abstract: A54.00008)", APS MARCH MEETING 2022, VOLUME 67, NUMBER 3; MARCH 14-18, 2022; CHICAGO (USA), vol. 67, 14 March 2022 (2022-03-14), pages 1-1, XP093012924, Hauppauge, NY 11788 (USA) Retrieved from the Internet: URL:https://meetings.aps.org/Meeting/MAR22/Session/A54.8> [retrieved on 2023-01-11] the whole document -----	1-20

1

INTERNATIONAL SEARCH REPORT

Information on patent family members

International application No
PCT/US2022/043892

Patent document cited in search report	Publication date	Patent family member(s)	Publication date
US 4596150 A	24-06-1986	CA 1239991 A	02-08-1988
		EP 0195434 A2	24-09-1986
		JP H0658345 B2	03-08-1994
		JP S61258161 A	15-11-1986
		US 4596150 A	24-06-1986
US 9719863 B1	01-08-2017	NONE	